ADVANCED MATERIALS
www.advmat.de

# Efficient and Stable Perovskite Solar Cells by Tailoring of Interfaces

*Jianxing Xia, Muhammad Sohail,* and Mohammad Khaja Nazeeruddin**

**The interface tailoring is crucial for the efficiency and stability of Perovskite Solar Cells (PSCs). The reported interface engineering primarily focuses on the energy level turning and trap state passivation to improve the photovoltaic performance of PSCs. In this review, molecule modifications are classified according to the basics of electron transfer mechanisms for the interface tailoring of materials. An in-depth analysis of energy level modification and trap passivation, as well as the universal Density Functional Theory (DFT) method employed in interface tailoring. In addition, strategies to address environmental protection and large-scale mini-modules fabrication by interface engineering are also discussed. This review can guide the researchers in understanding interface engineering to design interface materials for efficient, stable, and eco-friendly PSCs.**

## 1. Introduction

Halide perovskite materials have attracted vast interest in recent years due to their excellent optical and electronic properties, such as the long charge carrier's diffusion lengths and lifetimes, as well as the intense absorption in the visible regions.[1,2] The power conversion efficiencies (PCEs) of perovskite solar cells (PSCs) have achieved above 25%[3] and have become the most potential candidates for next-generation solar cells since the first reported in 2009.[4]

Despite the remarkable achievements of PSCs, their progress is still hindered by the inevitable under-coordinated surface ionic defects or film defects within the metal oxide electrode, electron transport layers (ETLs), hole transportation layers (HTLs), perovskite functional layer and its relevant interfaces, crucially governing the efficiency, stability, and hysteresis of PSCs.[5,6] For the metal oxide ETLs, HTLs, and perovskite, it has been found that the ion vacancies are easily formed at surfaces[7,8] and accumulate the defects at the contact interfaces of electrode/ETLs, ETLs/perovskite, perovskite/HTLs and HTLs/electrode after the PSCs fabrication. These interface defects introduce trap states inside the bandgap of materials, which trap the free carriers, increase the interfacial non-radiative processes, and convert the excited state energy to thermal energy, significantly against the device's performance.[9] Secondly, except the materials itself induced the energy level mismatching after the fermi level equilibrium, the defect also influences the interfacial energy level matching due to the unbalanced surface charge induced electron transfer, which resulted from the interfacial build-in filed ($E_{bi}$) and the interfacial barriers.[10] In addition, some instability issues are caused by these defects, as it provides channels of ions migration under the thermal and light socking conditions, which act as the random dopant, changing the quasi-fermi level splitting of the interface, agonizing the performance of PSCs during aging.[11,12] The degradation of perovskite grains was initialized at the defective surface, while some crystals with low defects will collapse slower;[13] the charge accumulation usually localizes at the defects, which hinders the electric field distribution within devices, presumably resulting in intrinsic degradation of performance and influence the hysteresis of PSCs.[14–16] When the devices are scaled-up as modules, these interfacial defects-induced problems will be amplified, limiting the commercialization of PSCs. Furthermore, the degradation of perovskite material will also generate environmental issues due to the leakage of lead from PSCs.[17] To solve these obstacles, current works majorly focused on interface engineering to effectually reduce the trap states, reduce the interfacial charge accumulation, inhibit ionic migrations, and improve the hydrophobicity of PSCs. Additionally, interfacial energy level engineering also has been attempted to improve the performance and stability of PSCs. The strategies have got great success in reducing the non-radiative recombination, improving

J. Xia, M. K. Nazeeruddin
Institute of Chemical Sciences and Engineering
École Polytechnique Federale de Lausanne (EPFL)
CH-1015, Lausanne Switzerland
E-mail: MdKhaja.Nazeeruddin@epfl.ch
M. Sohail
Department of Chemistry
Texas A&M University at Qatar
Education City, P.O. Box 23874, Doha Qatar
E-mail: muhammad.sohail@qatar.tamu.edu
M. K. Nazeeruddin
Department of Materials Science and Engineering
City University of Hong Kong
Kowloon, Hong Kong 999077, China
M. K. Nazeeruddin
Center of Excellence for Advanced Materials Research (CEAMR)
King Abdulaziz University
P.O. Box 80203, Jeddah 21589, Saudi Arabia

The ORCID identification number(s) for the author(s) of this article can be found under https://doi.org/10.1002/adma.202211324



**DOI: 10.1002/adma.202211324**

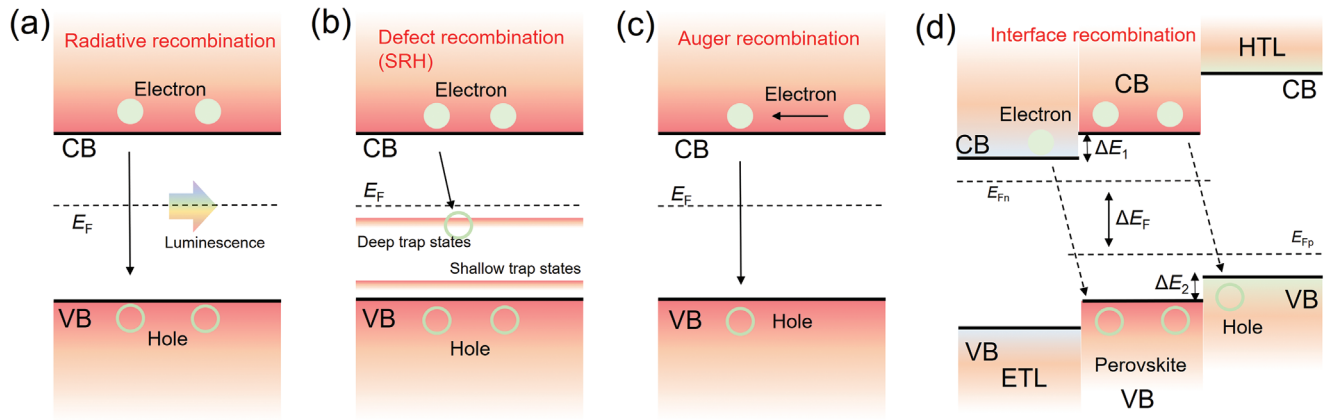


**Figure 1.** The various type of recombination processes of carriers within solar cells. a) The radiative recombination process; b) the defect recombination (SRH) process; c) the auger recombination process; d) the interface recombination process.

efficiency and stability, large area fabrication of PSCs, and environmental conservation, which facilitated the commercialization of PSCs.

In this review, the recent progress for various interface modifications of PSCs has been summarized. Especially, we discussed the internal mechanism for trap state generation, surface energy level, build-in field, and work function controlling, as well as provided the universal guidelines and research methods for interface trap states and energy level amelioration. This review outlook and insights on the research trends concerning promising strategies for interface modification to improve the efficiency and stability of PSCs, importantly, guide the interface materials design for trap states passivation and matched energy level. Additionally, the application of interface engineering for environmental protection and large-scale module fabrication is summarised.

## 2. Theory for the Interface Recombination Loss

After the photo-excitation, the radiative and non-radiative recombination's dominate the carrier recombination within solar cells.[18] The radiative recombination stems from the direct hole-electron recombination from the valance band (VB) and conduction band (CB) without the electron relaxation process (**Figure 1**a); it exists in the defect-free direct band gap semiconductor and without compromising the solar cell performance. In contrast, the auger recombination (non-radiative recombination) consists of the indirect band gap materials and is negligible within the hybrid halide perovskite (Figure 1c). The Shockley-Read-Hall (SRH) and interface recombination's dominate the non-radiative combination process of PSCs. The SRH recombination major comes from the un-coordinated ionic defects of perovskite-induced deep-level trap states, which trap the free-carrier at the gap states.[7,10,11] However, the shallow trap states faintly influence the non-radiative recombination as the states are near to the VB and CB, which could easily lead to de-trapped excited charge carriers under the increased thermal energy and reduce the non-radiative recombination (Figure 1b). When the hole transportation layers (HTLs) or electron transportation layers (ETLs) come into contact with perovskite film, the carrier would be collection by the ETL and HTL via the interface build-in field ($E_{bi}$) (Figure 1d). However, the position of band offset of ETL and perovskite ($\Delta E_1$), HTL, and perovskite ($\Delta E_2$) is vital for the non-radiative recombination at interfaces. The lower $\Delta E_1$ and $\Delta E_2$ will avoid electron or hole recombination, while the higher values result from more severe interface non-radiative recombination. Usually, the band offset between perovskite and the charge transportation layers lower than 0.2 eV is better for charge transportation and to restrain the interface recombination.[19] Another aspect is if the CB and VB of ETL and HTL are out of the CB and VB of perovskite, the interfacial non-radiative recombination will be effectively inhibited; however, the layers should be very thin, which allows the carrier tunneling.[20] Finally, both defect and interface non-radiative recombination will reduce the photovoltaic performance and result in open-circuit voltage ($V_{oc}$) loss of PSCs, as well as expressed by the formula:[21,22]

$$V_{oc} = V_{oc,rad} - \frac{K_B T}{e} ln\, EQE_{EL}^{-1} = V_{oc,rad} - V_{oc,\ non-rad} \quad (1)$$

Where the $V_{oc,rad}$ is the value of radiative recombination of devices, $V_{oc,non\text{-}rad}$ is the value of non-radiative recombination by the defects and interface factors, the $K_B$ is Boltzmann constant, T is temperature, e is the charge of an electron, and $EQE_{EL}$ is external quantum efficiency. For the interfaces, the $EQE_{EL}$ value is determined by the interface defects and the un-matched interface energy level induced non-radiative recombination. Thus, according to the equation, tailoring the interface defects and energy level could reduce the $V_{oc}$ loss of PSCs.

On the other hand, the interface carrier driving force is another factor that influences the interface non-radiative recombination and the EQE, which helps the trapped charges to escape from the trap defects and avoid the interface hole-electron pairs recombination via the potential difference. The carriers driving force originates from the heterojunction contact-induced interface $E_{bi}$ between perovskite and charge transportation layers (CTLs). The interfacial $E_{bi}$ depends on the electron and hole concentrations of semiconductors. Usually, the larger the Fermi level ($E_F$) difference between the contact semiconductors, the higher interface $E_{bi}$ obtained, resulting in higher $V_{oc}$ of PSCs. Generally,

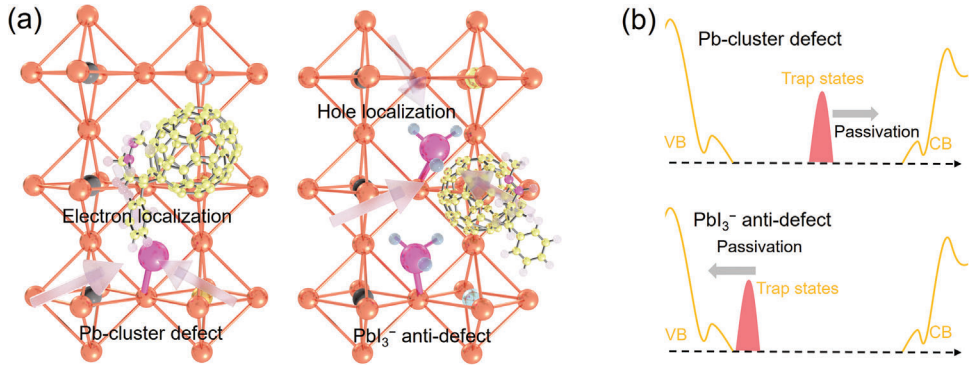


**Figure 2.** The passivation of perovskite defects. a) The typical Pb-cluster defects and the $PbI_3^-$ anti-defect, where the PCBM is signaled for the molecules induced passivation; b) the illustration of trap states shifting generated by Pb-cluster defects and the $PbI_3^-$ anti-defect within perovskite.

the relation between $V_{oc}$ and $E_F$ offset can be expressed by the equation:[18]

$$eV_{oc} = E_g - K_B T ln\left(\frac{n}{N_C}\right) - K_B T ln\left(\frac{p}{N_V}\right) = E_{Fn} - E_{Fp} \quad (2)$$

Where $E_g$ is the band gap of perovskite, the $K_B$ is Boltzmann constant, T is temperature, e is the charge of an electron, n is the electron concentration of ETL and $N_C$ is the corresponding electron density of states, p is the hole concentration of HTL and $N_v$ is the hole density of states, the $E_{Fn}$ is the quasi-fermi level of ETL, the $E_{Fp}$ is the quasi-fermi level of HTL. It indicates that the higher splitting of quasi-fermi levels between ETL and HTL will result in higher $V_{oc}$. In addition, the higher charge concentrations of ETL and HTL also benefit the $V_{oc}$. Thus, tailoring the interface $E_F$ is the basic method to further improve the $V_{oc}$ of PSCs.

## 3. Theory for the Interface Amelioration

### 3.1. Theory of Passivate Interface Defects

The defects of the perovskite surface are generated during the device fabrication, which depends on the nature of solution processing and the rapid crystal growth of perovskite thin films at a lower temperature.[11] It is reported that the major intrinsic point defects in the $MAPbI_3$ crystal are three types of vacancies ($V_{MA}^-$, $V_{Pb}^-$, $V_I^+$) and three types of interstitials ($MA_i$, $Pb_i$, $I_i$).[23,11] These interstitials and vacancies defects always form deep-level states within the band gap of perovskite, leading to non-radiative recombination losses at the bulk of the perovskite interface. The Density Functional Theory (DFT) finds that the positive iodide vacancies ($V_I^+$) and $MA^+$ vacancies ($V_{MA}^-$) are the dominant defect species within typical $MAPbI_3$ perovskites due to the much lower formation energy than the $Pb^{2+}$ vacancies.[7] The typical defects of Pb-cluster always from the ($V_I^+$) or the interstitial $Pb^{2+}$ atoms; however, the electron-rich $PbI_3^-$ anti-defect major from the interstitial $I^-$ atoms or the ($V_{MA}^-$), which are abundant within the grain boundary and the surface of perovskite film (**Figure 2**a).[7] The trap states of the typical Pb-cluster defect and the $PbI_3^-$ anti-defect have been widely studied by the orbital distribution and partial density of states (PDOS) of DFT.[24] The results find that the Pb-cluster defects give rise to the localization of the lowest unoccupied conduction band states on the perovskite surface, inverse the charge localization of $PbI_3^-$ anti-defect dominating in the highest occupied valence band states due to both non-equilibrium surface defects charge. If the anti-charge of ions is employed on the defect surface, the localization of surface orbitals will reduce or eliminate by the balanced surface charge. The PDOS analysis finds that the CB and VB of the defect-free perovskite crystal contributed by the orbitals of $I_{5p}$ and $Pb_{6p}$; however, the $MA^+$ cation will not contribute to the important states of perovskite.[25,26] When the Pb-cluster was introduced on the perovskite surface, there were new gap states within the middle of the band gap of perovskite, which serve as deep traps due to the states being occupied by an excess electron. For the $PbI_3^-$ anti-defect, the trap states close to the perovskite VB, which may be due to the accumulation of holes at the perovskite surface via the un-balanced charge.[10,24] As shown in Figure 2b, when the ions with the anti-charge to the defects, the trap states move to the CB or the VB of perovskite (the Pb-cluster defect moves to the CB, but the $PbI_3^-$ anti-defect moves to the VB side). The change of the surface charge localization is the key factor that reverses the deep trap states to the shallower ones or reduces the trap states completely.[10] To passivate the corresponding trap states, the ionic-type compounds are useful for these obstacles.[25] Furthermore, the transfer of surface charges by graphene derivative,[27] molecule donor or acceptor,[28] atomic coordination chemistry [29] is another way to passivate the trap states. In principle, the Pb-cluster defect will be passivated by some substance which will deplete the surface of extra electrons; however, the $PbI_3^-$ anti-defect passivation needs electron acceptors from the contact substance. To passivate both of these trap states, there needs both turn the surface electron concentration together. The basic passivation mechanism will help to screen the passivation substances for perovskite film in future studies.

### 3.2. Theory of Tailoring Interface Energy Level Alinement

The band alignment between the interfaces of semiconductors is of particular interest for PSCs, which determine the carrier collection efficiency. The band alignment influences the interface Schottky barrier and the interface $E_{bi}$ after the contact of the semiconductor with the balanced $E_F$. To tailor the interfacial band alignment, the work function ($W_F$) of the semiconductor was usually changed by the surface modification via

ionic compound,[13] quantum dot,[30] derivatives of graphene,[27] organic acceptor/donor,[28,31] and self-assembling monolayer.[32] The $W_F$ of a uniform semiconductor is defined as the minimum energy required to remove an electron from the $E_F$ of the conductor to just outside the surface having a local vacuum level ($E_{vac}$) by $W_F = E_{vac} - E_F$. The higher electron concentration indicates a higher $E_F$ and a lower $W_F$. Thus, tuning the electron concentration of a semiconductor surface is the key path to tailoring the interface energy level. The free electron concentrations are defined as:[33]

$$n = \int_{CB}^{\infty} D(E)\, F(E)\, dE \tag{3}$$

$$F(E) = 1/\left(e^{(E-E_F/KT)} + 1\right) \tag{4}$$

Where D(E) is an electron density of states (DOS), and F(E) is the Fermi-Dirac distribution function. Thus the change of electron concentrations of semiconductors is extremely related to the $E_F$ and DOS, as well as makes a change in work function. The DOS can be obtained by the DFT calculation. Commonly, for the perovskite film, the electron concentration can be tuned by the different ratio of $PbI_2$/MAI or FAI, which the $PbI_2$ rich perovskite surface with high electron concentration trends to become n-type, but the MAI or FAI dominated perovskite surface with the low electron concentration resulted in p-type.[34] Modulating the components ratio of the perovskite will tune the interface contact of ETL/perovskite and perovskite/HTL. The charge transfer by surface modification is another way to change the surface electron concentrations. The donor of an electron to the semiconductor surface will increase the $E_F$ and reduce the corresponding surface $W_F$. Inversely, the electron transfer to other substances will reduce the $E_F$, resulting in more p-type of the semiconductor surface. The surface systems consist of the semiconductor (S) and interacted molecules (M). In this scenario, all the semiconductors are defined as having the same electron affinity ($EA_S$) and ionization energy (IPs), and the molecules are defined as $EA_M$ and $IP_M$ for the electron affinity and ionization energy. As shown in **Figure 3**a, the pairs of semiconductor and surface molecules can be found either in a neutral or ionized microstate according to the local equilibrium of the reaction $S + M \leftrightarrows S^+ + M^-$ (p-doping) or $S + M \leftrightarrows S^- + M^+$ (n-doping). The energy difference between these two microstates would be $\Delta E = -\Delta E_{off} + V_C + \Delta V_E$, where $\Delta E_{off} = EA_M - IP_S$ or $\Delta E_{off} = |EA_S - EA_M|$is the semiconductor-molecule specific orbital energy difference, and $V_C = -e^2/4\pi\epsilon\epsilon_0 r$ is the electrostatic interaction energy between within the semiconductor-molecule system, r is the distance between the semiconductor-molecules system, $\epsilon$ is electric constant, $\epsilon_0$ is relative material permittivity, and e is the elementary charge. $\Delta V_E$ is the electrostatic environmental potential for the complicated surface modification system. An environmental charge would influence the electrostatic potential, as the molecules and semiconductor units are not single. The environmental electrostatic potential ($\Delta V_E$) can be expressed by:[35]

$$\Delta V_E = \frac{-e^2}{4\pi\varepsilon\varepsilon_0 r}\left[\sum_{\alpha}(r_\alpha - r_S)^{-1} - (r_\alpha - r_M)^{-1}\sum_{\beta}(r_\beta - r_S)^{-1} - (r_\beta - r_M)^{-1}\right] \tag{5}$$

Where the $\alpha$ and $\beta$ are the positive and negative charges in the environment, $r_\alpha$, $r_\beta$, $r_S$, $r_M$ are the positions of positive and negative charges in the environment, and the positions of the semiconductor units and surface molecule, respectively. As the energy difference of the semiconductor-molecules system, the electron or the hole will be hopping between the two sites, and the hopping rate of an electron or hole from site $i$ to $j$, $W_{ij}$ is described by the Miller-Abraham (MA) equation:[36]

$$W_{ij} = \nu_0\, e^{(-2r_{ij}/b)} e^{\left[-\frac{|E_j - E_i| + (E_j - E_i)}{k_B T}\right]} \tag{6}$$

Where $E_j$ and $E_i$ are energies of the final and initial state, $\nu_0$ is the attempt-to-escape frequency, $b$ is the localization radius of a charge carrier, $k_B$ is Boltzmann constant, T is the temperature. Thus, a change in the energy levels and the potential difference between semiconductor and modification molecules will change the surface electron or hole hoping, resulting in different surface electron and hole concentrations of the semiconductor. For the interface engineering of PSCs, when the $E_F$ equilibrium after the contact between perovskite and CTLs, the interface contact energy level will be changed. Recently, as shown in Figure 3b, Chen et al.,[36] and Tu et al.,[37] employed the surface molecule-semiconductor charge transfer turned the interface energy level between perovskite/CTLs and results in surface p or n-doping of semiconductor, which turned the interfacial energy levels and improved the efficiency of PSCs.

The presence of the well-ordered ionic charge layers and the surface anchoring monolayers (SAMs) of the semiconductor interfaces usually form specific dipole moments, as shown in Figure 3c,d, which transfer the surface electron and change the surface $W_F$, finally promote the charge carrier dynamics within the semiconductor devices.[38,39] The surface dipole by the ionic compounds and surface anchoring monolayer will provide a surface electric field; however, the orientation of these molecules and the antiphase dipole is vital for total dipole and the $W_F$ changes. The total surface dipole moment primarily comprises two portions after the molecule is deposited on the semiconductor surface. The first part depends on the effectiveness of the dipole moment supplied by the molecule itself, and the second dipole moment is provided by the interaction between surface atoms and molecule (S-M). The surface potential change caused by the external dipole-induced surface electric fields across the basal plane according to classical electrostatics and the alteration of the $W_F$ can be expressed by:[40,41]

$$\Delta\varphi = -N\left[\frac{\mu_{\perp,M}}{\epsilon_0\kappa_M} + \frac{\mu_{s-M}}{\epsilon_0\kappa_{s-M}}\right] \tag{7}$$

where the $\mu_{\perp,M}$ is the dipole moment perpendicular to the perovskite surface, $\mu_{s-M}$ represents the dipole moment caused by the surface atomic interactions, N is the grafting density, and k and $\epsilon_0$ are the dielectric constants and the permittivity of free space, respectively. The $\mu_{s-M}$ can be estimated by the length of the bond which anchors to the atoms of the semiconductor ( $\mu_{s-M} = qL$, where the q is the charge, and L is the bond length).[11] Therefore, the $\Delta\varphi$ is dependent on the surface atomic interactions ($\mu_{s-M}$) and the magnitude and direction of the molecular dipole moment toward the perovskite surface ($\mu_{\perp,M}$).

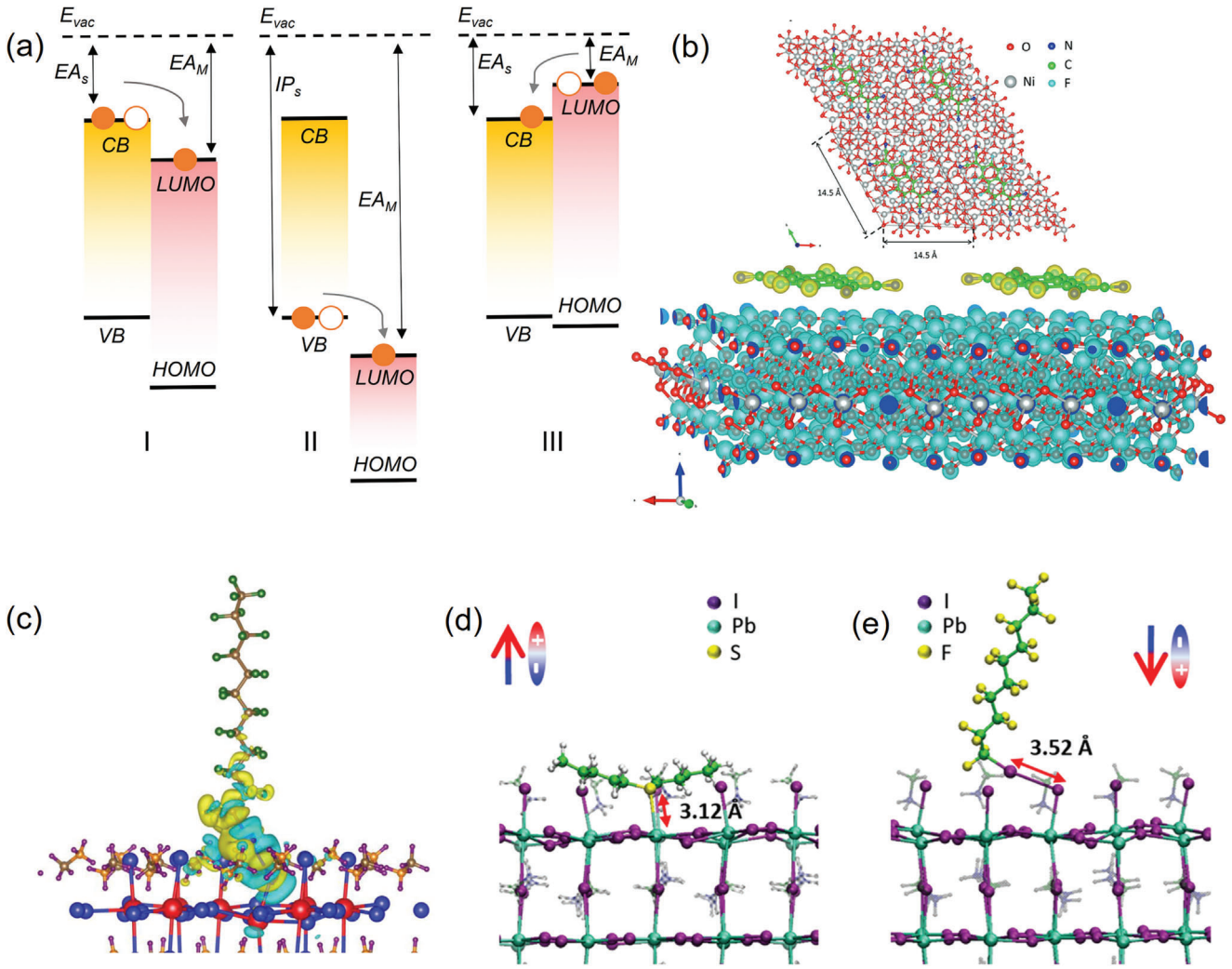


**Figure 3.** Theory of tailoring interface energy level alinement. a) The electronic transfer mechanism by the donor or acceptor contact with the semiconductor; b) the acceptor F6-TCNNQ adsorption on the NiO surface; Reproduced with permission.[36] Copyright 2018, Wiley-VCH; c) the I-$PFC_{12}$ SAM adsorption on perovskite surface and form a surface dipole, as well as the charge density difference; Reproduced with permission.[39] Copyright 2020, American Chemical Society; d) the amyl sulfide SAM adsorption perovskite surface, lay on orientation;[38] e) the perfluorodecyl iodide adsorption perovskite surface, vertical orientation. Reproduced with permission.[38] Copyright 2021, The Royal Society of Chemistry.

The principle of the complex dipole calculation, which combines DFT, would be better and more useful for the further interface modification of dipole and molecule design.

### 3.3. DFT Methods for the Interface Engineering

The DFT is vital for the interface engineering of PSCs, which combines the experimental results conducted with the insights mechanism of interface tailoring and guides the interface material design or the trend of interface modification. It can effectively and accurately study the electronic structure, defects, bonding, surface physical and chemical adsorption of the solid and its clean surface. It meets the requirements of the study on the difference between periodic surface and interface binding energies, bonding types, surface electron transfer, orbitals, trap passivation, and the ionic migration barriers, which has become an important theoretical simulation tool for the interface engineering of PSCs.[42,43] It is feasible to employ DFT to provide a theoretical basis for designing interface-modified materials. Gaussian,[44] CASTEP,[45] VASP,[46] Quantum ESPRESSO[47] and CP2K[48] are the widely used package software for the PSCs. Especially the Gaussian is merely suitable for molecule calculation, and others are suitable for the periodic structure.

#### *3.3.1. Adsorption Model and Binding Energy*

Interface engineering usually employs small organic molecules, polymers, ionic liquids, organic-inorganic salt, and carbon-based materials. The interface interactions are always experimental and measured by the XPS and FITR; however, the special model and the interfacial configuration are challenging to construct, especially the multi-interaction sites at the semiconductor surface

within PSCs. The specific orientation of the interfacial materials is vital for the interface energy level, as the different potential distribution of molecules. The reducible molecules interface materials usually directly adsorption on the clean and stable surface of the semiconductor interface, such as small molecules and ionic liquid [25,49] While the crystal-based interface materials could form a heterojunction with the absorption interface after matching a lattice.[50] More precisely, the interaction could be calculated by the multiple molecular absorptions within the molecular dynamics (MD) as the intermolecular interactions that cannot be ignored, such as the Van der Waals, bonding, and the potential. The calculation of binding energy ($\Delta E_B$) by an absorption model is usually defined as: $\Delta E_B = (E_A - E_0 - nE_m)/n$, where the energy of $E_A$ is the total energy of the optimized semiconductor surface adsorbed with the interface materials, the $E_0$ is the total energy of the optimized semiconductor surface, and the $E_m$ is the energy of optimized molecules, n is the number of the molecules.[51] Han et al. elucidated the binding energies of each Lewis base bonded to the perovskite crystal by using DFT. The binding energies were calculated to be −19.4, −31.5, and −34.5 kJ $mol^{-1}$ for ethylene carbonate, propylene carbonate, and poly(propylene carbonate), respectively.[52] Zhou et al. calculated the binding energy between the DTBTI and perovskite. The large value (−2.17 eV) for the DTBTI coordinated with Pb atoms, as the O, N, and S atoms in DTBTI are rich in electrons.[53] You et al. compared the binding energy of $COO^-$, $-OSO_3^-$, $CH_2OSO_3^-$ and $-NHSO_3^-$ groups adsorption on perovskite and the $TiO_2$, confirmed the preferential adsorption of a functional group of the biopolymer heparin sodium.[54] Yang et al. employed the MD to calculate the $SO_4^-$ adsorption on perovskite MAI terminal at 350 K for several picoseconds, suggesting a stronger interaction between surface Pb atoms of $MAPbI_3$ and $SO_4^-$ units to form PbSO4, which protected the perovskite crystal.[55]

### 3.3.2. Electron Localized Function

Excepting the binding energy of molecules adsorption on the semiconductor surface, elucidating the bond type at the interface is also necessary for interface modification. The electron localization function (ELF) clarified the distribution of electron localization at the interfaces, which may offer a visualized physical picture of the chemical bonds.[56,57] For closed-shell systems, the ELF is defined as:

$$ELF = 1/[\left(\frac{D_\sigma}{D_0}\right)^2 + 1] \quad (8)$$

The value of ELF highly depends on the electron localization and ranges from 0 to 1. The higher the ELF value, the more localization of the electrons. ELF = 1 corresponds to the electron totally localized (lone pairs), and ELF = 0.5 matches the probability of the electron-gas-like pair. Analysis of ELF can efficiently reveal the character of different chemical bonds. Gong et al. evaluated ELF of perovskite interacting with the $Ni^{2+}$ ions (**Figure 4**a). The insertion of $Ni^{2+}$ ions decreases the intensity of electron localization on $MA^+$ and $I^-$ regions, implying $Ni^{2+}$ shares electrons with surrounding ions and interacts with $MA^+$ cations with lone pair electrons and octahedral $[PbI_6]^{4-}$ as well. The electron from $MA^+$ components distributes around $Ni^{2+}$, which is strong evidence for electrons localized nearby the $Ni^{2+}$.[58] Our previous work also employed the ELF to elaborate further on the interaction between $Li^+$/organic cation and $O_2/H_2O$. When the oxygen and $H_2O$ interact with a phenylamine cation-based surface, the electrons prefer to localize between the H atom of phenylamine cation and O atoms, implying its weak interactions; however, there is delocalization of electrons density between Li ions and O atoms, inversely indicating stronger interactions.[26] Cao et al. also studied the ELF contour plots of graphene/$PbI_2$ and graphene/$CH_3NH_3I$ interfaces (Figure 4b). The ELF is 0.6 between C atoms of graphene and attains a maximum value of 0.86 near C atoms, indicating the strong covalent bonds within graphene. However, The ELF is lower than 0.1 in the middle of the graphene/$PbI_2$ and graphene/$CH_3NH_3I$ interface, which indicates that no electron is located in these regions and there is no existence of covalent bonds connecting the graphene layer and the perovskite slab.[59] Further study to employ ELF for the interface modification could compensate for the interaction analysis.

### 3.3.3. Charge Density Difference

The interface interactions, usually along with the electron transfer process, will alter the interface energy levels and play important roles in improving PSCs performance. Ultra-violet photoelectron spectroscopy (UPS) and the Kelvin probe force microscope (KPFM) are the standard measurements to realize the energy level shifting of materials after the interface modification. However, the specific charge transfer and the insight reason are blurry. Charge density difference is visualized for the electron redistribution at the atomic scale, which will help to analyze the reason for charge transfer, such as the different donor or acceptor properties of the materials and the interaction formed surface dipole. The charge density difference $\Delta\rho$ is defined as $\triangle\rho = \rho_A - \rho_0 - \rho_m$, where $\rho_A$, $\rho_0$, and $\rho_m$ denote the charge density of the optimized adsorbed slabs, the corresponding separated slab without the adsorbed molecules, and the molecules, respectively.[10,25] Ou et al. deposit the $MoO_3$ on the $MAPbI_3$ surface, and the UPS results find that the perovskite becomes more p-type of the surface after the $MoO_3$ contact. As exhibited in Figure 4d, the charge density difference finds that a strong electron accumulation appears around the Mo atoms, while the electron depletion around the I atoms of the $MAPbI_3$, indicating that $MAPbI_3$ transfers the electrons to $MoO_3$. Notably, a substantial electron accumulation is present around the O atoms of $MoO_3$ that form N–H...O hydrogen bonds.[60] Theoretically, the electron loss from perovskite is consistent with the p-doping of a surface from UPS. Similarly, Tu et al. also employed the charge density difference to probe the reason for TPPO-induced n-doping for the $SnO_2$. The results find that electron loss of $R_3P^+$-$O^-$ $\sigma$-bond will be received and spread to peripheral tin atoms other than the directly connected Sn atoms in the redistribution and result in the n-doping of surface $SnO_2$.[37] Wang et al. also employed it to explain the p-doping of the molecules. Furthermore, the amount of charge transfer also can be used to estimate the strength of the interface interaction.[61] Qiao et al. studied the charge density difference of different ions ($Pb^{2+}$, $In^{3+}$, $Sb^{3+}$) adsorbed on the $TiO_2$ (101) surface (Figure 4c). Where it can be seen that the charge

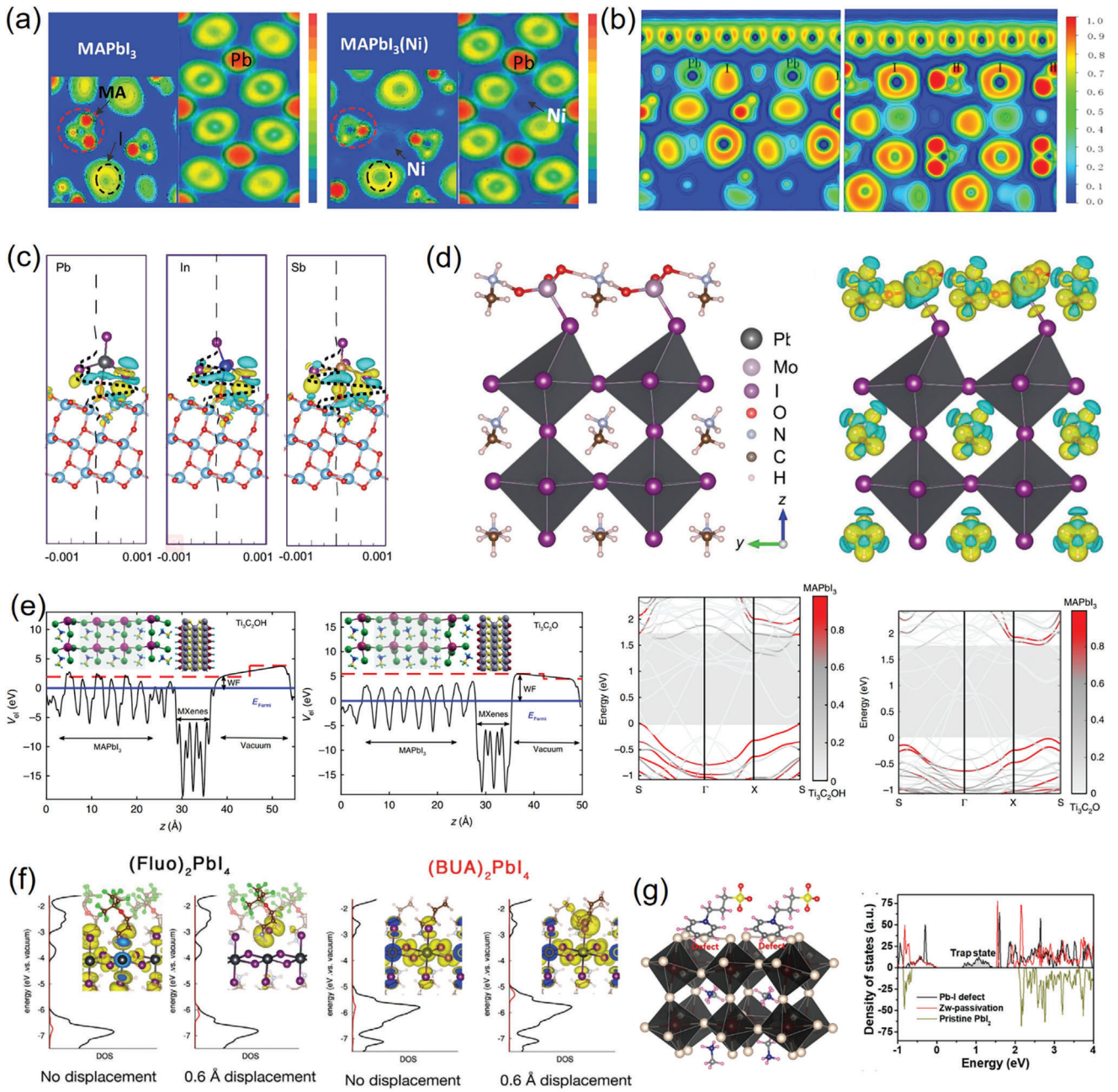


**Figure 4.** DFT methods for interfacial engineering. a) The ELF of $Ni^{2+}$ ions interacted with perovskite; Reproduced with permission.[58] Copyright 2018, Wiley-VCH; b) The ELF of graphene interacted with perovskite; Reproduced with permission.[59] Copyright 2018, American Chemical Society; c) the charge density of difference of $Pb^{2+}$, $In^{3+}$, and $Sb^{3+}$ interacted with $TiO_2$ (101) surface; Reproduced with permission.[62] Copyright 2018, Wiley-VCH; d) the structure and the charge density differences of $MoO_3$ interacted with perovskite; Reproduced with permission.[60] Copyright 2018, Wiley-VCH; e) the electrostatic potential averaged over planes perpendicular to the $MAPbI_3/Ti_3C_2(OH)_2$ and $MAPbI_3/Ti_3C_2O_2$ interface, as well as the band structures of the $MAPbI_3$/Mxene slabs for OH and O termination of the Mxene; Reproduced with permission.[63] Copyright 2019, Springer Nature; f) total DOS (black curve) and DOS (red line) of one iodine which has been pulled out by 0.6 Å (vide infra) with respect to the perovskite plane, the inset is the spatial localization of the valence band edge orbital; Reproduced with permission.[64] Copyright 2018, Wiley-VCH; g) the schematic model showing passivation of $Pb–I_3^-$ defects, and the DOS of a $Pb–I_3^-$ antisite defect, $Pb–I_3^-$ defect passivated with the zwitterion and pristine $PbI_2$. Reproduced with permission.[13] Copyright 2018, The Royal Society of Chemistry.

transferred across the interface between $Sb^{3+}$ based cluster and the $TiO_2$ (101) is higher than the $Pb^{2+}$ and $In^{3+}$-based cluster, which consistent the stronger interaction between the perovskite and the electron acceptors.[62]

#### 3.3.4. Band Structure and Orbitals

As discussed above, the interfacial materials interaction and the interaction induced charge transfer; however, the surface band structure and the orbitals, as well as the work function, will influence the shifting of the energy level at the hetero-junction interface. Agresti et al. employed the DFT to understand the origin of the perovskite $W_F$ change induced by the interaction with Mxene and compared the interface of perovskite/$Ti_3C_2T_x$ with OH and O termination, as shown in Figure 4e, the $MAPbI_3/Ti_3C_2(OH)_2$ interface induced an interface dipole. It led to the interfacial electron transfer, causing a reduction of the $W_F$ and affecting the band alignment of the system. However, the $MAPbI_3/Ti3C_2O_2$ interface results in higher $W_F$. In addition, the perovskite bandgap is barely affected by the interaction with MXene, remaining at 1.7 eV, during the shifting of the VBM and CBM when they contact Mxene with the OH or O termination. It indicates that the weak interfacial dipole will influence the energy level alignment.[63] Queloz et al. also employed the DFT studied the displacement of the 2D organic cations on the DOS orbitals distribution (Figure 4f). 0.6 Å displacement of both BUA and Fluo cation will up shifting the VBM and CBM of perovskite.[64,65] The DOS is also employed to realize trap passivation via interface engineering. Choi et al. employed the zwitterion at the interface of $SnO_2$/perovskite and calculated the DOS before and after the molecular interaction (Figure 4g). Finally, the trap states within the band gap of perovskite have been eliminated, attributing to Pb–N bond-induced charge balance.[13] Wang et al. calculated the DOS of perovskite interactions with or without the C=O group-based molecules. When the C=O groups modify the perovskite, a rather insignificant shift in the valence band maxima (VBM) and the conduction band minimum (CBM) takes place compared with that in the $FAPbI_3$ cells containing $FA^+$ vacancy. However, the C=O group will passivate the $I^-$ vacancy and Pb-cluster trap state well.[65] Specially employing the DFT and DOS calculation, we find that the different orientations of the molecules or ionic dipole will influence the shifting of trap states in our previous work. The forward orientation of the dipole toward the perovskite surface will convert the deep trap states (Pb-cluster) to shallower ones, while the reverse surface dipole will make the trap states deeper. The shallower trap states make the electron easier de-trap the excited charge carriers even with the extra thermal energy.[10]

## 4. Energy Level Tailoring and Passivation

### 4.1. ETL/Perovskite Interface

The electron transporting layers (ETLs) are crucial in PSCs, which transport electrons and block holes.[13,24] At present, the most commonly employed ETLs in n-i-p PSCs are the metal oxide $SnO_2$ and $TiO_2$; for the p-i-n structure, the popular ETLs are the PCBM and $C_{60}$. Although the high electron mobility of these materials effectively auxiliary light raw electronic-hole separation, The ETLs, and the relevant contact heterojunction interface also suffer from many disadvantages: 1) oxygen vacancy defects are inevitable within metal oxide ETLs during the preparation, damaging the interface contact of ETLs/perovskite heterojunction.[7,8] In addition, vacancy defects accumulate an unbalanced charge at the interface, resulting in the recombination of photo-generated carriers. 2) The photocatalytic activity of oxygen vacancies of metal oxides surface under ultraviolet light enhances, thus, accelerating the interface degradation of perovskite, which affects the intrinsic stability of the PSCs under working. 3) The accumulated charge changes the internal electric field balance of the interface, aggravates the hysteresis phenomenon, and degrades the intrinsic stability of the device.[24] Others, the interfacial energy level matching and the trap states of perovskite film at the contact interface are also vital for overall performance parameters within PSCs. Therefore, solving these obstacles of ETLs/perovskite interface is particularly important for the efficient, stable, and low hysteresis PSCs. The interface modification tailored the interface energy level, work function, and trap states of the ETLs, and the defects passivation and energy level matching on the surface of the perovskite layer according to the aforesaid basic interface turning mechanism, and finally effectively improved the performance of PSCs.

#### 4.1.1. Ionic Liquid and Zwitterion

Ionic liquid and the zwitterion containing cations and anions are popular for the interface engineering of PSCs due to their remarkable advantages:[13] 1) possible forming the interfacial dipoles by the molecular chemical adsorption which provides the extra molecular electric field at the interfaces and results in surface charge transfer, as well as the change of the interfacial fermi levels; 2) owing to the abundant cations and anions within the ionic liquid and zwitterion, it is possible to balance the surface charges of interfaces which passivated the traps states within the band gap.

Liu et al. employed $[BMIM]BF_4$ ionic liquid to modify the surface of $TiO_2$. Atomic Force Microscopy (AFM) results find that [BMIM] BF4-modified $TiO_2$ with lower roughness improves the interfacial contact of $TiO_2$/perovskite and reduces carrier recombination. In addition, thanks to the high electrical conductivity of the ionic liquid, the modified $TiO_2$ with higher electron mobility, lower work function, and lower CB assists the electron injection and transporting from perovskite to the $TiO_2$. Finally, the PSCs obtained the certificated efficiency of 19.42%.[66] Snaith et al. further introduced the same ionic liquid on the surface of $SnO_2$, reducing the surface work function, and the device delivered higher efficiency and lower hysteresis.[67] Therefore, the surface modification of ionic liquid on the metal oxide ETLs will effectively improve the interfacial injection and transporting of electrons. In order to match the energy level of ETLs/perovskite, Zhang et al. employed $KBF_4$ to modify the $SnO_2$ ETL; however, the surface $W_F$ increased, and the modified $SnO_2$ exhibits a higher CB, which made it close to the CB of perovskite and benefit for the separation of photo-generated electrons (Figure 5d). Finally, the efficiency of PSCs achieved 22.9% at a low concentration of 0.2 mg $mL^{-1}$ $KBF_4$.[68] Our previous work also employed the $BMIMBF_4$ ionic liquid to modify the PCBM/perovskite interface,

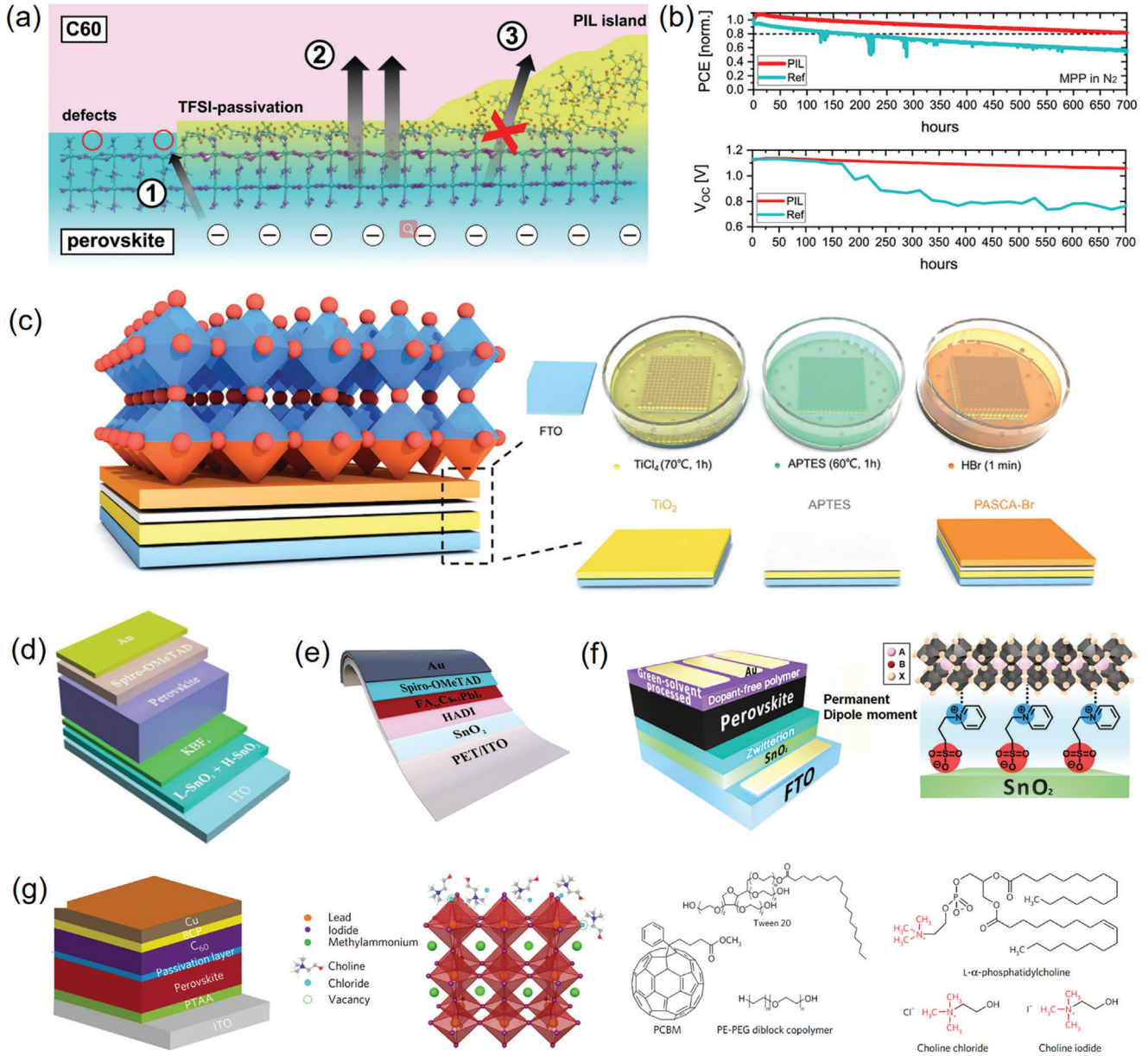


**Figure 5.** Ionic liquid and zwitterion modified the ETL/perovskite interface, a) Schematic representation of passivation mechanism at the perovskite/ETL interface in the presence of PIL;[70] b) The stability of PSCs with or without the PIL modification; Reproduced with permission.[70] Copyright 2021, The Royal Society of Chemistry; c) the illustration of the PASCA-Br modified the ETL/perovskite interface; Reproduced with permission.[74] Copyright 2020, Wiley-VCH; d) the devices structure of $KBF_4$ modified the ETL/perovskite interface; Reproduced with permission.[68] Copyright 2022, American Chemical Society; e) the device structure of HADI modified the ETL/perovskite interface; Reproduced with permission.[73] Copyright 2022, Wiley-VCH; f) the illustration of 3-(1-pyridyl)-1-propane sulfonate modified $SnO_2$ surface and the corresponding device's structure; Reproduced with permission.[13] Copyright 2018, The Royal Society of Chemistry; g) the illustration of PAHs modified the perovskite and $C_{60}$ interface, as well as the molecule structure of PAHs. Reproduced with permission.[6] Copyright 2019, Springer Nature.

which reduced the work function of PCBM, similar to the Liu and Snaith et al. reported. However, the better interface transporting is attributed to the up-shifting of the quasi-fermi level of PCBM, which enlarged the distance with the quasi-fermi level of HTL.[69]

Caprioglio et al. introduce a multi-functional interlayer based on an imidazolium poly-ionic liquid [PeIm][TFSI] at the perovskite/C60 interface (**Figure 5**a). The $TFSI^-$ anion embedded in an insulating polymer matrix reduced the non-radiative recombination across the interfaces. In addition, the interface range of anion and cation of ionic liquid will provide surface dipole to reduce the CB of perovskite, enhancing the interface charge extraction. As a result, the PSCs based on [PeIm][TFSI] obtained 21.4% efficiency with improved FF and $J_{sc}$ for the p-i-n structure, and the [PeIm][TFSI] based device significantly outperformed the reference cell retaining its efficiency at 80% of the initial value after 700 h outputting (Figure 5b).[70]

Liu et al. further employed [BMIM]$BF_4$ as the interface layer of ITO/perovskite to fabricate ETLs-free PSCs, which increased the bendability of the device. Finally, the PCE of flexible PSCs based on ionic liquid is more than 16%.[71] In addition, the $EMIMPF_6$ employed as the interface layer between FTO and perovskite films to prepare PSCs without ETLs obtained an efficiency of 16.2%. It is found that the ionic liquid not only effectively improves the surface work function and conductivity of FTO but also passivates the Pb-cluster trap state within perovskite film through chemical coordination, which reduces the surface recombination of charge carriers and the $V_{oc}$ loss.[72]

Liu et al. modified $SnO_2$ with histamine diiodate (HADI) and obtained an efficiency of 24.79% (Figure 5e). The DFT studies found that the amino terminus of HADI bonds with $Sn^{4+}$ of $SnO_2$, whereas the N atom of the imidazole terminus will interact with the Pb atom of the perovskite to form an effective interfacial linkage. The molecule-semiconductor interaction increased the CB of $SnO_2$, reducing the interfacial transport barrier of carriers. Owing to the chemical coordination between N and Pb-cluster defects, the trap states have also been passivated. Because the interface links increase the bend ductility, the flexible devices retained more than 95% of the original efficiency after 1000 times of bending.[73] To increase the bending stability of flexible PSCs. The ionic amine silane coupling agent (PASCA-Br) was also employed to modify the $TiO_2$/perovskite interface (Figure 5c). The coupling agent strongly bonds with $TiO_2$ and perovskite surface by the chemical interactions. The interactions increased the interfacial mechanical strength and reduced the cracking of perovskite film during bending.[74]

Ammonium fluoride ($NH_4F$) was also employed to modify the $SnO_2$ surface, which reduced defects and tailored the energy level of $SnO_2$ films by surface chemical doping. After the modification, the device achieved a PCE of 23.2%.[75] In addition, the 4-imidazoleacetic acid hydrochloride (ImAcHCl) was reported to modify $SnO_2$ ETL. The results find that the carboxylic acid chemically bonds with the hydroxyl groups of $SnO_2$, and the imidazolium cation electrostatically interacts with the perovskite surface. The treated device achieved the best PCE of 21.0% with negligible hysteresis.[76] Choi et al. introduced 3-(1-pyridyl)-1-propane sulfonate onto the surface of $SnO_2$. It is found that the molecule will effectively reduce the $W_F$ of $SnO_2$ surface from 4.34 eV to 4.23 eV, improving the interfacial energy level matching and the $E_{bi}$. In addition, the dipole toward perovskite inhibited the surface charge recombination and passivated the $PbI_3^-$ anti-defect. Finally, the performance of PSCs improved to 21.43%.[13] Furthermore, the quaternary ammonium halides (QAHs) as the interlayers of perovskite/PCBM were reported to passivate negative ($PbI_3^-$ anti-defects) and positive-charged components (Pb-cluster) ionic defects of perovskite (Figure 5g). The DFT study finds the QAHs will eliminate the trap states at the VB side of perovskite for $PbI_3^-$ anti-defects and reduce the trap states at the CB side of the Pb-cluster. Finally, the defect passivation reduces the $V_{oc}$ deficit of PSCs to 0.39 V and boosts the PCE to a certified value of 20.59±0.45%, as well as improves the device's stability.[6]

Our previous work employed potassium L-aspartate (PL-A) and developed a self-diffusion interfacial doping method to restrain the carrier trap-induced recombination via the reconstruction of energy level structure at $SnO_2$/perovskite interface. The PL-A anions will remain at the $SnO_2$ surface by strong chemical adsorption. However, the cations gradually diffuse into perovskite and endow an n-doping effect during the spin-coating of the perovskite film. Finally, 23.74% PCE for the PL-A modified devices was obtained.[77] The ionic liquid and zwitterions at ETL/perovskite for the PCE and stability have been illustrated in **Table 1**.

#### *4.1.2. Small Molecule*

In addition to ionic liquids and zwitterions, small molecule interface modifications have also been extensively reported. The specific atoms of a small molecule (such as N, O, S, and F) will bond with the surface chemical sites of ETL or perovskite as the surface dipole or self-assembling monolayer (SAM), transferring the surface electrons and thus change the $E_F$ shifting and passivated the trap states of semiconductors.

Qin et al. employed formamidine sulfinic acid (FSA) to modify the $SnO_2$ surface. In addition to reducing the work function of $SnO_2$, 2D-GWIAXS studies show (**Figure 6**a,b) that the FSA will effectively regulate the orientation of $PbI_2$ at the (001) plane, and reduces the residual $PbI_2$ after the formation of perovskite film which inhibits the interface defects formation of perovskite film. Finally, the PCE of PSCs based on $FAPbI_3$ perovskite is more than 24%.[78] The N atom containing 2-methyl benzimidazole (MBIm) was also employed as the interlayers of $SnO_2$/perovskite. Introducing MBIm will not change the grain size of the perovskite film, but it increases the adhesion of the perovskite film on the surface of $SnO_2$ ETL and improve the interfacial contact of $SnO_2$/perovskite. In addition, the N atom of MBIm coordinated with the $Pb^{2+}$ of perovskite to reduce the atomic defect at the interfaces. Owing to the interfacial connection and passivation, the $V_{oc}$ of PSCs increased from 1.09 V to 1.15 V.[79] Li et al. synthesized the S and O atoms containing organometallic compound ($FcTc_2$) and employed them at the perovskite/$C_{60}$ interface (Figure 6c). The MD found that $FcTc_2$ provided strong chemical Pb–O binding to reduce surface trap states of perovskite and increased the carrier lifetime over 2 µs (Figure 6d). In addition, it accelerated interfacial electron transfer through the electron-rich and electron-delocalized ferrocene units. The resulting devices achieved a certified PCE of 24.3% and maintained >98% of their initial efficiency during long-term operational stability tests over 1500 h.[80]

Wang et al. introduce Lewis's base thiophene or thiazole-modified $C_3N_4$ layer at the $TiO_2$/perovskite interface to constitute a stepwise energy band alignment and passivate interface defects. The thiophene and thiazole donate the lone pair electrons of S or N atoms to the under-coordinated $Pb^{2+}$, which passivated the electronic trap states caused by halogen vacancies, minimizing trap-assisted non-radiative recombination of PSCs, the thiazole-$C_3N_4$-based devices obtained higher $V_{oc}$ of 1.11 V and improved stability.[81]

Electron acceptor materials on the semiconductor surface can effectively change the properties of the semiconductor materials. Lou et al. synthesized $\pi$-conjugated N-type small molecule (BTAC4) and employed it to modify the $SnO_2$ ETL. Similarly, the surface-regulated $SnO_2$ exhibits better-matched interfacial energy levels to assist the injection of photo-generated carriers

**Table 1.** The ionic liquids and zwitterions employed at the ETL/perovskite interface for improving the efficiency and stability of PSCs.

| Materials | ETL | Perovskite | Structure | [$J_{sc}$ / mA cm$^{-2}$] | [$V_{oc}$ / V] | FF | PCE / % | Stability | Ref. |
|---|---|---|---|---|---|---|---|---|---|
| [BMIM]$BF_4$ | $TiO_2$ | $MAPbI_3$ | n-i-p | 22.75 | 1.12 | 0.77 | 19.62 | - | 2016[66] |
| [BMIM]$BF_4$ | $SnO_2$ | $FA_{0.83}MA_{0.17}Pb(I_{0.83}Br_{0.17})_3$ | n-i-p | 22.7 | 1.16 | 0.79 | 20.8 | – | 2019[67] |
| $KBF_4$ | $SnO_2$ | $FA_{0.925}MA_{0.05}Cs_{0.025}Pb(I_{0.95}Br_{0.05})_3$ | n-i-p | 25.1 | 1.137 | 0.824 | 22.90 | 85% (1000 h, RH 70 ± 10%) | 2022[68] |
| [BMIM]$BF_4$ | PCBM | $Cs_{0.05}(FA_{0.85}MA_{0.15})_{0.95}Pb(I_{0.85}Br_{0.15})_3$ | n-i-p | 22.66 | 1.14 | 0.8083 | 20.88 | 88% (60 days, ambient condition) | 2019[69] |
| [PeIm][TFSI] | $C_{60}$ | $Cs_{0.05}(MA_{0.17}FA_{0.83})_{0.95})Pb(I_{0.83}Br_{0.17})_3$ | p-i-n | 22.54 | 1.158 | 0.8193 | 21.39 | 80%(700 h, 1 sun, $N_2$) | 2021[70] |
| [BMIM]$BF_4$ | – | $(FAPbI_3)_{0.85}(MAPbBr_3)_{0.15}$ | Flexible n-i-p | 22.72 | 1.07 | 0.662 | 16.09 | – | 2016[71] |
| $EMIMPF_6$ | – | $(FAPbI_3)_{0.87}(MAPbBr_3)_{0.13}$ | n-i-p | 20.4 | 1.09 | 0.729 | 16.2 | – | 2021[72] |
| HADI | $SnO_2$ | $FA_{0.9}Cs_{0.1}PbI_3$ | Flexible n-i-p | 24.64 | 1.17 | 0.7816 | 22.44 | 91% (50 days, RH 35%) | 2022[73] |
| PASCA-Br | $TiO_2$ | $Cs_{0.05}(FA_{0.85}MA_{0.15})_{0.95}Pb(I_{0.85}Br_{0.15})_3$ | n-i-p | 24.58 | 1.14 | 0.77 | 21.66 | – | 2020[74] |
| $NH_4F$ | $SnO_2$ | $(FAPbI_3)_{0.95}(MAPbBr_3)_{0.05}$ | n-i-p | 24.6 | 1.16 | 0.814 | 23.2 | – | 2020[75] |
| ImAcHCl | $SnO_2$ | $FA_{0.95}MA_{0.05}PbI_{2.85}Br_{0.15}$ | n-i-p | 23.06 | 1.152 | 0.79 | 20.96 | 94%(35 days, RH 40–60%) | 2019[76] |
| 3-(1-pyridinio) 1-propanesulfonate, | $SnO_2$ | $FA_{0.83}MA_{0.17}Pb(I_{0.83}Br_{0.17})_3$ | n-i-p | 23.6 | 1.16 | 0.784 | 21.43 | 70% (140 h RH 85% 85°C) | 2018[13] |
| QAHs | $C_{60}$ | $FA_{0.85}MA_{0.15}Pb(I_{0.85}Br_{0.15})_3$ | p-i-n | 23.7 | 1.14 | 0.78 | 21 | 100% (30 days, ambient condition) | 2017[77] |
| PL-A | $SnO_2$ | $FA_{0.95}MA_{0.05}Pb(I_{0.95}Br_{0.05})_3$ | n-i-p | 24.5 | 1.20 | 0.8172 | 23.74 | 93% (1500 h, RH 20%) | 2022[78] |

to ETL. It is worth noting that the modification of small N-type molecules improves the surface conductivity of $SnO_2$, which may attribute to surface electron transfer. It further assists the carrier transporting at the ETL/perovskite interface and improves the PCE of PSCs.[82] Zhang et al. employed graphdiyne (GYD) as the surface modification material of $SnO_2$. The results found that the introduction of GYD improved the $W_F$ of the $SnO_2$ surface and enhanced the process of interfacial electron injection from the perovskite layer to ETL. DFT study finds that the increasing of $W_F$ is attributed to the transfer of electrons from the $SnO_2$ to graphite acetylene. In addition, interfacial graphite alkyne effectively reduces the charge accumulation at the $PbI_3^-$ anti-defects perovskite films. Thus, the PCE of PSCs increased from 18.79% to 20.74%.[26] Wang et al. combined graphene with N-type organic small molecules (NDI) to modify the $SnO_2$/perovskite interface. The NDI-graphene layers not only enhanced the conductivity and carrier transporting of $SnO_2$ but also interacted with FAI and MAI of perovskite films via van der Waals interaction, thus enhancing the interfacial stability of PSCs. Finally, the PSCs based on the composites achieved a high fill factor of 82%.[86]

In addition to the direct passivation of ETL and perovskite by the small molecules, the anchoring of molecules on ETL as the SAM provides the surface dipole to transfer the surface electron of semiconductors or reduce the surface defects of materials. Tu et al. found that the surface-anchored P=O functional group of triphenylphosphine oxide (TPPO) could form an effective surface N-type doping on the electron transport layer of $SnO_2$ through the surface charge transfer by its dipole (Figure 6f). The surface doping not only reduces the $W_F$ of $SnO_2$ surface and increases the $E_{bi}$ of the interface but also causes the band bending of perovskite film to connect the CB between the ETL/perovskite interface, thus improving the carrier injection and transporting.[38] The position of a functional group of a molecule will change the molecular dipoles when anchored with the ETL. Han et al. compared the 4-methoxybenzoic acid (MBA), 3, 4-dimethoxybenzoic acid (DMBA), and 3, 4, 5-Trimethoxybenzoic acid (TMBA) interlayers on the influence of the interface of PSCs. The carboxyl terminus of molecules anchored on the ZnO surface and formed a surface dipole. By controlling the position and number of substitutions of different methoxy groups on the cyclobenzene, the dipole moment of the surface increased to 13.2 Debye (D) for the TMBA. Finally, the $W_F$ of ZnO reduced from 4.61 eV to 4.39 eV, which effectively improves the electron injection at this interface.[32] Dai et al. employed trimethoxy silane (H-SAM) and (3-iodopropyl) trimethoxy silane (I-SAM) monolayers on the surface of $SnO_2$ film to relieve the interfacial stress between ETL and perovskite, thus improving the stability of the corresponding PSCs (Figure 6e). Owing to the strong interaction between iodine and Pb atoms, the toughness at ETL/perovskite interface increased 50%, enhancing the PSCs' mechanical reliability. In addition, the I-SAM-modified device achieves superior PCE (21.4%) and lower photovoltaic hysteresis due to better interface matching via the surface dipole.[84] The introduction of monolayers relieves the interfacial stress and influences the crystal growth of

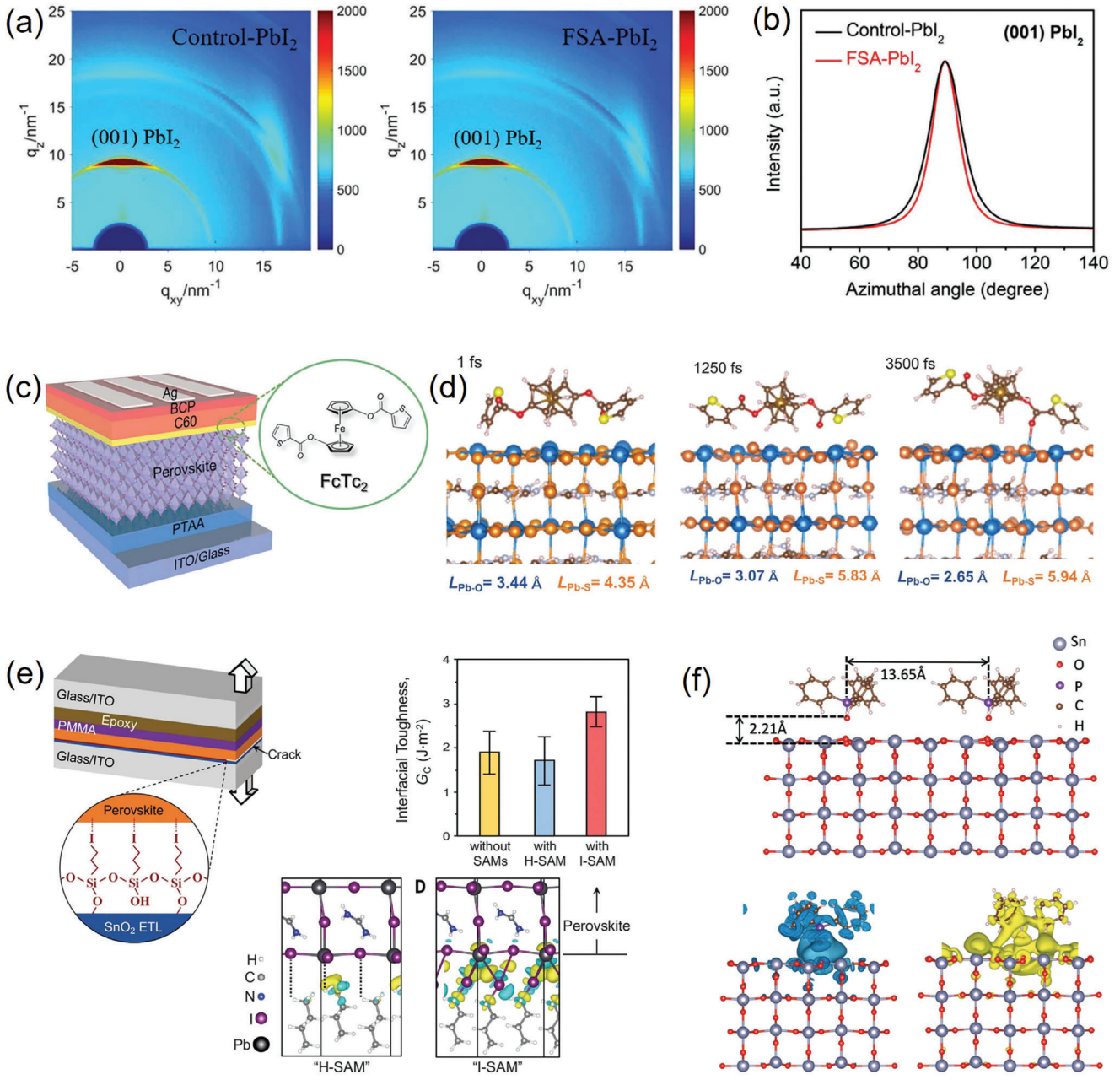


**Figure 6.** The small molecules modified the ETL/perovskite interface, a) The 2D GIWAXS patterns of the control and FSA-$PbI_2$ films;[78] b) the intensity azimuthal graph of (001) diffraction of $PbI_2$ prepared under both conditions 2D-GIWAXS patterns of the control and FSA-$PbI_2$ films; Reproduced with permission.[78] Copyright 2022, Wiley-VCH; c) the schematic illustration of inverted PSC based on $FcTc_2$ as the interface;[80] d) the molecular dynamics simulations of the interaction between perovskite and $FcTc_2$; Reproduced with permission.[80] Copyright 2022, Springer Nature; e) the schematic illustration of the sandwich for toughness testing, and toughness of ETL/Perovskite interface without SAMs and ones with H-SAM or I-SAM, as well as the charge density difference plots from DFT calculations; Reproduced with permission.[84] Copyright 2021, American Association for the Advancement of Science; f) the side-view of the relaxed model of TPPO absorbed $SnO_2$ (110) surface and the charge density difference of TPPO on $SnO_2$ (110) surface; Reproduced with permission.[37] Copyright 2019, Wiley-VCH.

perovskite films. Shi et al. obtained monolayer-modified $SnO_2$ film by soaking it in 3-Mercutopropyl trimethoxysilane (MPTMS) solution. Perovskite films achieved grain size over 1 µm under 3 h immersion conditions, and the efficiency of PSCs increased to 20.03% based on the method.[85] Hou et al. introduced dopamine (DA) SAM on the surface of $SnO_2$, which the hydroxyl group of dopamine effectively anchored on the Sn atom to form strong coordination. The exposed amino terminus interacted with perovskite film, which could reduce the surface defects of perovskite. Furthermore, it increased the grain size of perovskite from 1 µm to 2 µm, further reduced the grain boundary defects of perovskite, and improved the PCE.[87]

**Table 2.** The small molecule employed at the ETL/perovskite interface for improving the efficiency and stability of PSCs.

| Materials | ETL | Perovskite | Structure | $[J_{sc}$ / mA cm$^{-2}]$ | $[V_{oc}$ / V] | FF | PCE / % | Stability | Ref. |
|---|---|---|---|---|---|---|---|---|---|
| FSA | $SnO_2$ | $FAPbI_3$ | n-i-p | 25.43 | 1.166 | 0.813 | 24.1 | 85% (1000 h MPP, 50 °C) | 2022[78] |
| MBIm | $SnO_2$ | $Cs(FAPbI_3)_x(MAPbBr_3)_{1-x}$ | n-i-p | 23.41 | 1.195 | 0.77 | 21.25 | 90% (250 h, 50±5% RH) | 2020[79] |
| $FcTc_2$ | $C_{60}$ | $(FA_{0.98}MA_{0.02})_{0.95}Pb(I_{0.98}Br_{0.02})_3$ | p-i-n | 25.59 | 1.179 | 0.806 | 24.3 | 98%(1500 h, MPP, $N_2$) | 2022[80] |
| Thiazole-$C_3N_4$ | $TiO_2$ | $(FAPbI_3)_{0.875}(CsPbBr_3)_{0.125}$ | n-i-p | 22.50 | 1.11 | 0.77 | 19.23 | – | 2021[81] |
| BACT4 | $SnO_2$ | $Cs_{0.05}(FA_{0.85}MA_{0.15})_{0.95}Pb(I_{0.85}Br_{0.15})_3$ | n-i-p | 24.2 | 1.252 | 0.761 | 23.06 | 98% (30 days, RH 35%) | 2021[82] |
| GYD | $SnO_2$ | $CsFAMAPbI_3$ | n-i-p | 23.32 | 1.137 | 0.7962 | 21.11 | – | 2020[26] |
| NDI-graphene | $SnO_2$ | $FA_{0.75}MA_{0.15}Cs_{0.1}PbI_{2.65}Br_{0.3}$ | n-i-p | 22.66 | 1.084 | 0.821 | 20.16 | – | 2018[83] |
| TPPO | $SnO_2$ | $Cs(FAPbI_3)_x(MAPbBr_3)_{1-x}$ | n-i-p | 24.30 | 1.106 | 0.769 | 20.69 | – | 2021[38] |
| TMBA | ZnO | $MAPbI_3$ | n-i-p | 21.38 | 1.05 | 0.61 | 13.75 | 66.81% (7 days, RH 45%) | 2019[32] |
| I-SAM | $SnO_2$ | $Cs_{0.05}(FA_{0.85}MA_{0.15})_{0.95}Pb(I_{0.85}Br_{0.15})_3$ | n-i-p | 23.26 | 1.185 | 0.778 | 21.44 | 80% (3921 h, MPP, $N_2$) | 2021[84] |
| MPTMS | $SnO_2$ | $Cs(FAPbI_3)_x(MAPbBr_3)_{1-x}$ | n-i-p | 23.60 | 1.112 | 0.7632 | 20.03 | 90% (30 days, RH 30%) | 2021[85] |
| Dopamine | $SnO_2$ | $MAPbI_3$ | n-i-p | 21.80 | 1.05 | 0.739 | 16.87 | 80% (300 h, RH 70%) | 2018[86] |
| 5-AVA | – | $FA_{0.9}Cs_{0.1}PbI_{3-x}Cl_x$ | n-i-p | 23.91 | 1.08 | 0.75 | 19.37 | – | 2021[87] |
| PMSME | – | $FA_{0.85}MA_{0.15}Pb(I_{0.85}Br_{0.15})_3$ | n-i-p | 23.62 | 1.15 | 0.7567 | 20.55 | – | 2020[88] |

The surface SAMs are also used to improve the surface $W_F$ of ITO and fabricated ETL-free PSCs with high PCE. Wang et al. introduced the polar 5-aminovaleric acid (5-AVA) monolayer onto the surface of ITO, reduced its surface work function from 4.70 eV to 4.12 eV, and finally achieved 19.37% efficiency of PSCs without ETL.[87] Huang et al. synthesized small molecule electrolytes (PMSME) and employed them as the SAM for ITO, which increased the efficiency of this kind of solar cell to 20.55%.[88] The detailed photovoltaic parameters and stability are summarized in **Table 2**.

#### *4.1.3. Fullerene Derivative*

Fullerene and the derivatives have been widely employed as the interfacial layers of ETL/perovskite due to the outstanding electronic properties and the suitable energy level that matches perovskite. Except for the better transfer of the interfacial electron, the functional fullerene chemically bonds with the metal atoms at the ETL/perovskite interface and thus passivates the trap states. In addition, the nature of the accepter electron of fullerene itself will further shift the trap states of anion defects of perovskite, consistent with the discussed passivation mechanism for the acceptors.

Huang et al. synthesized the hydroxylated $C_{60}$ and employed it as an interlayer between $TiO_2$ and perovskite layers. The excellent electron conductivity of hydroxylated $C_{60}$ resulted in significantly enhanced electron transfer from perovskite to $TiO_2$. In addition, the higher LUMO of the hydroxylated $C_{60}$ (−4.27 eV) than $TiO_2$ (−4.35 eV) reduced the interfacial recombination and improved the PCE of PSCs.[89] Chavan et al. integrated gold nanoparticles functionalized with fully conjugated fullerene derivative ($C_{60}$-BCT@Au NPs) as ETL/perovskite interface layers. The interfacial contact not only improved the crystallinity and morphology of perovskite films but also improved the charge extraction efficiency from the perovskite to $TiO_2$ via the suitable and higher CB of the fullerene $C_{60}$ derivative. The device yields an efficiency of 19.08% with improved stability.[90] Zhou et al. used PCBM and $C_{60}$-ETA as a double-layer $TiO_2$ modification layer, which effectively increased the photo-generated current density of PSCs from 18.33 mA cm$^{-2}$ to 21.96 mA cm$^{-2}$.[91] Zhang et al. designed the iodide functional fullerene derivative (PCBB-3N-3I) to passivate interface defects and reconfiguration the interfacial energy of perovskite/PCBM. Due to the electrostatic interaction, PCBB-3N-3I not only passivates surface defects positively but also assembles on top of the perovskite with the preferred orientation (Figure 7b). The PCBB-3N-3I exhibits a strongly molecular electric dipole to reconfigure the interfacial energy band, leading to enhanced $E_{bi}$ and charge collection. As a result, the PSCs exhibit a promising PCE of 21.1% with robust ambient stability.[92]

Zhan et al. introduced the fullerene derivative C9 on the surface of $SnO_2$ film, and the hydroxyl terminal of C9 molecule was effectively anchored on the surface of $Sn^{4+}$ and filled oxygen vacancies, thus passivated the defect state caused by the surface non-equilibrium charge (**Figure 7**a). By employing the C9, the efficiency of PSCs was increased from 20% to 21.3% with a higher FF of 0.789.[93] Wang et al. employed ultrafast transient absorption spectroscopy to study the photocarrier dynamics across fullerene derivative-modified $SnO_2$ ETLs. The $C_{60}$ pyrrolidine tris-acid (CPTA)-modified $SnO_2$ ETL and PCBM-modified $SnO_2$ ETL exhibit favorable energy band energy alignment to perovskites, resulting in a better electron injection rate compared to

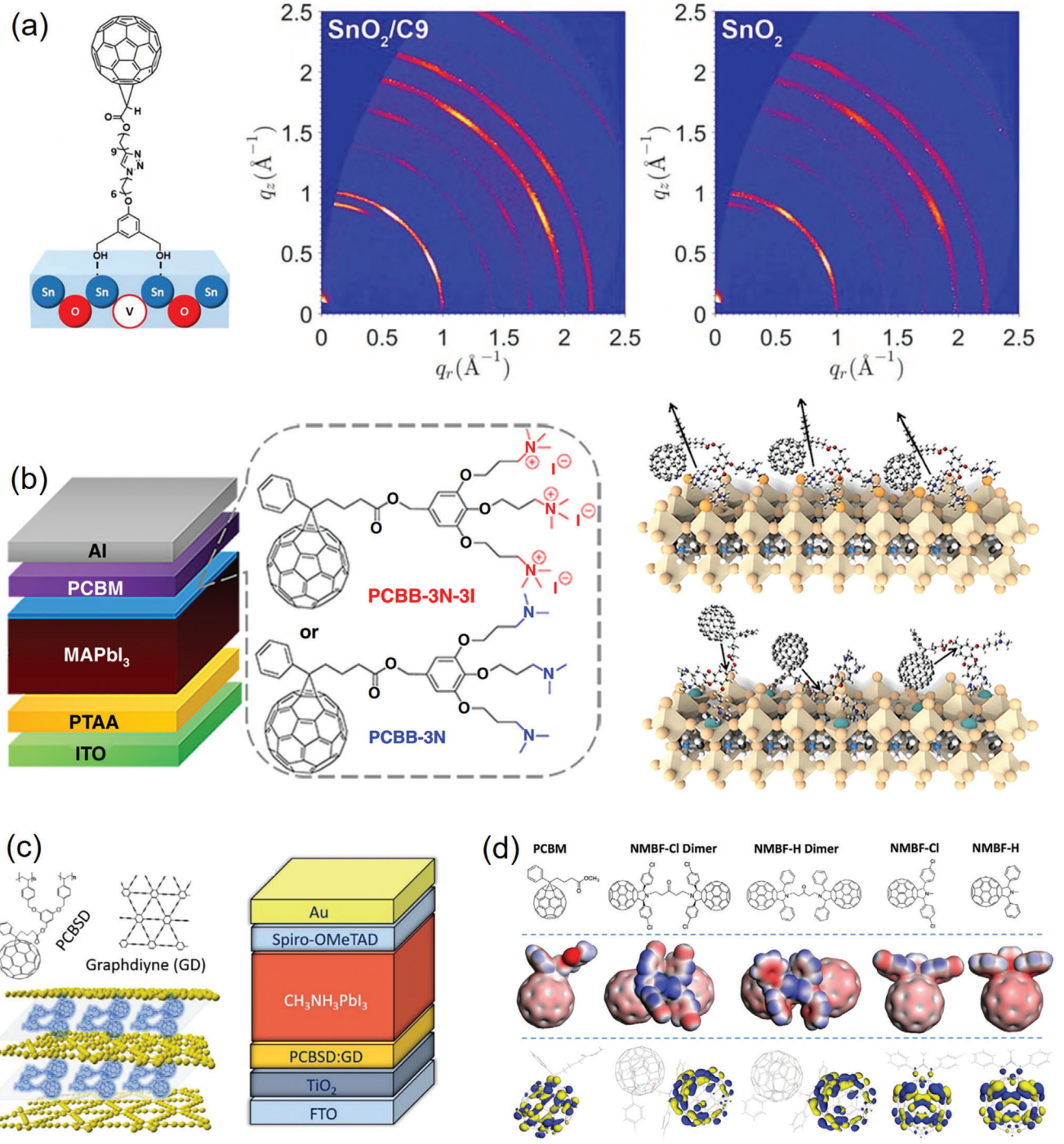


**Figure 7.** The fullerene derivatives modified the ETL/perovskite interface. a) The molecule structure of C9 and the mechanism of the passivation, as well as the GIWAXS patterns of perovskite based on C9-modified $SnO_2$ and the bare $SnO_2$; Reproduced with permission.[93] Copyright 2018, The Royal Society of Chemistry; b) the illustration of PSCs with and without PCBB-3N-3I/PCBB-3N treatment on perovskite, as well as the illustration of molecules dipole orientation; Reproduced with permission.[92] Copyright 2019, Springer Nature; c) the illustration of graphdiyne doped PCBSD as the interlayers between ETL and perovskite; Reproduced with permission.[96] copyright 2018, Elsevier; d) the chemical structures of fullerene monomers and dimers, as well as the electronic properties of the fullerene derivatives; Reproduced with permission.[97] Copyright 2020, Wiley-VCH.

**Table 3.** The Fullerene derivative employed at the ETL/perovskite interface for improving the efficiency and stability of PSCs.

| Materials | ETL | Perovskite | Structure | $J_{sc}$ / mA cm$^{-2}$] | [$V_{oc}$ / V] | FF | PCE / % | Stability | Ref. |
|---|---|---|---|---|---|---|---|---|---|
| $C_{60}(OH)_{24\text{-}26}$ | $TiO_2$ | $MAPb(I_xCl_{1-x})_3$ | n-i-p | 20.91 | 0.95 | 0.715 | 14.69 | – | 2016[89] |
| $C_{60}$-BTC@Au | $TiO_2$ | $Cs_{0.05}(MA_{0.17}FA_{0.83})_{0.95}Pb(I_{0.83}Br_{0.17})_3$ | n-i-p | 22.96 | 1.138 | 0.7581 | 19.08 | 90% (200 h, MPP, UV-light) | 2020[90] |
| $C_{60}$-ETA | $TiO_2$ | $MAPbI_3$ | n-i-p | 23.76 | 1.06 | 0.693 | 17.09 | – | 2017[91] |
| PCBB-3N-3I | PCBM | $MAPbI_3$ | p-i-n | 23.46 | 1.105 | 0.8136 | 21.10 | 87% (150 h, RH 40–50%) | 2019[92] |
| C9 | $SnO_2$ | $(FAPbI_3)_x(MAPbBr_3)_{1-x}$ | n-i-p | 24.1 | 1.12 | 0.789 | 21.3 | 82% (90 days, RH 15±5%) | 2018[93] |
| CPTA | $SnO_2$ | $FA_{0.66}MA_{0.34}PbI_{2.85}Br_{0.15}$ | n-i-p | 22.2 | 1.10 | 0.76 | 18.6 | – | 2019[94] |
| Y3N@$C_{80}$ | $SnO_2$ | $Cs(FAPbI_3)_x(MAPbBr_3)_{1-x}$ | n-i-p | 24.24 | 1.14 | 0.7838 | 21.66 | – | 2022[95] |
| PCBSD:GD | $TiO_2$ | $MAPbI_3$ | n-i-p | 23.30 | 1.11 | 0.78 | 20.19 | 80% (500 h, RH 25%-30%) | 2018[96] |
| NMBF-Cl dimer | $SnO_2$ | $(FAPbI_3)_x(MAPbBr_3)_{1-x}$ | n-i-p | 25.5 | 1.12 | 0.78 | 22.3 | 98% (1000 h, ambient condition) | 2020[97] |

the bare $SnO_2$ ETL. Moreover, the carboxylic acids of CPTA will interfacial chemical bond to $SnO_2$ surface, thus establishing interface dipoles. The chemisorption of the CPTA fullerene functions as a recombination suppressor both at the CPTA-passivated $SnO_2$/perovskite interface and inside perovskite.[94] The endohedral metallofullerenes (EMFs, $Y_3N@C_{80}$) were synthesized by Zhou et al. as an interfacial modifier of $SnO_2$ ETL. The interface modification significantly increased $V_{oc}$ from 1.106 V to 1.14 V and increased PCE from 20.59% to 21.66%, which were attributed to the more suitable CB energy levels and more effective electron extraction at the $SnO_2$/$Y_3N$@C80/perovskite interface. In addition, the stability of the modified devices was also improved.[95] In addition, graphdiyne (GD) has also been introduced into fullerene derivatives (PCBSD) as N-type dopants to modify the $TiO_2$ surface (Figure 7c). Finally, the modified $TiO_2$ have a better interface match with perovskite film and improved the corresponding PSCs efficiency to 20.19%.[96] Recently, chlorinated fullerene dimers were used for interfacial metal oxides/perovskite (Figure 7d). The chlorinated fullerene dimers coordinated with metal oxides and perovskite via the chlorine terminals. The planar PSCs deliver a maximum PCE of 22.3% without hysteresis while maintaining over 98% of initial efficiency after storage for 1000 h.[97] The detailed photovoltaic parameters and stability are summarized in **Table 3**.

#### *4.1.4. Metal Salts*

Metal salts are also employed to match the interfacial energy level by the surface doping or the bilayers ETLs and passivate the surface trap states of perovskite via coordination. Tavakoli et al. designed the amorphous $SnO_2$ (a-$SnO_2$) as the interfacial layer at the $TiO_2$/perovskite and improved the PCE to 21.4% by turning the energy level of ETLs.[98] The $SnO_2$ is also employed on the $In_2O_3$ ETL surface to form the gradient energy level at the ETLs and assist the electron transportation, thus boosting the PCE of planar PSCs to 23.24% along with the higher $J_{sc}$ (24.53 mA cm$^{-2}$) and FF (0.8123)[99] In addition, the Sb-$SnO_2$$SnO_2$/bilayer ETLs also result in better PCE.[100] Chavan et al. employed the atomics deposition methods to fabricate the TiN layers on the m-$TiO_2$. Owing to the better interfacial energy level match and the surface interaction with perovskite, the devices based on TiN exhibit higher PCE and stability and negligible hysteresis.[101] The $La_2O_3$ also have been employed on the m-$TiO_2$ as the surface modifier, resulting in better interfacial carrier transportation.[102] Huang et al. synthesized the water-soluble 2D $TiS_2$ to modify the $SnO_2$ ETLs (**Figure 8**e). The $TiS_2$-based ETL with higher CB reduced the interfacial carrier recombination. As the interfacial chemical bonding of Pb–S, perovskite defects also have been passivated and improved the PCE to 21.7% for the planar devices.[103]

Metal halide is also widely employed on ETLs. Zhang et al. dissolved $PbI_2$ in HMP as a $TiO_2$ interface modification layer, and the device using PTAA as HTM achieved a PCE of 19.5%. Further studies have found that interfacial $PbI_2$ can effectively regulate the crystal growth process of perovskite thin films, thereby reducing the film trap states and improving the efficiency of PSCs.[104] CsI modifies the m-$TiO_2$ surface reported by Han et al. to reduce $W_F$ of ETL and results in enhanced $E_{bi}$, which promotes charge separation and collection.[105] Wang et al. introduced RbF into the interface between $SnO_2$ and perovskite, and the results found that the F atom interacts with the oxygen vacancy of $SnO_2$, while Rb atom interacts with the surface exposed oxygen atoms, which reduced the surface defects of $SnO_2$. The perovskite film based on surface-modified RbF exhibits a longer fluorescence lifetime than that that RbF doped with $SnO_2$, indicating the better passivation effect of perovskite by the interface modification. Finally, the PCE of a device based on interfacial RbF boosted to 23.38%, and it also increased the $J_{sc}$ and FF to 24.32 mA cm$^{-2}$ and 0.7939.[106] The Cl-based metal halide is popular for interfacial modification. Wang et al. adopted $NiCl_2$ as a modifier on $SnO_2$ and passivated the interface of ETL/perovskite. The devices based on $NiCl_2$ achieved a high $V_{oc}$ (1.17 V) due to the increased energy level of the CB.[107] Min et al. reported the formation of an interlayer between a $SnO_2$ and perovskite, achieved by

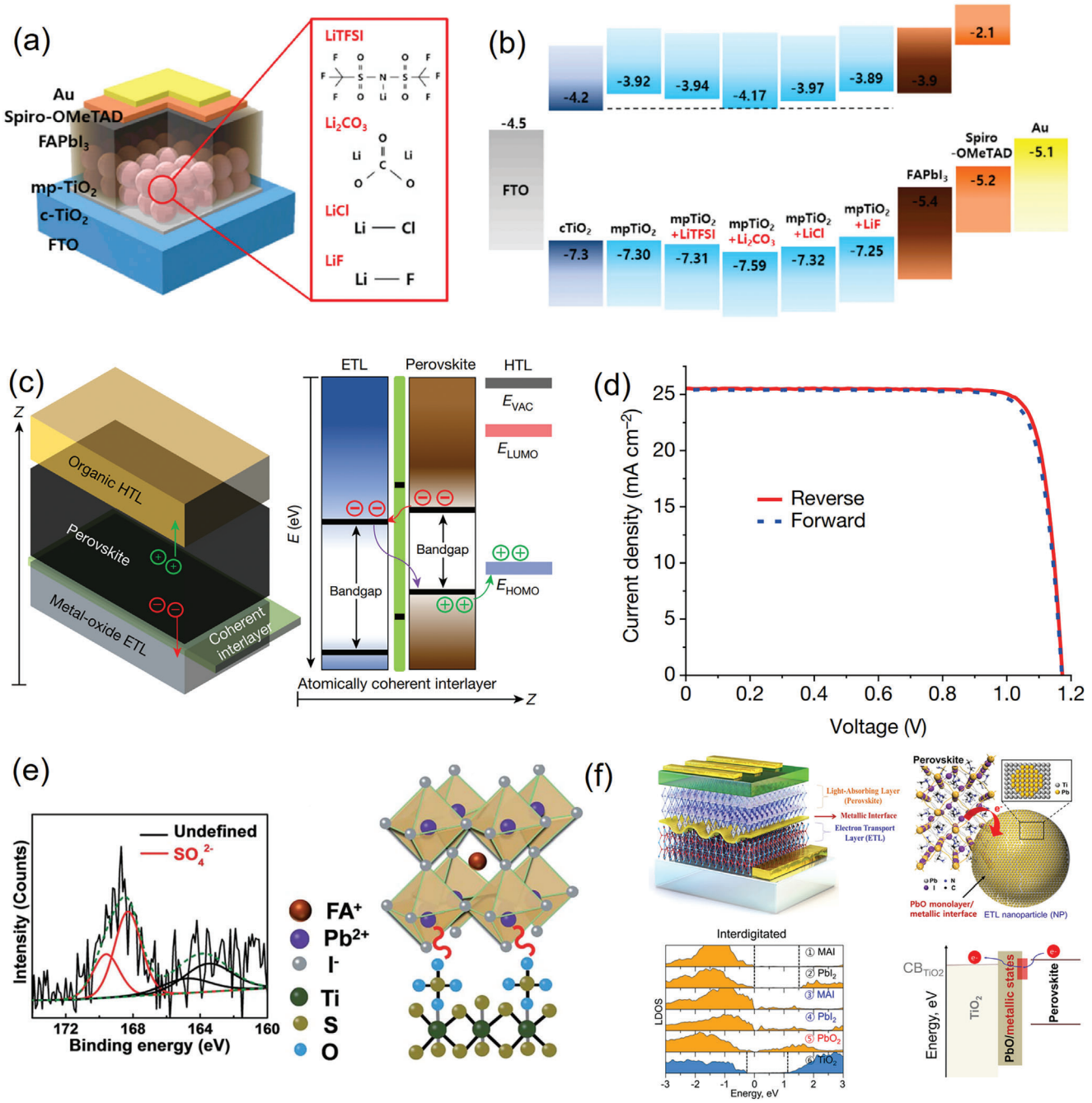


**Figure 8.** The metal salt modified the ETL/perovskite interface. a) The different Li salt modified the $TiO_2$ surface;[110] b) the illustration of energy level of the $TiO_2$ modified different Li salt; Reproduced with permission.[110] Copyright 2021, Elsevier; c) the Cl atoms passivate the ETL/perovskite interface;[108] d) the *J–V* curve of Cl atoms passivate the ETL/perovskite interface; Reproduced with permission.[108] Copyright 2021, Springer Nature; e) the XPS and the illustration of $TiS_2$ interacted with perovskite film; Reproduced with permission.[103] Copyright 2019, The Royal Society of Chemistry; f) the illustration of PbO modified the ETL/perovskite interface, and the DOS of the $TiO_2$/PbO/perovskite hetero-junction, as well as the energy level of metallic states introduced by PbO; Reproduced with permission.[111] Copyright 2021, American Chemical Society.

coupling Cl-bonded $SnO_2$ with a Cl-containing perovskite precursor (Figure 8c). This interlayer has atomically coherent features, which enhance charge extraction and transport from the perovskite layer and have fewer interfacial defects. Such a coherent interlayer allowed us to fabricate PSCs with a certificated PCE of 25.5% with an excellent FF of 0.832 (Figure 8d). Furthermore, unencapsulated devices maintained ≈ 90%of their initial efficiency even after continuous light exposure for 500 h.[108] As the passivation of the halogen atom, the I atoms are also introduced in the graphene quantum dots as the interfacial materials to improve the PCE of PSCs further.[109] Kim et al. compared the electrical properties of different Li-salt (LiTFSI, $Li_2CO_3$,

**Table 4.** The metal salts employed at the ETL/perovskite interface for improving the efficiency and stability of PSCs.

| Materials | ETL | Perovskite | Structure | [$J_{sc}$ / mA cm$^{-2}$] | [$V_{oc}$ / V] | FF | PCE / % | Stability | Ref. |
|---|---|---|---|---|---|---|---|---|---|
| a-$SnO_2$ | $TiO_2$ | $(Cs_{0.05}MA_{0.15}FA_{0.85}Pb(I_{0.85}Br_{0.15})_3$ | n-i-p | 23.91 | 1.169 | 0.765 | 21.4 | 91% (500 h, light illumination) | 2018[98] |
| $SnO_2$ | $In_2O_3$ | $FAMAPbI_3$ | n-i-p | 24.53 | 1.16 | 0.8123 | 23.07 | 97.5% (80 days, $N_2$) | 2020[99] |
| $SnO_2$ | Sb-$SnO_2$ | $Cs_{0.05}(FA_{0.85}MA_{0.15})_{0.95}Pb(I_{0.85}Br_{0.15})_3$ | n-i-p | 23.90 | 1.173 | 0.74 | 20.73 | – | 2019[100] |
| TiN | $TiO_2$ | $MA_{0.17}FA_{0.83}Pb(I_{0.83}Br_{0.17})_3$ | n-i-p | 22.83 | 1.148 | 0.7625 | 19.38 | 80% (500 h, RH 40%) | 2020[101] |
| $La_2O_3$ | $TiO_2$ | $MAPbI_3$ | n-i-p | 20.84 | 1.01 | 0.7464 | 15.81 | – | 2016[102] |
| $TiS_2$ | $SnO_2$ | $(FAPbI_3)_x(MAPbBr_3)_{1-x}$ | n-i-p | 24.57 | 1.11 | 0.794 | 21.73 | – | 2019[103] |
| $PbI_2$ | $TiO_2$ | $MAPbI_3$ | n-i-p | 22.53 | 1.08 | 0.801 | 19.5 | – | 2016[104] |
| CsI | $TiO_2$ | $MAPbI_3$ | n-i-p | 21.01 | 1.03 | 0.79 | 17.1 | 66% (60 days, ambient condition) | 2017[105] |
| RbF | $SnO_2$ | $Cs(FAPbI_3)_x(MAPbBr_3)_{1-x}$ | n-i-p | 24.32 | 1.213 | 0.7929 | 23.38 | – | 2021[106] |
| NiCl | $SnO_2$ | $MAPbI_3$ | n-i-p | 22.74 | 1.17 | 0.731 | 19.46 | – | 2019[107] |
| $SnO_2$-Cl | $SnO_2$ | $FAPbI_3$ | n-i-p | 25.71 | 1.1885 | 0.832 | 25.5 | 90% (500 h, MPP, ambient condition) | 2021[108] |
| I-GQDs | $SnO_2$ | $FAPbI_3$ | n-i-p | 25.42 | 1.073 | 0.82 | 22.37 | 84% (600 h, MPP, $N_2$) | 2021[109] |
| $Li_2CO_3$ | $TiO_2$ | $FAPbI_3$ | n-i-p | 26.17 | 1.171 | 0.8247 | 25.28 | 95.5% (528 h, MPP) | 2021[110] |
| PbO | $TiO_2$ | $Cs_{0.05}(FA_{0.85}MA_{0.15})_{0.95}Pb(I_{0.85}Br_{0.15})_3$ | n-i-p | 23.5 | 1.15 | 0.78 | 21.2 | 95% (13 days, RH 20%-30%) | 2021[111] |

LiCl, and LiF) doped m-$TiO_2$ as the interlayers of c-$TiO_2$ and perovskite (Figure 8a). Interestingly, they found that the anions of the Li-salt influenced the electrical properties of the ETLs and the performance of PSCs. The $Li_2CO_3$-based mp-$TiO_2$ shifts the CB deeper than those of pristine m-$TiO_2$ and other Li-salt-based m-$TiO_2$ (Figure 8b). The maximum efficiency of 25.28% and certified efficiency of 24.68% was obtained by employing $Li_2CO_3$ with improved FF and $J_{sc}$.[110] Especially, Tsvetkov et al. spin-coated PbO crystal on the surface of $TiO_2$ film, PbO formed a strong interaction between $TiO_2$ and perovskite interface and transferred the surface electron interface of $TiO_2$/perovskite. The DOS study shows that the interfacial PbO with an ultra-low bandgap, which means that the introduction of metal states at the interface enhanced the transport and injection of carriers.[111] MOFs are also used as a modifier that improves performance and stability and reduces hysteresis.[112] The detailed photovoltaic parameters and stability are summarized in **Table 4**.

### 4.2. Perovskite/HTL Interface

The defects are always accumulated at the perovskite/HTM interface, where the water and oxygen molecules are easily captured by these defects, leading to the degradation of perovskite and reducing the long-term stability of the PSCs. At the same time, the interface defects usually increased the interface carrier recombination and changed the matching of interface energy level, which influenced the performance and hysteresis of the PSCs. In addition, the Li-TFSI and *t*-BP are widely used as p-type dopants within the HTMs for the state-of-the-art reported PSCs. However, the Li-TFSI is highly hydrophilic, while *t*-BP is easy to coordinate with the $PbI_2$ of the perovskite surface at the interface, which accelerates the collapse of perovskite crystal and the decreasing of PSCs performance.[10,25] Therefore, tailoring interface defects, hydrophobicity, and energy level matching of perovskite/HTM interface are particularly important for efficient, stable, and low hysteresis PSCs fabrication.

#### *4.2.1. Low-dimensional Perovskite Halide Salt*

The basic chemical formula of organic-inorganic lead halide perovskites is $ABX_3$, where A represents a cation (such as methylammonium and formamidinium), B = Pb, and X is the halogen atom.[4,7] The under-coordinated ionic defects widely exist in perovskite surface due to the non-equilibrium stoichiometric proportion; however, the secondary deposited low-dimensional perovskite halide salt (LDPHS) will fill the ionic defects and improve the surface hydrophobicity, as well as increasing the interfacial charge recombination and the stability of the PSCs. In addition, some of the LDPHS modification changes the surface energy level of perovskite, which fast the interface carrier transportation.

Jiang et al. spin-coated the PEAI on the surface of $FA_{1-x}MA_xPbI_3$ as the perovskite/HTM interfacial modifier to reduce the trap states and inhibit the recombination of photogenerated carriers. The carrier lifetime of different heating temperatures of the PEAI deposition was compared. The results show that the room temperature-based sample exhibits the longest carrier lifetime of more than 2 µs, compared to a higher temperature of 80 °C, resulting in a lower value. Based on the modification, the PCE of PSCs boosted to 23.32% with an FF of

0.784.[113] Similarly, Palei et al. introduced PETAI onto the 3D perovskite surface and increased the carrier lifetime from 0.3 μs to 1.5 μs, and the efficiency of PSCs increased from 18.8% to 20.2%. For stability, the devices based on PETAI maintained 92% of the original efficiency after aging for 500 h under continuous illumination in a high-humidity atmosphere.[114] Jeong et al. compared the influence of alkyl chains of 2D cations of LDPHS on the photoelectric properties of PSCs (CHAI and CHAMI). The TRPL measurements showed that the samples based on 2D organic cation without alkyl chain modification exhibited faster interfacial carrier injection due to the lower valence band of perovskite surface. As a result, the efficiency of PSCs increases to 23.94% with a super-high FF of 0.8425.[115] The two amino-terminals of the two-dimensional cations (XDAI) have also been introduced onto the 3D perovskite surface, which could effectively connect each layer of $PbI_4^{2-}$ crystals of perovskite. After the modification, the surface $W_F$ increased from 3.94 eV to 4.35 eV, which enhanced the extraction of photo-generated holes at perovskite/HTM interface and improved the PCE to 20.74% for $MAPbI_3$ type-based solar cells. In addition, the stability achieved was 80% (1000 h aging, 60% relative humidity) due to the higher hydrophobicity of perovskite after surface modification.[116]

Liu et al. studied the diffusion of surface modification of tert-butylcarbamidine hydrochloride (TBHCl) influence on their energy level and PV performance. The TOF-SIMS found that the TBHCl 2D material presented gradual distribution from the surface to the bottom of the perovskite and was doped with 3D perovskite film. Furthermore, the gradient doping of 3D perovskite form the gradient VB across the perovskite enhanced the carrier transport process within perovskite and the interface of perovskite/HTM. Based on the diffuse TBHCl, the PCE of PSCs was boosted to 22.54%.[117] Sung et al. studied the types of structure of 2D cations, such as long alkyl chain (OPA), aniline (PPA), and carbazole (CEPA), on the surface band structure of perovskite films and the performance of corresponding PSCs. Figure 9f shows that OPA and PPA cations are faint alter to the VB of 3D perovskite surface due to the weak surface dipole. However, CEPA increased the VB of perovskite film by 0.11 eV, making the surface energy level better matched with PTAA HTM and enhancing the steady-state fluorescence (PL) quenching of perovskite/PTAA. Finally, the PCE of PSCs based on CEPA obtained 23.6%, and the devices showed almost without change in PCE after heating at 85 °C for 1000 h, while the reference devices retained only 85% of the initial efficiency.[118] Particularly, Jang et al. proposed a solid-phase transfer method to prepare 3D/2D heterojunctions. They found that the 2D perovskite film can be developed on the surface of the 3D perovskite film under pressure and heat where the perovskite films are face-to-face stacked, enhancing the carrier lifetime of the perovskite film. Besides, the 2D perovskite film improves the hydrophobicity of 3D perovskite film. The device achieves an efficiency of 24.63% under the standard light source illumination. The corresponding PSCs retained more than 95% of the original efficiency after aging for 1000 h under 85% humidity conditions.[119] Recently, Sidhik et al. leveraged the solvent dielectric constant and Gutmann donor number to successfully grow 2D perovskite film on the 3D perovskite via the solution process, as shown in **Figure 9**a,b. They studied the composition, thickness, and bandgap of 2D layer's influence on the performance of PSCs. Characterization reveals a 3D/2D transition region of 20 nm, mainly determined by the roughness of the bottom 3D layer. At 50 nm of 2D perovskite deposition, the photovoltaic efficiency boosted to 24.5% with a high $V_{oc}$ of 1.2 V and FF of 0.84 (Figure 9c). The devices retained 99% of the initial efficiency after 2000 h operation, which is much higher than the traditional 2D cation passivation strategy (90%, 1000 h operation).[120] Xue et al. employed the $\pi$-conjugated pyrene-containing A-site cations (PREA) to tailor the electronic states of perovskite (Figure 9d). The results find that the band edges of metal-halide perovskites with a general chemical structure of $ABX_3$ are constructed mainly of the orbitals from B and X sites, and the orbitals of A-site cation are far away from the band edge. However, DFT found that the $\pi$-conjugated pyrene-containing A-site cations electronically contributed to the surface band edges and increased the VB of perovskite (Figure 9e). In addition, the ethylammonium pyrene has increased the hole mobilities, improved PCE, and the stability of PSCs.[121]

In addition, lower dimensions of organic cations have also been employed for surface defect passivation of 3D perovskite films. Cheng et al. introduced thiophene-based cations (TFCl) into the surface of 3D perovskite, and they found that the TFCl will react with $PbI_2$ and MAI to form 1D perovskite crystals, thus forming 1D/3D perovskite heterojunction. Meanwhile, the sulfur element in 1D perovskite can effectively passivate the Pb-cluster defects within perovskite film and improve the photo-generated carrier lifetime of perovskite. The efficiency of PSCs based on carbon electrodes increased to 17.42%.[122] Li et al. synthesized an organic cation based on 1,10-phenanthroline, and they found that the cation will also form the 1D/3D perovskite heterojunctions after the surface modification. The surface 1D perovskite with a high band gap (larger than 3 eV) inhibits interfacial carrier recombination of the perovskite/HTM.[123] Chen et al. synthesized organic cations based on aniline and protonated thiourea group and applied them to the surface of 3D perovskite films. The organic cations based on aniline react with 3D perovskite film and form 1D perovskite, while the cations based on protonated thiourea group will form 0D perovskite. Further study shows that the 0D/3D perovskite film has a long carrier lifetime than the 1D/3D perovskite film due to the better passivation of the interface defects, and the PCE increased to 24.49% along with the enhancement of $J_{sc}$ and FF for the 0D/3D based perovskite.[124] Similar to the low-dimensional perovskite halide salt, others materials also will react with the surface of perovskite to passivate the extra surface defects. Luo et al. introduced GABr on the surface of perovskite. On the one hand, the surface defects of the perovskite film will reduce after the surface reaction. Besides, the secondary reaction perovskite film exhibits a higher $E_F$ than the original film, which fasting the interfacial carrier transportation.[125] Similarly, they introduced $B_2Cat_2$ on perovskite film to react with the excess FAI; the reaction reduced the surface trap states and improved PSCs' stability. The devices retained 82% of the original efficiency after aging for 800 h at 30% humidity.[126] Chen et al. introduced $FAPF_6$ salt on the surface of $FA_{0.88}Cs_{0.12}PbI_3$ perovskite and formed $PF_6^-$ anion contained perovskite phase via the solid-ion exchange reaction. It is worth noting that the surface-generated phase exists at grain boundaries and forms grain boundary patches. Further study finds that the density of trap states of perovskite passivated by the grain boundary patch

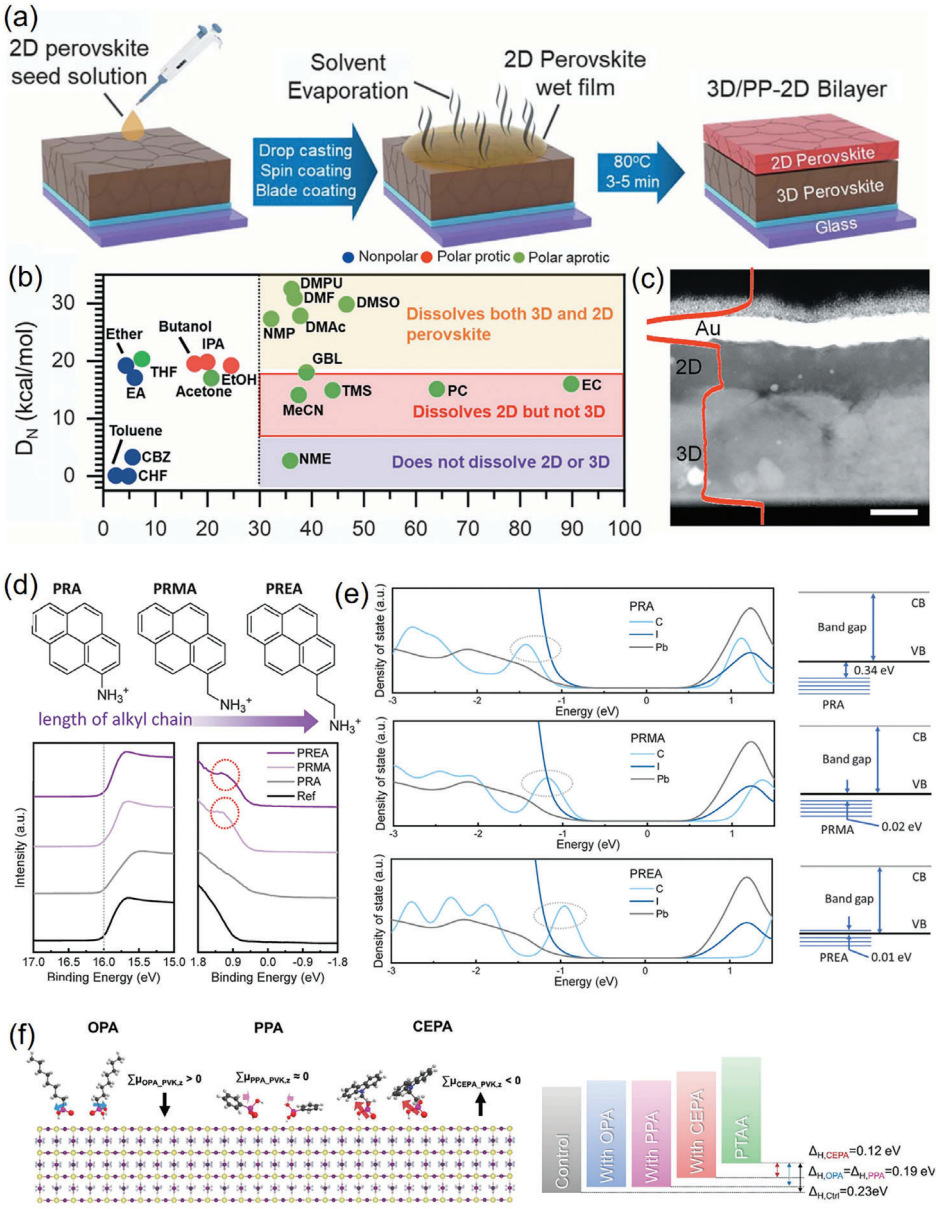


**Figure 9.** Low-dimensional perovskite halide salt employed as the interlayer of perovskite/HTM interface. a) The illustration of growth 2D perovskite film based on solution process;[120] b) the different solvents based on the dielectric constant and the Gutmann number ($D_N$) to identify the differences in solubility of the 3D and 2D perovskite powders;[120] c) the cross-sectional SEM of 3D/2D layers by the solution process; Reproduced with permission.[120] Copyright 2021, American Association for the Advancement of Science; d) the molecules' structure and the UPS of PRA, PRMA, and PREA interface materials;[121] e) the DOS of perovskite interacted with PRA, PRMA, and PREA interface materials; Reproduced with permission.[121] Copyright 2021, American Association for the Advancement of Science; f) the illustration the dipole orientation OPA, PPA, and CEPA molecules on the perovskite film, and the energy level shifting of perovskite after the interaction. Reproduced with permission.[118] Copyright 2022, Wiley-VCH.

is as low as 1.05 ×$10^{16}$ $cm^{-3}$ and improved the performance and stability of PSCs.[127] The detailed photovoltaic parameters and stability are summarized in **Table 5**.

### *4.2.2. Small Molecules and Polymers*

The small molecules and polymers are usually the surface modifier of perovskite/HTM, which the organic components will increase the hydrophobicity of perovskite film and prevent the interfacial diffusion of water and oxygen.[26] Besides, a particular functional group coordinates with perovskite, passivates the trap states and the suitable interfacial energy level, giving the carriers minimized recombination and better transportation at the interfaces. Furthermore, the interaction of molecule and perovskite sometimes transfers the electron and thus changes the energy level of the perovskite surface to match with the HTM, improving the PCE of PSCs.

**Table 5.** The Low-dimensional perovskite halide salt employed at the perovskite/HTL interface for improving the efficiency and stability of PSCs.

| Materials | HTL | Perovskite | Structure | [$J_{sc}$ / mA cm$^{-2}$] | [$V_{oc}$ / V] | FF | PCE / % | Stability | Ref. |
|---|---|---|---|---|---|---|---|---|---|
| PEAI | Spiro | $FAMAPbI_3$ | n-i-p | 25.2 | 1.179 | 0.784 | 23.32 | 80% (500 h, 85 °C) | 2019[113] |
| PETAI | Spiro | $(FAPbI_3)_{1-x}(MAPbBr_3)_x$ | n-i-p | 23.0 | 1.08 | 0.814 | 20.2 | 92% (500 h, RH 40–60%) | 2022[114] |
| CHMAI | Spiro | $FAPbI_3$ | n-i-p | 24.83 | 1.143 | 0.8425 | 23.91 | – | 2021[115] |
| XDAI | Spiro | $MAPbI_3$ | n-i-p | 23.78 | 1.134 | 0.7692 | 20.74 | 80% (1000 h, RH 60%) | 2022[116] |
| TBHCl | Spiro | $Rb_{0.02}(FA_{0.95}Cs_{0.05})_{0.98}PbI_{2.91}Br_{0.03}Cl_{0.06}$ | n-i-p | 22.60 | 1.186 | 0.841 | 22.54 | 89% (1656 h, RH 10–20%) | 2022[117] |
| CEPA | Spiro | $(FAPbI_3)_{0.95}(MAPbBr_3)_{0.05}$ | n-i-p | 24.7 | 1.18 | 0.808 | 23.6 | 95% (1000 h, MPP) | 2022[118] |
| $(BA)_2PbI_4$ | Spiro | $(FAPbI_3)_{0.95}(MAPbBr_3)_{0.05}$ | n-i-p | 24.7 | 1.185 | 0.839 | 24.59 | 94% (1056 h, 85 °C, RH 85%) | 2021[119] |
| $BA_2MA_{n-1}Pb_nI_{3n+1}$ | Spiro | $Cs_{0.05}(MA_{0.10}FA_{0.85})Pb(I_{0.90}Br_{0.10})_3$ | n-i-p | 24.34 | 1.2 | 0.84 | 24.5 | 99% (2000 h, MPP, 60 ± 5 °C, RH 70 ± 5%) | 2022[120] |
| PREA | Spiro | $(FAPbI_3)_{0.94}(MAPbBr_3)_{0.06}$ | n-i-p | 24.91 | 1.177 | 0.784 | 23 | 90% (2000 h, MPP) | 2021[121] |
| TFCl | – | $MAPbI_3$ | n-i-p | 23.36 | 1.012 | 0.737 | 17.42 | 90% (1000 h, MPP, ambient condition) | 2022[122] |
| 1,10-phenanthroline | Spiro | $CsFAMAPbI_3$ | n-i-p | 25.4 | 1.12 | 0.82 | 23.3 | 80% (800 h, RH 50%) | 2022[123] |
| 0D | Spiro | $Cs(FAPbI_3)_x(MAPbBr_3)_{1-x}$ | n-i-p | 25.51 | 1.163 | 0.8254 | 24.49 | 90% (800 h, MPP) | 2022[124] |
| GABr | PTAA | $(FA_{0.95}PbI_{2.95})_{0.85}(MAPbBr_3)_{0.15}$ | p-i-n | 22.50 | 1.21 | 0.790 | 21.51 | – | 2018[125] |
| $B_2Cat_2$ | Spiro | $FA_{0.81}MA_{0.10}Cs_{0.04}PbI_{2.55}Br_{0.40}$ | n-i-p | 22.88 | 1.183 | 0.78 | 21.11 | 82% (800 h, RH 30%) | 2018[126] |
| $FAPF_6$ | Spiro | $FA_{0.88}Cs_{0.12}PbI_3$ | n-i-p | 23.11 | 1.045 | 0.80 | 19.25 | 80% (528 h, 50–70%) | 2018[127] |

Krishna et al. introduced 2, 5-thiophene dicarboxylic acid at the interface of perovskite/HTM. The C=O group of the molecule could coordinate with Pb-cluster atoms on the surface of perovskite, reducing the accumulation of surface charges (Figure 10f). By employing the interface modification, the PCE of corresponding n-i-p PSCs reached 23% PCE. Interestingly, the migration of Au element to perovskite is also inhibited due to the molecular filling of grain boundaries, so that the PSCs storage under $N_2$ condition for 1400 h, the PCE still retained more than 90% of the initial efficiency.[28] Furthermore, Zhang et al. introduced ferrocene to $(FAPbI_3)_{0.95}(MAPbBr_3)_{0.05}$ surface (**Figure 10**a). The ferrocene is a gradient distribution across the perovskite via the molecule diffusion, thus making the upward band bending of perovskite toward HTM side, enhancing the $E_{bi}$ of bulk perovskite and reducing the recombination at perovskite/HTM interface (Figure 10b). Finally, the PCE of PSCs with ferrocene increased to 23.45% with a higher FF of 0.805. Beyond the increased hydrophobicity of PSCs, it is worth noting that the introduction of ferrocene effectively reduced the diffusion of Spiro-OMeTAD, further improving the stability of PSCs.[128] Abdi-Jalebi et al. coated the tetracene on the perovskite film, and the PSCs obtained a PCE of 21.6%. They find that the improvement of PCE is attributed to the HOMO level of tetrabene-benzene (−5.28 eV) between the perovskite film (−5.43 eV) and Spiro-OMeTAD (−5.22 eV), which forms an energy level ladder and reduces the interface barrier of carrier transportation.[129] Sutanto et al. synthesized a small molecule based on phosphine oxide (THPPO) to passivate the perovskite surface. The passivating mainly originates from the coordination of Pb–O bond, which allows the transfer of the lone pair electron. Based on the passivation, the PCE of PSCs improved to 20.70%.[130] Similarly, Su et al. proposed that the crown ether molecules complexed with cations in perovskite, and passivate the film surface defect states via the Pb–O bond. Moreover, the crown ether molecules will also interact with the $MA^+$ and $FA^+$ within perovskite films through the difference in electrostatic potential, which further reduces the surface trap states and minimizes the $V_{oc}$ loss. The corresponding PSCs obtained PCE of 23.7% with better FF (0.795) and *J*sc (25.80 mA cm$^{-2}$) under standard simulated sunlight illumination. In addition, the device still maintains more than 80% of the initial efficiency after outputting 300 h.[131]

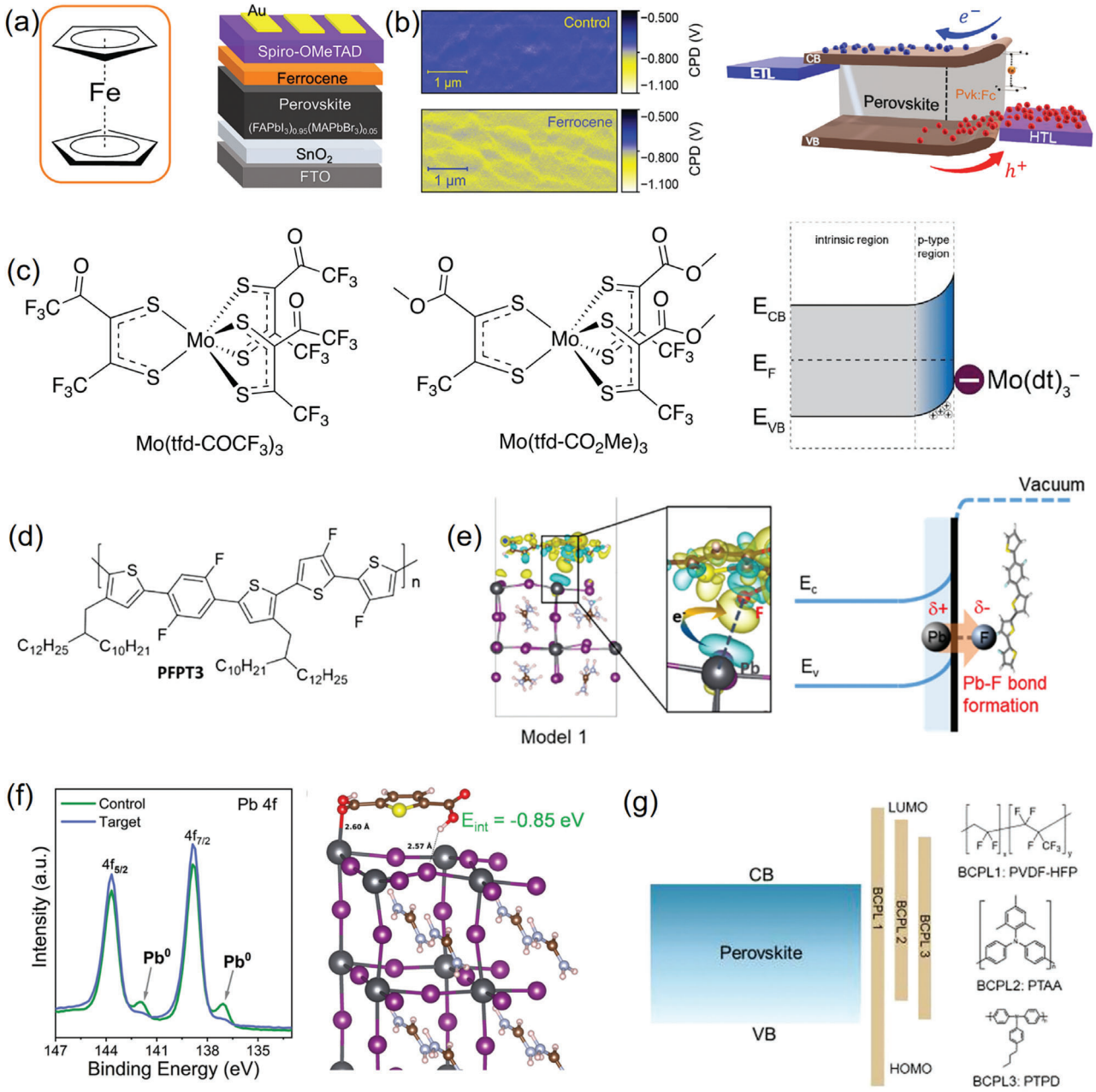


**Figure 10.** The small molecules and polymers employed as the interlayers of perovskite/HTM interface. a) The illustration of the ferrocene as the interface modification of perovskite/HTM;[128] b) the KPFM of the perovskite surface with or without the ferrocene and the illustration of band blending of perovskite surface; Reproduced with permission.[128] Copyright 2022, Wiley-VCH; c) the molecule structure of p-dopants and the surface p-dopant induced perovskite band blending; Reproduced with permission.[30] Copyright 2019, The Royal Society of Chemistry; d) the molecule structure of PFPT3;[135] e) the charge density difference of PFPT3 interacted with perovskite and the corresponding band blending by the PFPT3; Reproduced with permission.[135] Copyright 2021, American Chemical Society; f) the XPS of 2, 5-thiophene dicarboxylic acid interacted with perovskite as well as the optimized structure of 2, 5-thiophene dicarboxylic acid interacted with perovskite surface; Reproduced with permission.[28] Copyright 2021, The Royal Society of Chemistry; g) the interfacial energy levels of PVDF-HFP, PTAA, and PTPD, as well as the corresponding molecule structure. Reproduced with permission.[136] Copyright 2019, Wiley-VCH.

The electronic interfacial materials have also been employed in the perovskite/HTM interface. Chen et al. synthesized a primary amine (CZ-Py) based electron donor and deposited it onto the surface of perovskite. Because CZ-Py with a higher HOMO level (−5.32 eV) than perovskite film (−5.72 eV) leads to the increasing VB energy level of perovskite, when it mixed with perovskite surface, thereby reducing the interface barrier between perovskite and HTM. Finally, the steady-state efficiency of 23.1% was obtained with this strategy.[132] Tian et al. also synthesized electron donors based on triphenylamine core which introduced methoxy

**Table 6.** The small molecules and polymers employed at the perovskite/HTL interface for improving the efficiency and stability of PSCs.

| Materials | HTL | Perovskite | Structure | [$J_{sc}$ / mA cm$^{-2}$] | [$V_{oc}$ / V] | FF | PCE / % | Stability | Ref. |
|---|---|---|---|---|---|---|---|---|---|
| 2,5-thiophenedicarboxylic acid | Spiro | $(FAPbI_3)_{1-x}(MAPbBr_3)_x$ | n-i-p | 25.27 | 1.172 | 0.791 | 23.4 | 90% (1400 h, $N_2$) | 2021[28] |
| Ferrocene | Spiro | $(FAPbI_3)_{0.95}(MAPbBr_3)_{0.05}$ | n-i-p | 25.26 | 1.153 | 0.8050 | 23.45 | 70% (1250 h, 60 °C, RH 50%) | 2022[128] |
| Tetracene | Spiro | $Cs_{0.06}FA_{0.79}MA_{0.15}Pb(I_{0.85}Br_{0.15})_3$ | n-i-p | 23.4 | 1.18 | 0.78 | 21.6 | 90% (550 h, MPP) | 2019[129] |
| THPPO | Spiro | $[(FAPbI_3)_{0.87}(MAPbBr_3)_{0.13}]_{0.92}(CsPbI_3)_{0.08}$ | n-i-p | 24.08 | 1.108 | 0.776 | 20.70 | – | 2021[130] |
| Crown-Ether | Spiro | $FA_{0.97}MA_{0.03}PbI_{2.97}Br_{0.03}$ | n-i-p | 25.80 | 1.154 | 0.795 | 23.70 | 80% (300 h, MPP, $N_2$) | 2020[131] |
| CZ-Py | Spiro | $FA_{0.9}MA_{0.1}PbI_3$ | n-i-p | 25.2 | 1.15 | 0.812 | 23.5 | 95% (1000 h, RH 50–60%) | 2021[132] |
| TM6 | Spiro | $Cs_{0.05}(MA_{0.17}FA_{0.83})_{0.95}Pb(I_{0.83}Br_{0.17})_3$ | n-i-p | 23.10 | 1.111 | 0.7862 | 20.18 | 97% (1056 h, RH 30–40%) | 2022[133] |
| TPA-PEABr | Spiro | – | n-i-p | 23.13 | 1.09 | 0.72 | 18.15 | 80% (30 days, RH 40–50%) | 2020[134] |
| $Mo(tfd\text{-}COCF_3)_3$ | Spiro | $FA_{0.85}MA_{0.15}Pb(I_{0.85}Br_{0.15})_3$ | n-i-p | 22.5 | 1.16 | 0.79 | 20.6 | 45% (800 h, 85 °C, RH 45%) | 2019[30] |
| PFPT3 | Spiro | $FAPbI_3$ | n-i-p | 24.34 | 1.13 | 0.80 | 22.00 | – | 2021[135] |
| PTPD | Spiro | $Cs_{0.05}MA_{0.05}FA_{0.9}PbI_{2.85}Br_{0.15}$ | n-i-p | 23.1 | 1.137 | 0.832 | 21.9 | – | 2019[136] |
| PTzNDI-2FT | Spiro | $Cs_{0.05}MA_{0.1}FA_{0.85}Pb(I_{0.9}Br_{0.1})_3$ | n-i-p | 25.2 | 1.2 | 0.77 | 23.2 | Near 100% (3000 h, RH 10%) | 2021[137] |

(TM5) and methylthiol (TM6) at the side chain of molecules and introduced them as the interlayer of MAPbI3/Spiro-OMeTAD to passivate the trap states. It is found that TM5 interacts with Pb atoms of perovskite through O atoms, while TM6 via the S atoms. The compared trap states find that the passivation ability of TM6 is higher than TM5, which may originate from the different donor abilities of the coordination atoms.[133] The devices based on TM6 achieved a PCE of 20.15%. Zhao et al. introduced the ammonium bromide group (TPA-EABr) and aniline bromide group (TPA-PEABr) based on the triphenylamine structure. They employed them as the interface modifiers of perovskite/HTM and compared the corresponding PSCs performance difference under the weak structural changes in the passivation materials. The TPA-PEABr film exhibits a higher HOMO level than TPA-EABr, which is helpful in improving the heterojunction contact between perovskite and Spiro-OMeTAD. The PSCs based on TPA-PEABr exhibit a higher PCE.[134] Noel et al. spin-coated $Mo(tfd\text{-}COCF_3)_3$ electron acceptor material on the surface of perovskite. Owing to its strong electron acceptor properties, $Mo(tfd\text{-}COCF_3)_3$ effectively transferred the electrons of the perovskite surface, which changed the electron concentration of perovskite film to achieve p-type doping on the surface and led to surface band blending of perovskite after the equilibrium of $E_F$ (Figure 10c). As the improved injection of carriers at the perovskite/HTM interface, the PCE of PSCs without *t*-BP dopant obtained 20.6%.[31]

Polymers are also employed for the interfacial materials of perovskite/HTM due to the higher hydrophobicity. Lyu et al. prepared a fluorinated conjugated polymer (PFPT3) and employed it as an interfacial layer of perovskite/HTM (Figure 10d). Interaction of perovskite and PFPT3 via Pb–F bonding induces surface dipole toward perovskite, which resulted in band bending of perovskite and is favorable for the hole extraction at the interface (Figure 10e). In addition, the PFPT3 interfacial layer strongly increases adhesion between perovskite and Spiro-MeOTAD, which suppresses the delamination of the HTM from perovskite layer. As a result, the PCE of PSCs boosted to 22.00%.[135] Tan et al. compared the structure difference of the polymers (PVDF, PTAA, PTPD) on the passivation of perovskite (Figure 10g). As a result, the PTPD-based interfacial materials exhibited the best passivation ability than others and obtained a PCE of 21.9% with a high FF of 0.83.[136] Recently, Li et al. synthesized naphthalimide-based hydrophobic fluorinated copolymer molecules (PTzNDI-2FT) and applied them as the interface of perovskite/Spiro-OMeTAD. In addition to improving the hydrophobicity of the perovskite surface, oxygen and fluorine atoms within the molecules effectively interact with the Pb atoms of perovskite film, thus inhibiting the trap state and increasing carrier lifetime. Based on the interface modification, the efficiency of PSCs boosted to 23.2%, and the PCE of PSCs was almost without alteration after the device aged at 10% relative humidity condition for 3000 h.[137] Others, such as polyTPD,[136] PBDB-T,[138] PTQ10,[139] also have been used for the interface layer of perovskite/HTM, which improved both efficiency and stability of PSCs. The detailed photovoltaic parameters and stability are summarized in **Table 6**.

#### *4.2.3. Quantum Dots and Carbon-based Materials*

Quantum dots (QDs) and carbon-based materials are also widely used for interface engineering via turning the surface energy level and offer unique chemical interactions. M. Bakr et al. spin-coated inorganic perovskite quantum dots onto the surface of

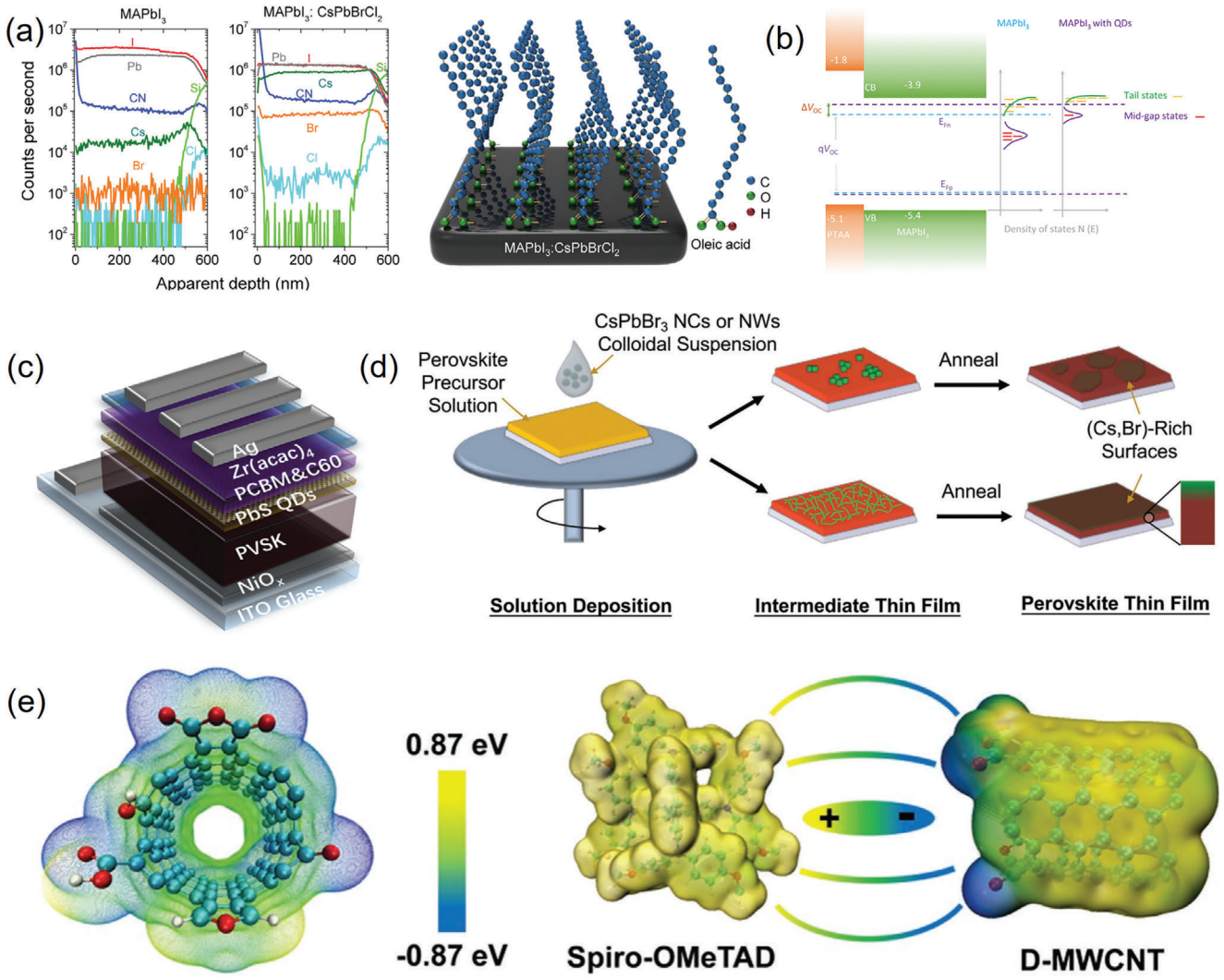


**Figure 11.** The quantum dots and carbon-based materials for the interface modification of perovskite/HTM. a) The TOF-SIMS of $CsPbBrCl_2$ QDs doping the perovskite film and the illustration of the surface anchored ligand after the QDs doping;[140] b) the illustration of energy level and the trap states of PSCs with or without the $CsPbBrCl_2$ QDs doping; Reproduced with permission.[140] copyright 2019, Elsevier; c) the illustration of devices structure by employing the PbS QDs interface modification; Reproduced with permission.[141] Copyright 2020, Wiley-VCH; d) the illustration of $CsPbBr_3$ NWs and NCs modified the perovskite surface; Reproduced with permission.[143] Copyright 2019, Wiley-VCH; e) the molecule structure of D-MWCNT and its electronic properties; Reproduced with permission.[146] Copyright 2022, Wiley-VCH.

the perovskite film, as shown in **Figure 11**a. Inorganic perovskite quantum dots evenly doped the whole perovskite film, while the organic components will anchor to the surface of the perovskite film. The results show that the inorganic perovskite quantum dots will reduce the trap state of the perovskite (Figure 11b). Besides, the self-assembled organic layer will effectively block the water on the surface of the perovskite, thus improving the device's efficiency and stability at the same time. Finally, the corresponding PSCs achieve an efficiency of 21.5%. Owing to the defect's passivation and surface hydrophobic organic molecules on perovskite, the stability of PSCs has been greatly improved, and it maintained 80% of the initial efficiency under the condition of 500 h of aging.[140] Bonaccorso et al. anchor $MoS_2$ QDS to graphene sheets via siloxane ($MoS_2$ QDs:f-RGO), and employ it as the interface layer between $MAPbI_3$ and Spiro-OMeTAD. It is found that $MoS_2$ QDs exhibit higher CB and lower VB than perovskite film, thus effectively reducing the recombination of carriers at the interface. At the same time, graphene improved the conductivity of the interface, thereby enhancing the interface carrier transporting and improving the photovoltaic performance of PSCs. The stability study showed that the composite interface modifier could increase the stability from 75.4% to 91.2% (after 1000 h of aging).[30] Ma et al. introduced lead sulfide QDs on the surface of perovskite (Figure 11c). The QDs interacted with the perovskite grain boundaries and inhibited the ion migration of perovskite. The reduction of the dangling bonds of $Pb^{2+}$ by the S atoms of QDs leads to highly improved PCE of devices due to the reduced non-radiative recombination. As a result, the $V_{oc}$ is significantly improved to higher values of 1.13 V for $MAPbI_3$-based PSCs. In addition, the stability also has been improved.[142] Akin

**Table 7.** The Quantum dots and carbon-based materials employed at the perovskite/HTL interface for improving the efficiency and stability of PSCs.

| Materials | HTL | Perovskite | Structure | [$J_{sc}$ / mA cm$^{-2}$] | [$V_{oc}$ / V] | FF | PCE / % | Stability | Ref. |
|---|---|---|---|---|---|---|---|---|---|
| $CsPbBrCl_2$ QDs | PTAA | $MAPbI_3$ | p-i-n | 23.4 | 1.15 | 0.8 | 21.5 | 80% (500 h, MPP) | 2019[140] |
| $MoS_2$ QDs:f-RGO | Spiro | $MAPbI_3$ | n-i-p | 22.81 | 1.11 | 0.7975 | 20.12 | 91.2% (1000 h) | 2018[29] |
| PbS QDs | NiOx | $MAPbI_3$ | p-i-n | 22.81 | 1.13 | 0.80 | 20.64 | – | 2020[141] |
| $CsPbBr_{1.85}I_{1.15}$ PQDs | Spiro | $Cs_{0.05}(FA_{0.85}MA_{0.15})_{0.95}Pb(I_{0.85}Br_{0.15})_3$ | n-i-p | 23.42 | 1.14 | 0.79 | 21.14 | 91% (30 days, RH 40–50%) | 2019[142] |
| $CsPbBr_3$ NWs | Spiro | $MA_{0.3}FA_{0.7}PbI_3$ | n-i-p | 24.1 | 1.12 | 0.791 | 21.37 | 96% (200 h, MPP, 40 °C) | 2019[143] |
| Cl-GO | PTAA | $FA_xMA_{1-x}PbI_3$ | n-i-p | 23.82 | 1.12 | 0.79 | 21.08 | 90% (1000 h, MPP, 60 °C) | 2019[144] |
| CNT@G | Spiro | $MAPbI_3$ | n-i-p | 23.52 | 1.08 | 0.77 | 19.56 | 80% (500 h, RH 30–50%) | 2018[145] |
| D-MWCNT | Spiro | $FA_xMA_{1-x}PbI_3$ | n-i-p | 25.97 | 1.08 | 0.787 | 22.07 | 95% (800 h, MPP) | 2022[146] |

et al. employed the $CsPbBr_{1.85}I_{1.15}$ QDs on perovskite layer to resist moisture-induced degradation. By employing the QDs, the PCE of PSCs boosted to 21.14%, and it could retain 94% of their initial performance after 400 h of illumination.[142] Zhang et al. employed $CsPbBr_3$ perovskite nanowires to modify the surface electronic states of perovskite, forming graded heterojunctions at the perovskite/HTL interface of PSCs (Figure 11d). The resulting PSCs show a high PCE of up to 21.4% and high operational stability.[143] Wang et al. reported chlorinated graphene oxide (Cl-GO) as the interface layer to stabilize the perovskite. The Cl-GO interacted with the Pb-rich perovskite film through the strong Pb–Cl and Pb–O chemical bonds. The interaction enhanced the extraction of photo-generated charge carriers and avoided the loss of weak components from perovskites. The target PSCs retained 90% of their initial PCE of 21% under continuous outputting at 60°C for 1000 h.[144] Li et al. composited the graphene with a carbon nanotube (CNT@G) and employed it to dope Spiro-OMeTAD for the PSCs. The CNT@G doped Spiro-OMeTAD exhibits efficient carrier extraction, faster charge transport, and restrained carrier recombination, which improved the PCE and stability of PSCs.[145] Recently, Wang et al. demonstrated the multi-walled CNT (D-MWCNT) would tune the charge transfer kinetics at the perovskite/HTM interface. Benefiting from the electrostatic dipole moment interaction between the oxygen-containing groups of D-MWCNT and Spiro-OMeTAD, the energy level of HTM has been turned, allowing faster charge transfer by the electron redistribution and 1D hyper-channels (Figure 11e), the efficiency of PSCs boosting to 22.07% (FF = 0.787, $J_{sc}$ = 25.97 mA cm$^{-2}$, $V_{oc}$ = 1.08) and exhibits excellent operational stability.[146] The detailed photovoltaic parameters and stability are summarized in **Table 7**.

### 4.3. Electrode/CTLs Interface

The electrode layer plays the role of photo-generated carrier collection, which also affects the photoelectric performance of PSCs. The energy level matching between the FTO/ITO electrode and the ETL, as well as the Ohmic contact between the HTM and metal electrode (Au or Ag), are significant for collecting photogenerated charge and improving stability. Ma et al. prepared a MgO metal oxide layer at the FTO/$SnO_2$ interface. Owing to the anchoring effect, the metal oxide formed a dipole moment on the FTO surface and improved its work function. In addition, the introduction of MgO further inhibited the charge recombination at the ITO/$SnO_2$ interface, thus improving the photovoltaic performance of PSCs and the efficiency achieving 18.23%.[147] Lee et al. combined alkali metal complex (LiQ) with polyethylene imine (PEIE) and employed it as the interlayer to modify ITO/PCBM interface. The study found that the composite interface material formed a dipole moment on the surface of ITO, increasing the work function of ITO from −4.68 eV to −4.15 eV, which improved the interfacial energy level matching between ITO and PCBM. Finally, the PCE of PSCs based on organic PCBM ETL achieved 15.21%.[148] Recently, Li et al. proposed a chemical anticorrosion strategy to fabricate stable PSCs *by* introducing an organic corrosion inhibitor of benzotriazole (BTA) before Cu electrode deposition. BTA molecule will chemically coordinate with the Cu electrode and form an insoluble polymeric film of [BTA-Cu], suppressing the electrochemical corrosion and reaction between perovskite and the Cu electrode. PSCs with BTA/Cu exhibit good operational stability, 88.6 ± 2.6% of initial efficiency retained after continuous outputting for 1000 h.[149]

Xie et al. employed fullerene derivative PCBDAN mixed into PCBM as an ETL and spun onto the surface of ITO electrode. Owing to the strong polarity of PCBDAN, the PCBDAN:PCBM vertical phase separation during the spin-coating resulted in PCBDAN enrichment on the surface of ITO, while PCBM concentrated on the surface of the film (Figure 12b). The aggregated PCBDAN at the bottom turned the work function of ITO to −4.1 eV via the surface dipole, which matched well with the LUMO level of PCBM. Finally, 18.1% of efficiency was obtained based on the phase separation strategy, and the devices exhibit high UV light stability due to avoiding metal oxide ETL.[150] Lee et al. doped PCBM with PEI and prepared it on ITO electrode by scraping and spin-coating methods (**Figure 12**a). The N atom within PEI will interact with the hydroxyl group of ITO surface, which leads to the PEI enrichment on the ITO surface during

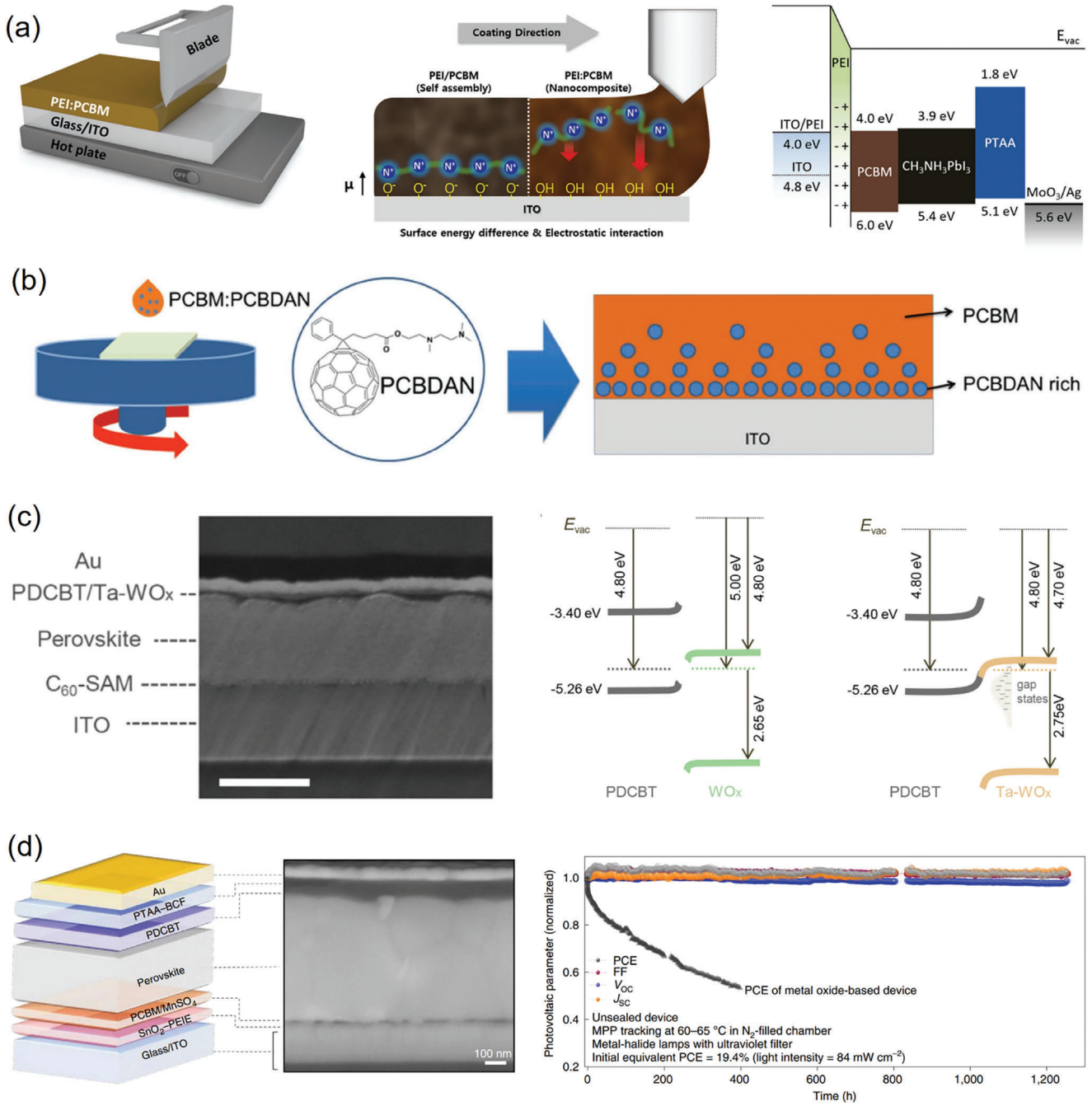


**Figure 12.** The modification of CTLs/electrode interface. a) The illustration of phase-separated PCBM:PEI by the blade coating and the corresponding energy level of PSCs; Reproduced with permission.[151] Copyright 2017, Wiley-VCH; b) the illustration of phase-separated PCBM:PCBDAN during the spin-coating; Reproduced with permission.[150] Copyright 2017, Wiley-VCH; c) The SEM of Ta-$WO_3$ as the interlayer of PDCBT and Au electrode, as well as the interfacial energy level shifting with the $WO_3$ and Ta-$WO_3$ interlayer; Reproduced with permission.[153] Copyright 2017, American Association for the Advancement of Science; d) the illustration of PTAA-BCF interlayer between PDCBT and Au electrode, and the corresponding cross-sectional SEM of PSC, as well as the stability of PSCs based on the interface modification; Reproduced with permission.[154] Copyright 2022, Springer Nature.

the printing and spin-coating process. The surface-enriched PEI formed interfacial dipoles, which regulated the surface work function of ITO to match the energy level of PCBM better. The final PCBM-based device achieves 17.4% efficiency. Furthermore, the intrinsic stability of PSCs is improved by reducing the accumulation of charge carriers at ITO interface.[151] Similarly, our previous work also reported a phase separation doping method to build a graded energy level between the ITO and perovskite via the PCBM:CsF mixture. Experimental and theoretical results prove that the inhomogeneous distribution of CsF within the bulk or surface of PCBM would not only form metal–oxygen (M–O) dipole on MOE but also create a graded energy bridge

**Table 8.** The modification of CTLs/electrode interface for improving the efficiency and stability of PSCs.

| Materials | Electrode | Perovskite | Structure | [$J_{sc}$ / mA cm$^{-2}$] | [$V_{oc}$ / V] | FF | PCE / % | Stability | Ref. |
|---|---|---|---|---|---|---|---|---|---|
| MgO | FTO | $MAPbI_3$ | n-i-p | 22.70 | 1.10 | 0.73 | 18.23 | – | 2017[147] |
| PEIE-LiQ | ITO | $MAPbI_3$ | n-i-p | 19.03 | 1.06 | 0.76 | 15.21 | – | 2017[148] |
| BTA | Cu | $(FAPbI_3)_x(MAPbBr_3)_{1-x}$ | p-i-n | 24.22 | 1.04 | 0.795 | 19.94 | 88.6 ± 2.6% (1000 h, MPP) | 2020[149] |
| PCBDAN | ITO | $MAPbI_3$ | n-i-p | 21.70 | 1.08 | 0.773 | 18.1 | 85% (228 h, UV light, RH 45%) | 2017[150] |
| PEI | ITO | $MAPbI_3$ | n-i-p | 19.63 | 1.131 | 0.783 | 17.40 | 90% (60 h, $N_2$) | 2017[151] |
| CsF | ITO | $Cs(FAPbI_3)_x(MAPbBr_3)_{1-x}$ | n-i-p | 22.64 | 1.148 | 0.8053 | 20.93 | 89% (60 days, ambient condition) | 2020[24] |
| Ta-$WO_3$ | Au | $FA_{0.83}MA_{0.17}Pb_{1.1}Br_{0.50}I_{2.80}$ | n-i-p | 22.7 | 1.17 | 0.80 | 21.2 | Over 100% (1000 h, MPP) | 2017[153] |
| PTAA-BCF | Au | $MA_{0.10}Cs_{0.05}FA_{0.85}Pb(I_{0.95}Br_{0.05})_3$ | n-i-p | 24.2 | 1.11 | 0.778 | 20.9 | 99% (1450 h, 65 °C, $N_2$) | 2022[154] |

to alleviate the disadvantage of band offset, which significantly avoids the carrier accumulation and recombination at defective interfaces.[24]

Ohmic contacts between HTM and metal electrodes (Au or Ag) have also been extensively studied. The polymerized PDCBT HTM has high stability and mobility but has inferior Ohmic contact with Au electrode. Sanehira et al. deposited $MoO_3$ layer at PDCBT/Au interface and improved the efficiency of PSCs; however, the results are dissatisfactory.[152] Aiming at the Ohmic contact problem at the interface of PDCBT/Au, Hou et al. comparatively studied the effects of $WO_3$ and Ta-doped $WO_3$ interlayers on the performance of PSCs (Figure 12c). UPS measurement finds that Ta-doped $WO_3$ could effectively match the surface energy level of PDCBT, improve its HOMO level, and then regulate its Ohmic contact with Au electrode. Finally, employing the dopant-free PDCBT, the PCE of PSCs boosted to 21.2%. The metal oxide layer will effectively interact with Au electrode and inhibit its ion migration which further improves the intrinsic stability of the device. Finally, the PCE of the device continuously outputting for 1000 h under $N_2$ conditions almost without decreasing. The result is also much higher than the device based on $MoO_3$ modification.[153] Although the Ohmic contact problem exists with the PDCBT/Au interface, the PTAA polymer HTM is well in contact with the Au electrode. Furthermore, Zhao et al. employed BCF-doped PTAA as the interface modification layer to ameliorate the Ohmic contact of the PDCBT/Au electrode. Besides improving the PCE of devices, the PSCs also exhibit ultra-high thermal stability, which retains 99% of the initial efficiency after heating at 65 °C for 1400 h.[154] The detailed photovoltaic parameters and stability are summarized in **Table 8**.

## 5. Insulating Layer

Most of the work aims to turn the energy level and reduce trap states by interface engineering. On the contrary, the insulating materials with a high band gap are also employed to reduce the interface recombination between the CB(VB) of CTLs and the VB(CB) of perovskite (Figure 1d).

Si et al. optimized the thickness of the insulating layer by quantum tunnel model based on effective-mass approximation (EMA) theory. The performance of the PSCs was modulated by tuning the thickness of $Al_2O_3$ middle layer. The optimal insulating layer can suppress the carrier recombination and improve the PCE of PSCs, resulting in the highest efficiency at the thickness of 4 Å.[155] Mathiazhagan et al. also employed the $Al_2O_3$ insulating layer to reduce the interfacial recombination and result in improved performance of PSCs.[156] Wang et al. inserted a polystyrene (PS) tunnel layer between perovskite and ETL interface, which reduced the interface charge recombination, making the stabilized efficiency of PSCs 20.3%. The tunnel layer also serves as the encapsulation material to prevent perovskite film from moisture, which has improved the stability of PSCs.[157] Zheng et al. introduced fluorine-containing insulating polymers, poly(perfluorobutenylvinylether) (Cytop), as the tunnel layer for planar PSCs. The Cytop layer not only fills the pinholes of the perovskite surface to decrease the trap concentration but also restricts charge recombination via the higher band gap as compared to perovskite.[158] Li et al. employed poly(4-vinylpyridine) (PVP) insulating layer at the interface of $NiMgO_x$ HTL and perovskite absorbing layer, the interfacial recombination of carriers has been effectively suppressed, and the $V_{oc}$ improved to an impressive value of 1.18 V.[159] Seok et al. introduced the ultrathin polymer polymethyl methacrylate (PMMA) between the perovskite layer and the copper phthalocyanine (CuPC) HTM, which can effectively inhibit carrier recombination at this interface, thus improving the $V_{oc}$ of PSCs. In addition, the device retains 80% of its initial efficiency when stored at 85 °C heating for 800 h.[20] Ochoa-Martinez et al. further analyzed the effect of PMMA on the perovskite film. Spatial and time-resolved photoluminescence and AFM analyses of samples with diverse morphologies demonstrate the deposition of PMMA in topographic depressions of the perovskite layer, such as grain and domain boundaries. The improvement of PCE by PMMA modification may attribute to the grain boundaries passivation.[160] In addition, Peng et al. employed PMMA at $TiO_2$/Perovskite interface, which increased the $V_{oc}$ of PSCs to 1.18 V.[161] They further employed the PMMA:PCBM mixture and the PMMA to double passivate the perovskite layer (PMMA:PCBM/perovskite/PMMA), improved the $V_{oc}$ to 1.22 V with a PCE of 20.4%.[162] Kim et al. compared the effect of relatively hydrophilic polyvinyl oxide (PEO) and relatively hydrophobic polystyrene (PS) interface

**Table 9.** The Insulating layer employed for the interface modification of PSCs.

| Materials | Interface | Perovskite | Structure | $[J_{sc}$ / mA cm$^{-2}]$ | $[V_{oc}$ / V] | FF | PCE / % | Stability | Ref. |
|---|---|---|---|---|---|---|---|---|---|
| $Al_2O_3$ | ETL/perovskite | $MAPbI_3$ | n-i-p | 18.90 | 1.01 | 0.62 | 15.55 | – | 2016[155] |
| PS | ETL/perovskite | $MAPbI_3$ | p-i-n | 22.90 | 1.10 | 0.806 | 20.3 | – | 2016[157] |
| Cytop | ETL/perovskite | $MAPbI_3$ | p-i-n | 20.4 | 0.91 | 0.78 | 14.5 | – | 2017[158] |
| PVP | HTL/perovskite | $Cs(FAPbI_3)_x(MAPbBr_3)_{1-x}$ | p-i-n | 21.5 | 1.148 | 0.78 | 19.3 | – | 2018[159] |
| PMMA | HTL/perovskite | $(FAPbI_3)_{0.95}(MAPbBr_3)_{0.05}$ | n-i-p | 24.87 | 1.08 | 0.7929 | 21.25 | 80% (800 h, 85 °C, RH 25%) | 2021[160] |
| PMMA | ETL/peorvskite | $Cs_{0.07}Rb_{0.03}FA_{0.765}MA_{0.135}PbI_{2.55}Br_{0.45}$ | n-i-p | 23.2 | 1.16 | 0.76 | 20.4 | – | 2018[162] |
| PEO | HTL/perovskite | $MAPbI_3$ | n-i-p | 19.87 | 1.098 | 0.75 | 16.46 | 50% (15 days, RH 88%) | 2018[163] |

modification on the stability of perovskite films. It is found that the perovskite film based on relatively hydrophilic PEO can adsorb water molecules on the surface of the polymer, thus protecting the perovskite film and making the devices based on PEO exhibit better stability.[163] The detailed photovoltaic parameters and stability are summarized in **Table 9**.

## 6. Interface Engineering for the Flexible PSCs

The flexible PSCs is one of most important direction for the PSCs application, which is popular for flexible wearable electronic devices and aerospace ascribes to the property of bending and weeny weight. Interface engineering also has been widely employed to improve the photovoltaic properties and the blending stability of flexible PSCs.[164]

Inorganic interfacial materials have been employed for highly efficient flexible PSCs. Zhang et al. introduced an inorganic CsBr buffer layer between $NiO_x$ HTL and perovskite layer to relieve the lattice mismatch-induced interface stress. The results show that the addition of the CsBr buffer layer optimized the interface between the perovskite absorber and the $NiO_x$ HTL, reduces interface trap states, and promoted the hole extraction injection. Finally, the PCE of optimal PSCs reaches up to 19.2%. Meanwhile, The PCE of control device declines to 65% of initial efficiency after 900 h while the device modified by CsBr still maintains 82% of the initial efficiency under the same condition (RH = 30%).[165] Ren et al. exploited a cross-linking agent of aluminum acetylacetonate ($Al(acac)_3$) as an interface layer between ETL and perovskite layer, making the energy levels of ETL well-matched with perovskite, meanwhile improving the grain size and crystallinity of the perovskite. Finally, a high PCE of 20.87% is achieved for the flexible PSCs. The device retains ≈80% of its initial performance after 1000 h aging without encapsulation (RH>50%). In addition, the devices blending 1500 cycles still retained over 91% of the initial PCE.[166]

The organic interface materials, such as the fullerene derivative, small molecule, and polymer also have been widely employed for flexible PSCs to enhance the performance and the blending stability. Kim et al. employed PCBM as the interface layer to enhance electron extraction of amorphous $TiO_2$. The amorphous $TiO_2$ plays the role of efficient electron selective contact with perovskite layer, while PCBM will help electrons to rapidly extract from perovskite. As a result, the PCE of flexible PSCs achieved 17.70% with a $V_{oc}$ of 1.09 V. In addition, the PCBM-based PSCs also exhibited better stability under 1 sun illumination.[167] Zhong et al. further developed the fullerene derivative with a carboxylic group (CPTA) to modify the low-temperature (140 °C) processed $SnO_2$ layer as the ETL of PSCs on a flexible PEN (polyethylene naphthalate) substrate. The beneficial effects of interface modification on increasing the carrier selectivity to electrons were elucidated and resulted in a PCE of 18.36% for the solar cells. The flexible PSCs retained 75% of their initial efficiency after 500 cycles of bending with a curvature radius of 5 mm.[168] Xiong et al. developed a simple surface post-treatment with *N*-benzyloxycarbonyl-d-valine (NBDV) to overcome interface contact problem between perovskite and PCBM. The study finds that NBDV surface post-treatment results in the bulk restructure of the entire perovskite film and improves the film-forming property of PCBM. Moreover, The strategy also improved the grain sizes, crystallinity, trap states, cathode interfaces, as well as the built-in field of devices, which result in performance and stability enhancement. A relatively higher PCE of 21.80% with highly FF of 82.74% is reached for flexible PSCs by the modification. Meanwhile, the PCE of the NBDV-based PSCs retain ≈77% and 84% of the initial value after storage for 768 h in air and 8376 h in $N_2$ conditions, respectively. However, the control devices only maintain ≈53% and 38% of their initial PCE values under the same aging conditions.[169] Meng et al. designed a thermally activated delayed fluorescence polymer P1 to modify the $FAPbI_3$ film. The spectral overlap between the photoluminescence of P1 and absorption of the above-bandgap quantum wells of $FAPbI_3$, which reduces the non-radiative recombination losses in PSCs. Moreover, P1 is found to introduce compressive stress into $FAPbI_3$, which relieves the tensile stress in perovskite. Consequently, the flexible PSCs deliver a high PCE of 21.40%. In addition, the flexible PSCs bending over 1000 cycles still retained ≈ 90% of the initial PCE.[170] Zhu et al. developed an "internal packaging" interface strategy to effectively heal the interface defects over perovskite films by the light-cured cross-linking molecule (BzA). Moreover, the cross-linked interfacial layer will act as an airtight "protective wall", preventing the device from water and oxygen corrosion and lead leakage. Finally, The flexible PSCs show considerable performance of 20.86% with a $V_{oc}$ of 1.12 V. Furthermore, the mechanical stability of flexible PSCs based on the BzA retained 84.5% of initial PCE under 3000 cycles with a curvature radius of 10 mm, while the devices without the modification retain only 80% of the initial PCE at the same bending condition.[171]

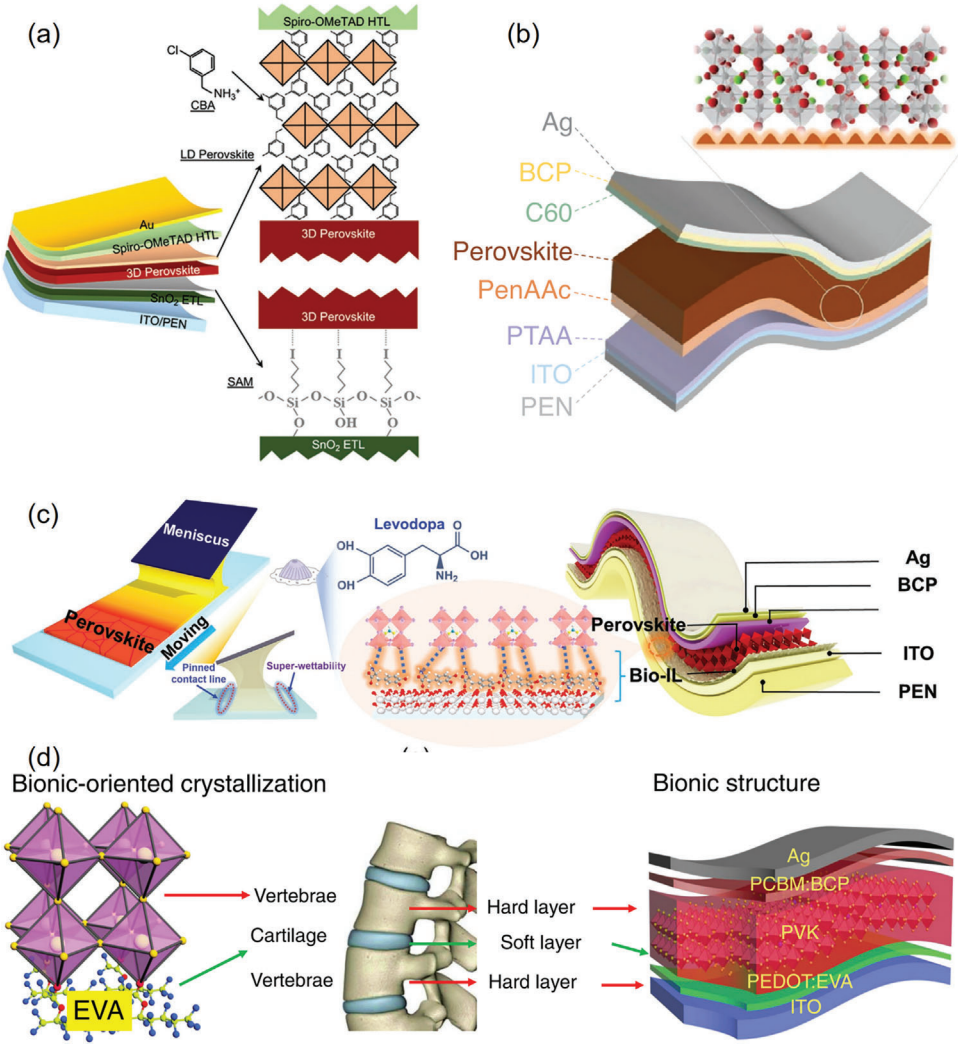


**Figure 13.** Interface engineering for the flexible PSCs. a) The illustration of double-side interfacial modification for the flexible PSCs; Reproduced with permission.[175] Copyright 2022, Wiley-VCH; b) the device structure of PenAAc modified PTAA surface for the flexible PSCs. Reproduced with permission.[173] Copyright 2022, Wiley-VCH; c) The illustration of bionic interface layer modifies the surface wettability for the blade coating flexible PSCs; Reproduced with permission.[177] Copyright 2022, Wiley-VCH; d) the illustration of conductive and glued polymer to fabricate highly bent stable flexible PSCs; Reproduced with permission.[176] Copyright 2020, Springer Nature.

The organic salt was also employed to react with the perovskite layer to further improved the performance of flexible PSCs. Dong et al. employed the FAI organic halide to dope the $SnO_2$ nanocrystals and then reaction formed the interfacial perovskite phase after the perovskite precursor deposition. PSCs with such interfaces deliver efficiencies of up to 20.1% for flexible substrates. Long-term (1000 h) operational stability and bending stability have been improved. Especially, the flexible devices mechanical-bending 2500 cycles still retain 85% initial PCE after the FAI modification, however, the control devices just retain 60% of the initial value.[172] Gao et al. employed the pentylammonium acetate (PenAAc) interface layer between the perovskite and HTL for the flexible inverted PSCs. The $PenA^+$ and $Ac^-$ have strong chemical binding with both acceptor and donor defects of surface-terminating on perovskite films. The PenAAc-modified flexible PSCs achieve a record PCE of 23.68% with a $V_{oc}$ of 1.17 V. Large-area devices (1.0 $cm^2$) also realized an exceptional PCE of 21.52%. In addition, the fabricated PSCs also exhibit excellent stability under mechanical bending, which remains above 91% of the initial PCE even after 5000 bends (Figure 13b).[173] Long et al. developed 4-trifluoromethylphenylethylamine iodide (CF3PEAI) to form a 2D perovskite interface between perovskite and HTL. It is found that the 2D perovskite not only plays a role in aligning energy band between perovskite and HTL but also passivates the traps within the 3D perovskite, thus reducing the interface energy loss and charge carrier recombination, facilitating the interfacial hole transfer. Consequently, the flexible PSCs led to a PCE of 21.1%. Furthermore, the long-term stability of devices is greatly improved through the 2D perovskite layer.[174] Especially, Dai et al. employed the SAM and low-dimensional (LD) perovskite capping layer to modify the double interfaces of ETL/perovskite and perovskite/HTL, respectively. Rational interface engineering results in the enhancement of not only the mechanical properties of both interfaces but also their optoelectronic properties

**Table 10.** Interface engineering for the flexible PSCs.

| Materials | Interface | Perovskite | Structure | $[J_{sc}$ / mA cm$^{-2}]$ | $[V_{oc}$ / V] | FF | PCE / % | Stability | Ref. |
|---|---|---|---|---|---|---|---|---|---|
| CsBr | HTL/Perovskite | $MA_{1-x}FA_xPbI_{3-y}Cl_y$ | p-i-n | 23.5 | 1.09 | 0.751 | 19.2 | 82% (900 h, RH 30%) | 2020[165] |
| $Al(acac)_3$ | ETL/perovskite | $MA_{1-x}FA_xPbI_{3-y}Cl_y$ | n-i-p | 24.69 | 1.133 | 0.746 | 20.87% | 91% (1500 cycles) | 2021[166] |
| PCBM | ETL/perovskite | $MAPbI_3$ | n-i-p | 22.25 | 1.09 | 0.73 | 17.70 | 79% (12 h, 30 °C, RH 40%) | 2018[167] |
| CPTA | ETL/perovskite | $MAPbI_3$ | n-i-p | 22.39 | 1.083 | 0.75 | 18.36 | 75% (500 cycles) | 2019[168] |
| NBDV | ETL/perovskite | $MAPbI_3$ | p-i-n | 23.82 | 1.106 | 0.827 | 21.8 | 84% (8376 h, $N_2$) | 2022[169] |
| P1 | ETL/perovskite | $FAPbI_3$ | n-i-p | 24.34 | 1.182 | 0.743 | 21.4 | 80% (1000 cycles) | 2022[170] |
| BzA | ETL/perovskite | $Cs(FAPbI_3)_x(MAPbBr_3)_{1-x}$ | n-i-p | 23.97 | 1.12 | 0.777 | 20.86 | 84.5% (3000 cycles) | 2022[171] |
| FAI | ETL/perovskite | $Cs_{0.04}(FA_{0.84}MA_{0.16})_{0.96}Pb(I_{0.84}Br_{0.16})_3$ | n-i-p | 22.4 | 1.15 | 0.782 | 20.1 | 85% (2500 cycles) | 2021[172] |
| PenAAc | HTL/perovskite | $Cs_{0.05}(FA_{0.98}MA_{0.02})_{0.95}Pb(I_{0.98}Br_{0.02})_3$ | p-i-n | 24.85 | 1.178 | 0.821 | 23.68 | 91% (5000 cycles) | 2022[173] |
| $CF_3PEAI$ | HTL/perovskite | $FA_{1-x}MA_xPbI_3$ | n-i-p | 23.79 | 1.128 | 0.789 | 21.1 | 90% (3000 cycles) | 2021[174] |
| $Si(OCH_3)_3(CH_2)_3I$/ 3-CBA | ETL/perovskite/ HTL | $(CsPbI_3)_{0.04}$ $[(FAPbI_3)_{0.9}(MAPbBr_3)_{0.1}]_{0.96}$ | n-i-p | 23.39 | 1.138 | 0.790 | 21.03 | 88% (10 000 cycles) | 2022[175] |
| PEDOT:EVA | HTL/perovskite | $(FAPbI_3)_x(MAPbBr_3)_{1-x}$ | p-i-n | 21.26 | 1.18 | 0.79 | 19.87 | 85% (7000 cycles) | 2020[176] |
| Levodopa | HTL/perovskite | $Cs(FAPbI_3)_x(MAPbBr_3)_{1-x}$ | p-i-n | 23.50 | 1.11 | 0.808 | 21.08 | 84.2% (2000 cycles) | 2022[177] |

holistically. As a result, the PCE of corresponding flexible PSCs improved to 21.03% with the excellent operational stability of 1000 h (duration at 90% initial PCE retained). More importantly, the devices bending 10 000 cycles still retained 88% of the initial PCE (**Figure 13**a).[175]

The biomimetic strategy has been also reported to improve the stability of flexible PSCs. Meng et al. inspired by robust crystallization and flexible structure of vertebrae employ a conductive and glued polymer (Poly(3,4-ethylenedioxythiophene):poly(ethyleneco-vinyl acetate), PEDOT:EVA) between indium tin oxide and perovskite layers, which facilitates oriented crystallization of perovskite and sticks the devices. With the results of study, the bionic interface layer accurately controls the crystallization and acts as an adhesive, which improved the performance and stability of flexible PSCs. The devices achieve a PCE of 19.87% with $V_{oc}$ of 1.18 V and FF of 0.79 under the active areas of 1.01 cm$^2$, and it also retained over 85% of initial efficiency after 7000 bending cycles with negligible angular dependence (Figure 13d).[176] Fan et al. inspired by the bio-glue of barnacles, developed a bionic interface layer (Bio-IL) to suppress the coffee-ring effect during printing perovskite layer. The coordination effect of the sticky functional groups in Bio-IL can pin the three-phase contact line and restrain the transport of perovskite colloidal particles during the printing and evaporation process. Moreover, the sedimentation rate of perovskite precursor is accelerated due to the electrostatic attraction and rapid volatilization from an extraordinary wettability. The superhydrophilic Bio-IL affords an even spread over a large-area substrate, which boosts a complete and uniform liquid film for heterogeneous nucleation as well as crystallization. Perovskite films on different large-area substrates with negligible coffee-ring effect are printed. Consequently, inverted flexible PSCs achieve a high efficiency of 21.08%. This strategy ensures a highly reliable reproducibility of printing PSCs with a near 90% yield rate. The flexible device with a bending radius of 3 mm to bend over 2000 cycles, the PCE of the device based on Bio-IL decreased from ≈19% to ≈16%, higher than that of control device (Figure 13c).[177] The detailed photovoltaic parameters and stability are summarized in **Table 10**.

## 7. Interface Engineering for the Mini-modules of PSCs

The fabrication of large-scale modules is important for the commercialization of PSCs, in which the modules usually composed of several series-connected subcells, making the device resistances and defect is more important than the small-area devices as the photo-generated carriers must flow through longer distances. Thus, employing interfacial engineering to control the trap states and the contact of heterojunction within PSCs is significant for highly efficient PSCs modules.

Lee et al. reported 4-fluoro-phenethylammonium iodide (FPEAI) to tune the surface morphology of perovskite. The surface modification of perovskite with FPEAI leads to in situ

generated 2D $(FPEA)_2PbI_4$ perovskite layer on the 3D perovskite. FPEAI modification induces a grain-boundary passivation effect, which suppresses the surface charge recombination. With the modification, the PSCs based on small-area (0.09 $cm^2$) and large-area (2.00 $cm^2$) achieve PCEs of 20.53% and 16.82%, respectively. Furthermore, the 11.2 $cm^2$ large PSC module exhibits a PCE of 13.66%.[178] our previous work reported one-year stable PSCs by employing AVAI fabricated an ultrastable $(HOOC(CH_2)_4NH_3)_2PbI_4/CH_3NH_3PbI_3$ perovskite junction. The 2D/3D forms an organized multi-dimensional interface that yields 12.9% efficiency for carbon-based PSCs. The modules (10×10 $cm^2$) of PSCs deliver 11.2% efficiency and are stable for 10 000 h measured under outputting conditions.[179] Dagar et al. demonstrated the LiF-modified perovskite and the SAM of 2PACz-modified ITO electrodes which largely improve the efficiency of PSCs. The optimized device for the mini-modules achieved a PCE of 19.4% for an active area of 2.2 $cm^2$.[180] Our previous work designed a series of 2D cationic ortho, para, and interposition $PDEAI_2$ isomers (*o*-$PDEAI_2$, *m*-$PEDAI_2$, and *p*-$PEDAI_2$) based on aniline and employed them for the surface modification of perovskite films (Figure 14b). TRPL measurement finds that the 3D perovskite modified with o-$PDEAI_2$ has the longest lifetime, while the para-position isomer exhibits the shortest lifetime, which may be attributed to the different passivating ability of defects. The PSCs based on *o*-$PDEAI_2$ exhibit a higher PCE of 23.92%. In addition, owing to its excellent defect passivation ability, the amplified module achieves PCE of 21.36% (26 $cm^2$).[181] Liu et al. employed EDTAK at ETL/perovskite interface to inhibit the reaction of $OH^-$ in $SnO_2$ with perovskite and tune the energy-level alignment. In addition, regarding the perovskite/HTL interface, by using EAI/MAI to passivate the surface defects of the $Cs_{0.05}FA_{0.54}MA_{0.41}Pb(I_{0.98}Br_{0.02})_3$ perovskite and tune the energy-level alignment (improved the VB of perovskite to −5.40 eV), as well as reduce the influence of moisture in both the top surface region. Based on the double-side modification, the PSCs modules (22.4 $cm^2$) achieved a reverse-scan efficiency of 16.6% (**Figure 14**a). For stability, the modified devices maintained ≈86% of the initial performance after continuous operation for 2000 h.[182]

Others, Sha et al. introduced graphene oxide nano-sheets (BJ-GO) at the perovskite/HTM interface. They find that the compact 2D network immobilizes the iodide ions, and multiple coordination bonds passivate the defects. The PSC module with an area of 35.80 $cm^2$ employing BJ-GO obtained a certified efficiency of 15.3%.[183] Du et al. reported surface redox engineering (SRE) via Ar plasma treatment and the reduction for vacuum-deposited $NiO_x$, making its interface match well with the slot-die-coated perovskite films. The SRE not only solved the de-wetting problem of perovskite on $NiO_x$ but also ameliorated electronic properties at buried contact interfaces. The perovskite modules of area 156 × 156 $mm^2$ exhibit a remarkable PCE of 18.6% (Figure 14c).[184] In our previous work, we reported on a diphenyl iodide cation and pentafluorophenyl boric acid anion-based dopant (DIC-PBA) for the doping of PTAA HTM. We find that DIC-PBA exhibits deep doping of PTAA and also creates interfacial p-doping of perovskite surface. PSCs based on the modules (aperture area: 33.2 $cm^2$) reached an efficiency of 19.13%. The PSCs also exhibit high stability at the air ambient and 85 °C heating conditions.[10]

The flexible PSCs modules are also reported by employing interface engineering. Pisoni et al. demonstrated highly efficient n-i-p PSCs fabricated on flexible substrates by interface engineering. They compared spin-coated PEIE and vacuum-deposited LiF as interlayers between ZnO and $C_{60}$. The interlayers induced a band bending, which resulted in enhanced charge extraction and lower recombination losses. The flexible perovskite module with a stabilized efficiency of 10.5% onto an aperture area larger than 10 $cm^2$ (geometric fill factor ≈94%) after the interfacial modifications.[185] Bu et al. provided a facile interface passivation strategy with potassium treatments for $SnO_2$ ETLs to reduce the interface recombination with a PCE reach 17.09% with an aperture area of 0.16 $cm^2$ after treatments. They also obtained a high PCE of 15.22% for a flexible module (5 × 6 $cm^2$) based on a slot-die-coated Alfa-$SnO_2$ substrate.[186]

Pescetelli et al. employed the 2D f-$MoS_2$ to modify perovskite/PTAA interface and the assembly and integration panels in a solar farm installed in Crete, and the single module efficiency obtained 16.4% (Figure 14d).[187] The solar farm reached a peak power exceeding 250 W working in outdoor conditions. Notably, the author finds that the $V_{oc}$ temperature coefficient of the panels is half the one for c-Si panels. Simultaneously exhibiting a larger positive ISC temperature coefficient which means the perovskite panels are extremely promising for outdoor operation at elevated temperatures in high-irradiance regions. The solar farm experiment shows an environmental profile that might compete with those calculated for the 2050 Europe electricity mix. Furthermore, the environmental footprints of the solar farm calculated for several geographical locations turn out to be lower than the current European electricity mix and are already competitive with the business-as-usual and realistic improvement future scenarios.[187] This work is based on interface engineering, laying the groundwork for commercialization targets of PSCs. The detailed photovoltaic parameters and stability are summarized in **Table 11**.

## 8. Interface Engineering for the Environment Protection

Organic-inorganic lead halide perovskite materials within PSCs are susceptible to moisture, and the perovskite crystal collapses fast in a high-humidity environment. Firstly, the $H_2O$ molecule interacts with the Pb sites of the perovskite crystal and forms a $PbI_2{\cdot}H_2O$ phase, which causes the fast decomposition of perovskite structure.[188] In addition, the perovskite materials are also unstable under high-energy UV irradiation, which usually promotes the degradation of devices under the catalysis of metal oxide ETL, and results in the collapse of the crystal lattice.[150,189] Perovskite materials also exhibit inferior thermal stability due to the low formation energy of the crystal. The long-term heating causes the volatilization of an organic group and leads to the degeneration of perovskite lattice.[190] The decomposition of perovskite components, such as Pb, organic cation, and halogen atoms, migrates to the surface of PSCs electrode after long-term storage, which leads to leakage.[191] Both $Pb^{2+}$ and $Pb^0$ have been proven harmful to the environment and human health. Thus, inhibiting the leakage of PSCs from protecting the environment is also vital for its commercial application.

The encapsulation of the PSCs may be one of strategy to reduce the Pb leakage. Yang et al. dipped halide perovskite film into $(C_8H_{17}NH_3)_2SO_4$ solutions for 30 to 60 min followed by thermal

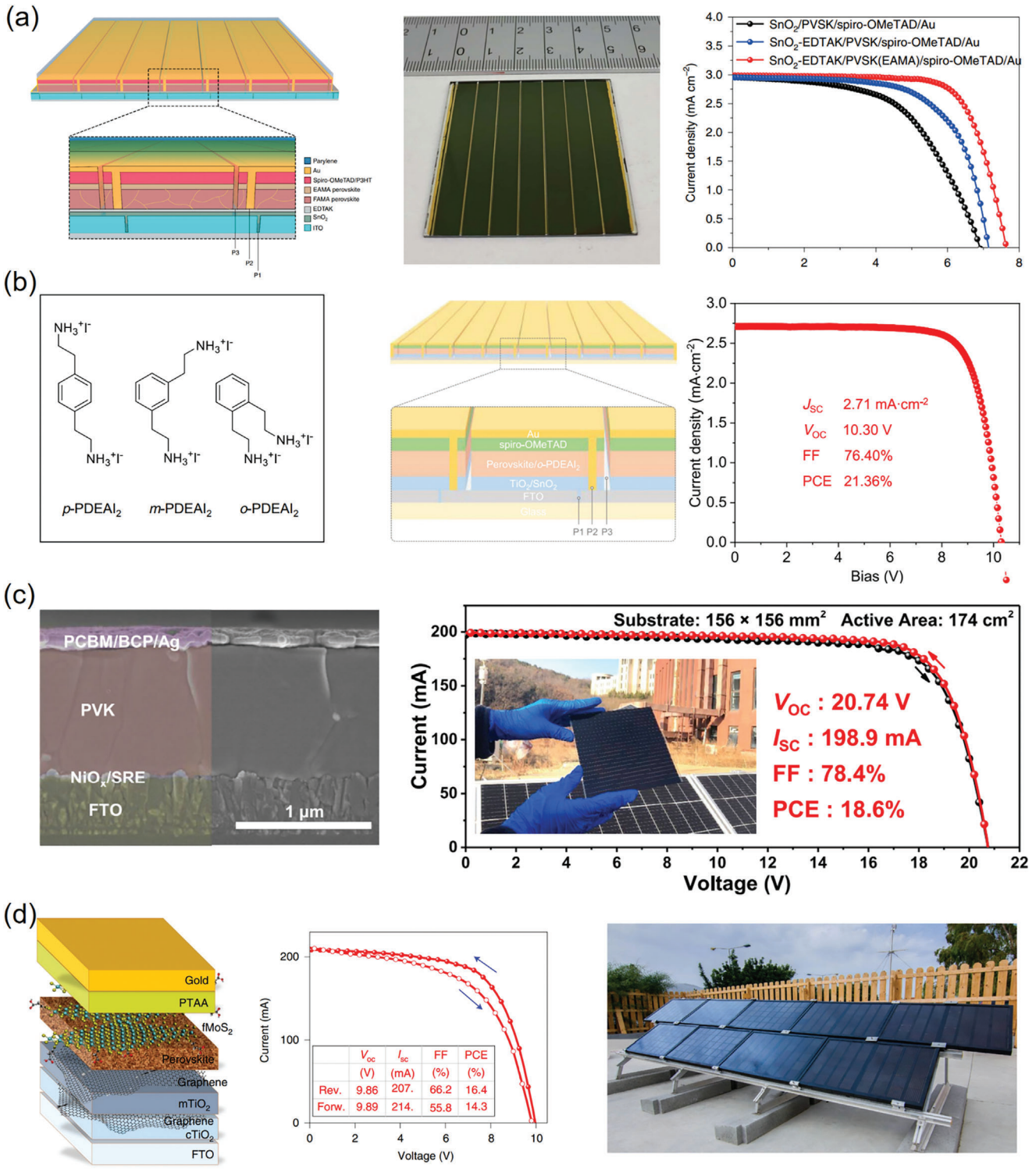


**Figure 14.** The interface engineering for the mini-module fabrication. a) The illustration double side interface modification by EDTAK and the EAMA perovskite, and the digital photograph of the mini-module with a size of 5 × 5 $cm^2$, as well as the *J–V* curve of the corresponding PSCs module; Reproduced with permission.[182] Copyright 2020, Springer Nature; b) the molecule structure of *o*-$PDEAI_2$, *m*-$PEDAI_2$, and *p*-$PEDAI_2$, as well as the illustration of module structure by the interfacial passivation and *J–V* curve of the corresponding PSCs module; Reproduced with permission.[181] Copyright 2022, Springer Nature; c) The cross-sectional SEM of PSCs based on SRE, and the *J–V* curve of corresponding PSCs module; Reproduced with permission.[185] copyright 2022, Elsevier; d) the illustration of the device's structure by the $MoS_2$ interface modification and the *J–V* curve of corresponding PSCs module, as well as the panels integrated modules; Reproduced with permission.[187] Copyright 2022, Springer Nature.

**Table 11.** Interface engineering for the mini-modules of PSCs.

| Materials/ Methods | Perovskite | Structure | Module area | Active area (AC) or aperture area (AP) | PCE / % | Stability | Ref. |
|---|---|---|---|---|---|---|---|
| FPEAI | $FA_{0.85}MA_{0.15}Pb(I_{0.85}Br_{0.15})_3$ | n-i-p | 25 $cm^2$ | AC 11.2 $cm^2$ | 13.66 | 60% (2700 h, RH 15–20%) | 2021[164] |
| AVAI | $MAPbI_3$ | n-i-p | 100 $cm^2$ | AC 47.6 $cm^2$ | 10.1 | Near 100% (10 000 h, ambient condition) | 2017[165] |
| 2PACz | $Cs_{0.05}FA_{0.79}MA_{0.16}PbBr_{0.51}I_{2.49}$ | p-i-n | – | AC 2.2 $cm^2$ | 19.4 | 80% (700 h, MPP) | 2021[166] |
| $PDEAI_2$ | $Cs(FAPbI_3)_x(MAPbBr_3)_{1-x}$ | n-i-p | 45.5 $cm^2$ | AC 26 $cm^2$ | 21.36 | 90% (1100 h, MPP, $N_2$) | 2021[167] |
| EDTAK | $Cs_{0.05}FA_{0.54}MA_{0.41}Pb(I_{0.98}Br_{0.02})_3$ | n-i-p | 25 $cm^2$ | AC 22.4 $cm^2$ | 16.6 | 86% (2000 h, MPP) | 2020[168] |
| BJ-GO | $CsFAPbI_3$ | n-i-p | 64 $cm^2$ | AP 35.8 $cm^2$ | 15.3 | 91% (1000 h, 85 °C, RH 85%) | 2021[169] |
| SRE | $CsFAMAPbI_3$ | p-i-n | 243.4 $cm^2$ | AP 174 $cm^2$ | 18.6 | >90% (1000 h, RH< 20%) | 2022[170] |
| DIC-PBA | $(FAPbI_3)_{0.95}(MAPbBr_3)_{0.05}$ | n-i-p | 45.5 $cm^2$ | AP 33.2 $cm^2$ | 19.13 | 90% (1200 h, ambient condition) | 2022[10] |
| PEIE | $MAPbI_3$ | Flexible p-i-n | – | AP 10 $cm^2$ | 10.5 | – | 2018[171] |
| KOH | $Cs_{0.05}(FA_{0.85}MA_{0.15})_{0.95}Pb(I_{0.85}Br_{0.15})_3$ | Flexible p-i-n | 30 $cm^2$ | AP 16.07 $cm^2$ | 15.22 | – | 2018[172] |

annealing, which formed the dense $PbSO_4$ shelled structure via the in situ reaction at the perovskite surface (**Figure 15**b). The $PbSO_4$ is insulating and almost insoluble in water, which could protect the perovskite film well. Benefit the advantage of $PbSO_4$, the sample of perovskite single crystal which capped the shell layer immersed in water for 60 s without any color change; however, the bare perovskite sample became yellow after 10 s immersion (Figure 15c).[55] Thus, the dense maskant of perovskite reduced the risk of Pb leakage. Li et al. mixed sulfonated graphene aerogels with polydimethylsiloxane as lead-absorbing encapsulants on both sides of flexible PSCs modules. The sulfonated graphene aerogels strongly bind with $Pb^{2+}$, giving them superior lead adsorption capacity in an aqueous solution. Over 99% of $Pb^{2+}$ from the degraded flexible modules have been captured by the encapsulant under scratching, bending, and thermal circling conditions, leading to a reduction of lead leakage to 10 ppb.[192]

Zhang et al. evaporated the 1H,1H,2H,2H-perfluorodecanethiol (PFDT) SAM at a lower temperature of 100 °C on the PSCs (Figure 15a). It is found that the SAM not only bonds with the surface of the Ag electrode via the Ag-S bond but is also anchored at the lateral perovskite surface via the Pb–S interaction, which improves the hydrophobicity of PSCs and inhibits the leakage of the Pb, as well as finally minimizing the Pb leakage to 2.05 ppm. The study also indicated that the interaction with perovskite might relieve the Pb leakage, except for the PSCs encapsulation.[193] The chemical interactions at the internal layer of PSCs also have been developed to reduce the risk of Pb leakage. Bi et al. dissolved 3-mercaptopropyltriethoxysilane (SiSH) into the anti-solvent chlorobenzene (CB) and dipped it on perovskite film during spin-coating. It passivated interfacial defects and facilitated perovskite crystallization, enhancing device stability by releasing interfacial stress. Especially, the interaction between perovskite and the SiSH reduced the irreversible environmental pollution by preventing lead leakage. Although the SiSH has prevented the $Pb^{2+}$ from dissolving in deionized water, there is still a large disparity with the drinking water. They further synthesized an adsorbent benzene-1,4-dithiocarboxamide (BD) and added it into the water; the $Pb^{2+}$ concentration in deionized water and simulated acidic rain conditions reduced to 11.09 and 9.07 μg $L^{-1}$, which is close to the standards for drinking water quality of Japan and China. It indicates S, N, and O elements contained materials as the interfacial layer will reduce the leakage of Pb.[194]

He et al. introduced interfacial crosslinking agent D-penicillamine (DPM) at the surface of $SnO_2$, the O atoms interacted on the $Sn^{4+}$ of ETL, and the exposed S atoms strongly interacted with the Pb atom of perovskite, which passivated the trap states to achieve an efficiency of 24.09%. In addition, unencapsulated PSCs exhibit better stability than the controlled device. Owing to the interaction induced better stability, making less Pb leakage into the environment.[195] Xiao et al. employed thiol-based CuP to post-treat the perovskite film. The thiol group in CuP reacts with Pb ion at perovskite film to form the Pb–S bond and efficiently encapsulate the perovskite film to improve the PSCs stability and prevent the leakage of noxious Pb.[196] Lee et al. reported a donor-acceptor type polymer composed of benzo[1,2-b:4,5:b′]dithiophene and tetraethylene glycol (TEG)-substituted 2,1,3-benzothiadiazole to prevent possible lead leakage via chelation at the contact interface. The nuclear magnetic resonance reveals that TEG groups can chelate lead ions with moderate strength ($K_{binding}$ = 2.76), which prevents lead leakage.[197]

Chen et al. reported a chemically robust cation-exchange resin (CER) method to prevent lead leakage from damaged PSCs modules. CERs exhibit both high adsorption capacity and high adsorption rate of lead in water due to the high binding energy with $Pb^{2+}$. Employing CERs, reduced lead leakage from modules by 62-fold to 14.3 ppb in water.[198] They further reported a new device structure incorporating a mesoporous sulfonic acid-based lead-adsorbing resin into PTAA/perovskites interface, immobilizing lead ions inside even if perovskites are exposed to rainwater. This structure proved to be more effective in preventing lead leakage and reducing the lead contamination of rainwater from damaged modules to 11.9 parts per billion.[199]

Wu et al. used a thiol-functionalized 2D conjugated MOF as an electron-extraction layer at the perovskite/cathode interface to maintain long-term operational stability and minimize potentially leaked lead ($Pb^{2+}$) ions (Figure 15d). The resultant devices

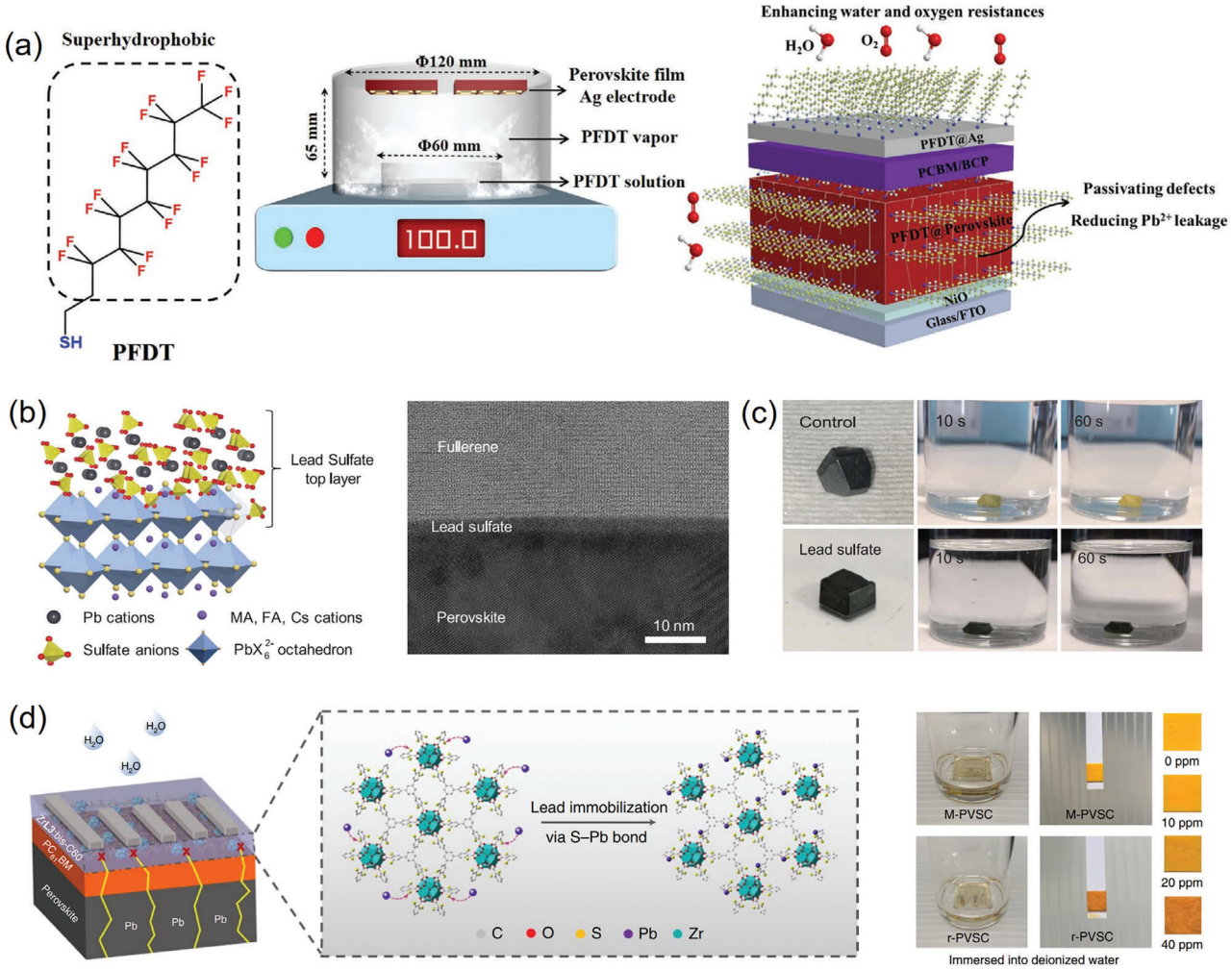


**Figure 15.** The strategies for inhibiting Pb leakage. a) The illustration of deposit PFDT on the PSCs, and the illustration of inhibit Pb leakage; Reproduced with permission.[193] Copyright 2021, Wiley-VCH; b) the illustration of $PbSO_4$ interacted with perovskite film, and the cross-sectional SEM of the $PbSO_4$ encapsulated perovskite;[55] c) the immersion in water of $PbSO_4$ single crystal and perovskite single crystal; Reproduced with permission.[55] Copyright 2019, American Association for the Advancement of Science; d) the illustration of 2D MOF employed to reduce the Pb leakage, and the corresponding Pb leakage measurement. Reproduced with permission.[200] Copyright 2020, Springer Nature.

exhibit high power conversion efficiency (22.02%) along with substantially improved long-term operational stability. The functionalized metal–organic framework could capture most of the $Pb^{2+}$ leaked via the chelation from the degraded PSCs.[200]

## 9. Challenges and Promising Strategies

The interface engineering of PSCs has achieved remarkable progress within heterojunction contact, defect passivation, large-area manufacturing, environmental protection, device internal stability and external environmental stability (temperature, ambient, and light conditions), and the corresponding mechanism research. However, there are also some challenges and questions that still need to be solved and answered for the commercialization of the technology in the near future:

1) The amelioration of interfacial energy level is a common phenomenon when interacting with the interface materials. However, there is some confusion between the energy level position and interface carrier dynamics.[24,66,67,69] Generally, the down-shifting of CB of ETL (up-shifting of HOMO of HTL) by tailoring the $E_F$ or the energy level itself increases the energy gap with the perovskite, which usually fasting the interface carrier injection and transportation. However, the higher energy gap will increase the interfacial barriers which dominated the recombination. Inversely, the reduced energy gap results in lower interfacial barriers but inferior interface $E_{bi}$ (**Figure 16**a). The qualitative analysis of the novel interfacial materials design and make interface engineering invariably rests on the experimental results. Thus, it is crucial and urgent to clarify the relation of interfacial energy level for the interfacial carrier dynamics; however, there is no work to give the specific value of the energy gap of interfacial to distinguish the recombination and transportation process.
2) Despite the remarkable progress of all kinds of interfacial materials applied in highly efficient and stable PSCs, which

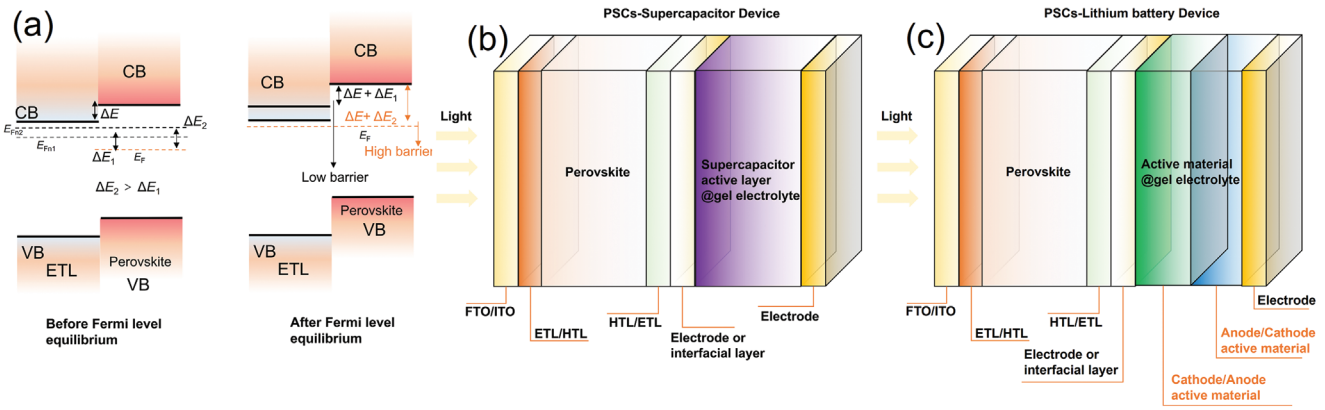


**Figure 16.** Challenges and promising strategies. a) The illustration of the problem of the interface energy level match; b) the illustration of optical energy storage integrated device of PSCs-Supercapacitor device; c) the illustration of optical energy storage integrated device of PSCs-Lithium battery device.

passivated the trap states and matched the interfacial energy level, the environmental problems caused by the Pb toxicity of PSCs have received relatively little attention. The averting of Pb leakage is mainly reduced via electrode interface encapsulation and surface chemical interaction, but the device efficiency is lower than other strategies. In the future, developing novel interfacial strategies or materials to achieve efficient and eco-friendly PSCs fabrication is also important and urgent. Metallic organic framework (MOF)[200] and Covalent organic framework (COF)[201] are the potential interface materials as the strongly heavy-metal adsorption capacity and manifold structure, which by turning the molecules dimension, structure, and ligands will be unique to match the interfacial energy level, trap passivation and inhibit the metal ion migrations.

3) The ultra-thin insulating layer interface modification material effectively inhibits the electron-hole pairs recombination at the interfaces and the interfacial carrier transportation via the interface tunnel effect. The excessively thick interface layer would improve the stability of PSCs but impeded the interface carrier extraction. Moreover, the report of the insulating passivation layers so far is relatively sparse, mainly containing PMMA,[162] PS,[157] PVP,[159] and PEO.[163] In the future, functional groups with electronic properties can be introduced through molecular engineering to adjust both the interface transport and trap states passivation and interfacial ionic migration, achieving high efficiency with increasing thickness and further improving the stability of PSCs.
4) Large-scale PSCs modules are achieving considerable efficiency and stability through interface engineering. Flexible modules have the advantages of being portable, lightweight, flexible, and other characteristics, which make them widely used for non-planar geometric surfaces, wearable electronic devices, aerospace, etc. However, the efficiency is much lower than that of PSCs based on the rigid substrate due to the difficulty of spin-coating and the conductivity; also, the hydrophilicity of the substrate is poor compared with rigid.[186] Scraping and roll-to-roll method will solve the problem of the spin-coating of flexible modules; however, the perovskite film is un-perfect due to the poor wettability. Therefore, the interfacial materials can be developed in the future to ameliorate the surface energy of the substrate and the adhesion of perovskite precursor, and thus fabricate the high-quality perovskite film as well as passivate the trap states and turn the energy level. The novel interfacial materials design lays a foundation for future portable energy and aerospace of PSCs.
5) Although PSCs effectively convert solar energy into electricity through a photoelectric effect to supply electronic equipment, their power generation is intermittent. In the future, an integrated PSCs device coupled with energy storage devices can be developed to achieve a continuous energy supply, such as the PSCs-Super capacitors (Figure 16b) and PSCs-lithium-ion battery (Figure 16c). Interface engineering will play an essential role in the interface connection. In addition, integrating novel light emitting and PSCs devices is also of great significance in future research to achieve intelligent in situ photoelectric to electro-optical reversible conversion.

## 10. Conclusions and Outlook

In this review, we have summarized the recent progress of interface engineering of PSCs toward multiple interfaces and discussed the basic electron transfer mechanism for trap states passivation and energy level shifting and the critical factors of the interface tailoring from the different types of materials, as well as introduced the general research method of DFT for the interface modification mechanism study. Additionally, the review also summarized the application of interface engineering for environmental protection and large-scale module fabrication. The interfacial modification can be classified into two species; the surface electronic properties changed (such as the surface trap states and energy level changed) and the without surface change of relative interface (such as the insulating tunneling layer). For the electronic properties tailored interface, the materials are multitudinous, containing ionic liquid, zwitterion, small molecule, fullerene derivative, metal salt, low-dimensional perovskite halide salt, quantum dots, and polymers et al.; however, the developing of insulating tunneling layer is scarce. For the energy level properties changed within the semiconductor surface, the basic mechanism can be attributed to: i) the surface dipole by

the semiconductor-molecules anchoring induced charge transfer, such as the ionic type molecules and small molecules or adsorbed ions; however, there are rarely reported on the important dipole orientation study and usually neglected the anti-dipole from the semiconductor-molecules interface; ii) the donor or acceptor of the electron from semiconductor, which is common in the electronic donor and acceptor type molecules, but it related to the electron affinity and ionization energy. Trap passivation also belongs to two types; one is the ionic type molecules induced local electrical neutralization. Second is the surface charge transfer induced charge compensation by the donor and acceptor type molecules, including the donor group's lone pair electron coordination. However, there is confusion about building the specific energy level, trap states change by the quantitative molecular properties.

Furthermore, The DFT methods, including molecular dynamics, binding energy, electron localization function, charge density difference, band structure, and orbitals distribution, are fundamental to the internal study of the surface interaction, bond type, charge distribution, energy level shifting, trap passivation by interface modification and its inner mechanism. By employing interface engineering and interface design, the large-scale modules also progressed significantly; the efficiency and stability seemingly meet the standard of commercialization, but the development of flexible devices of large scale is relatively lagging, which is important for wearable devices and the aerospace industry. The future environmental protection research for PSCs is also pressing due to the high potential for commercialization. In addition, the future design of perovskite interface will be toward multi-physical scale simulation combined with material properties, interface defects, energy level, and diversified development to quantitatively analyze the influence of interface modification on the interface properties of PSCs. Meanwhile, it is of great significance to construct integrated devices of photoelectric-electric energy storage, photoelectric-chemical energy storage, photoelectric-electrooptical conversion, and series solar cells through interface modification for the rational use of energy in the future and developing of multifunctional self-energized electronic devices.

## Acknowledgements

The authors thank the Qatar National Research Fund (a member of Qatar Foundation) for grant no. NPRP11S-1231-170150, for financial support.

Open access funding provided by Ecole Polytechnique Federale de Lausanne.

## Conflict of Interest

The authors declare no conflict of interest.

## Keywords

electron transfers, energy levels, interface engineering, perovskite solar cells, trap states

Received: December 4, 2022
Revised: February 7, 2023
Published online: July 2, 2023

[1] G. Hodes, *Science* **2013**, *342*, 317.
[2] G. Xing, N. Mathews, S. Sun, W. Lim, Y. M. Lam, M. Grätzel, S. Mhaisalkar, T. C. Sum, *Science* **2013**, *342*, 344.
[3] National Renewable Energy Laboratory, Best Research Cell Efficiency https://www.nrel.gov/pv/cell-efficiency.html (accessed: July 2022).
[4] A. Kojima, K. Teshima, Y. Shirai, T. Miyasaka, *J. Am. Chem. Soc.* **2009**, *131*, 6050.
[5] T. Han, S. Tan, J. Xue, L. Meng, J. Lee, Y. Yang, *Adv. Mater.* **2019**, *31*, 1803515.
[6] X. Zheng, B. Chen, J. Dai, Y. Fang, Y. Bai, Y. Lin, H. Wei, X. Zeng, J. Huang, *Nat. Energy* **2017**, *2*, 17102.
[7] H. Tan, A. Jain, O. Voznyy, X. Lan, F. P. G. Arquer, J. Z. Fan, R. Quintero-Bermudez, M. Yuan, B. Zhang, Y. Zhao, F. Fan, P. Li, L. N. Quan, Y. Zhao, Z. Lu, Z. Yang, S. Hoogland, E. H. Sargent, *Science* **2017**, *355*, 722.
[8] J. Ye, C. Liu, D. Mei, Q. Ge, *ACS Catal.* **2013**, *3*, 1296.
[9] T. W. Jones, A. Osherov, M. Alsari, M. Sponseller, B. C. Duck, Y. K. Jung, C. Settens, F. Niroui, R. Brenes, C. V. Stan, Y. Li, M. Abdi-Jalebi, N. Tamura, J. E. Macdonald, M. Burghammer, R. H. Friend, V. Bulović, A. Walsh, G. J. Wilson, S. Lilliu, S. D. Stranks, *Energy Environ. Sci.* **2019**, *12*, 596.
[10] J. Xia, Y. Zhang, C. Xiao, K. G. Brooks, M. Chen, J. Luo, H. Yang, N. I. D. Klipfel, J. Zou, Y. Shi, X. Yao, J. Chen, J. M. Luther, H. Lin, A. M. Asiri, C. Jia, M. K. Nazeeruddin, *Joule* **2022**, *6*, 1689.
[11] C. Ran, J. Xu, W. Gao, C. Huang, S. Dou, *Chem. Soc. Rev.* **2018**, *47*, 4581.
[12] Z. Xiao, Y. Yuan, Y. Shao, Q. Wang, Q. Dong, C. Bi, P. Sharma, A. Gruverman, J. Huang, *Nat. Mater.* **2015**, *14*, 193.
[13] K. Choi, J. Lee, H. Il Kim, C. W. Park, G. Kim, H. Choi, S. Park, S. A. Park, T. Park, *Energy Environ. Sci.* **2018**, *11*, 3238.
[14] K. Kawano, C. Adachi, *Adv. Funct. Mater.* **2009**, *19*, 3934.
[15] S. A. L. Weber, I. M. Hermes, S. Turren-Cruz, C. Gort, V. W. Bergmann, L. Gilson, A. Hagfeldt, M. Grätzel, W. Tress, R. Berger, *Energy Environ. Sci.* **2018**, *11*, 2404.
[16] Z. Liu, Q. Chen, J. Lee, Z. Zhao, X. Xu, Y. Hsieh, L. Meng, P. Sun, N. D. Marco, H. Zhou, Y. Cheng, Y. Yang, *Adv. Energy Mater.* **2018**, *8*, 1800568.
[17] J. Dou, Y. Bai, Q. Chen, *Mater. Chem. Front.* **2022**, *6*, 2779.
[18] W. Tress, *Adv. Energy Mater.* **2017**, *7*, 1602358.
[19] H. Pan, H. Shao, X. Zhang, Y. Shen, M. Wang, *J. Appl. Phys.* **2021**, *129*, 130904.
[20] H. Kim, K. S. Lee, M. J. Paik, D. Y. Lee, S.-U. Lee, E. Choi, J. S. Yun, S. Il Seok, *Adv. Funct. Mater.* **2022**, *32*, 2110473.
[21] O. D. Miller, E. Yablonovitch, S. R. Kurtz, *IEEE J Photovolt* **2012**, *2*, 303.
[22] R. T. Ross, *J. Chem. Phys.* **1967**, *46*, 4590.
[23] W.-J. Yin, T. Shi, Y. Yan, *Appl. Phys. Lett.* **2014**, *104*, 063903.
[24] J. Xia, J. Luo, H. Yang, F. Zhao, Z. Wan, H. A. Malik, Y. Shi, K. Han, X. Yao, C. Jia, *Adv. Funct. Mater.* **2020**, *30*, 2001418.
[25] J. Xia, R. Zhang, J. Luo, H. Yang, H. Shu, H. A. Malik, Z. Wan, Y. Shi, K. Han, R. Wang, X. Yao, C. Jia, *Nano Energy* **2021**, *85*, 106018.
[26] S. Zhang, H. Si, W. Fan, M. Shi, M. Li, C. Xu, Z. Zhang, Q. Liao, A. Sattar, Z. Kang, Y. Zhang, *Angew Chem. Int. Ed.* **2020**, *59*, 11573.
[27] Y. Tan, H. Cheng, Y. Zhao, Z. Wang, *J. Mater. Chem. A* **2022**, *10*, 7173.
[28] A. Krishna, H. Zhang, Z. Zhou, T. Gallet, M. Dankl, O. Ouellette, F. T. Eickemeyer, F. Fu, S. Sanchez, M. Mensi, S. M. Zakeeruddin, U. Rothlisberger, G. N. M. Reddy, A. Redinger, M. Grätzel, A. Hagfeldt, *Energy Environ. Sci.* **2021**, *14*, 5552.
[29] L. Najafi, B. Taheri, B. Martín-García, S. Bellani, D. D. Girolamo, A. Agresti, R. Oropesa-Nuñez, S. Pescetelli, L. Vesce, E. Calabrò, M. Prato, A. E. D. R. Castillo, A. D. Carlo, F. Bonaccorso, *ACS Nano* **2018**, *12*, 10736.

[30] N. K. Noel, S. N. Habisreutinger, A. Pellaroque, F. Pulvirenti, B. Wenger, F. Zhang, Y. Lin, O. G. Reid, J. Leisen, Y. Zhang, S. Barlow, S. R. Marder, A. Kahn, H. J. Snaith, C. B. Arnold, B. P. Rand, *Energy Environ. Sci.* **2019**, *12*, 3063.
[31] J. Han, H. Kwon, E. Kim, H. J. Son, D. H. Kim, *J. Mater. Chem. A* **2020**, *8*, 2105.
[32] H. Han, H. Choi, S. Mhin, Y.-R. Hong, K. M. Kim, J. Kwon, G. Ali, K. Y. Chung, M. Je, H. N. Umh, D.-H. Lim, K. Davey, S.-Z. Qiao, U. Paik, T. Song, *Energy Environ. Sci.* **2019**, *12*, 2443.
[33] P. Cui, D. Wei, J. Ji, H. Huang, E. Jia, S. Dou, T. Wang, W. Wang, M. Li, *Nat. Energy* **2019**, *4*, 150.
[34] M. Casalegno, G. Raos, R. Po, *J. Chem. Phys.* **2010**, *132*, 094705.
[35] A. Miller, E. Abrahams, *Phys. Rev.* **1960**, *120*, 745.
[36] W. Chen, Y. Zhou, L. Wang, Y. Wu, B. Tu, B. Yu, F. Liu, H.-W. Tam, G. Wang, A. B. Djurišić, L. Huang, Z. He, *Adv. Mater.* **2018**, *30*, 1800515.
[37] B. Tu, Y. Shao, W. Chen, Y. Wu, X. Li, Y. He, J. Li, F. Liu, Z. Zhang, Y. Lin, X. Lan, L. Xu, X. Shi, A. M. C. Ng, H. Li, L. W. Chung, A. B. Djurišić, Z. He, *Adv. Mater.* **2019**, *31*, 1805944.
[38] L. Canil, T. Cramer, B. Fraboni, D. Ricciarelli, D. Meggiolaro, A. Singh, M. Liu, M. Rusu, C. M. Wolff, N. Phung, Q. Wang, D. Neher, T. Unold, P. Vivo, Al. Gagliardi, F. D. Angelis, A. Abate, *Energy Environ. Sci.* **2021**, *14*, 1429.
[39] C. M. Wolff, L. Canil, C. Rehermann, N. Ngoc Linh, F. Zu, M. Ralaiarisoa, P. Caprioglio, L. Fiedler, M. Stolterfoht, S. Kogikoski Jr., I. Bald, N. Koch, E. L. Unger, T. Dittrich, A. Abate, D. Neher, *ACS Nano* **2020**, *14*, 1445.
[40] B. de Boer, A. Hadipour, M. M. Mandoc, T. van Woudenbergh, P. W. M. Blom, *Adv. Mater.* **2005**, *17*, 621.
[41] F. Ali, C. Roldán-Carmona, M. Sohail, M. K. Nazeeruddin, *Adv. Energy Mater.* **2020**, *10*, 2002989.
[42] F. D. Angelis, *Acc. Chem. Res.* **2014**, *47*, 3349.
[43] J. Su, T. Zhu, T. Pauporté, I. Ciofini, F. Labat, *J. Comput. Chem.* **2020**, *41*, 1740.
[44] M. J. Frisch, G. W. Trucks, H. B. Schlegel, G. E. Scuseria, M. A. Robb, J. R. Cheeseman, G. Scalmani, V. Barone, G. A. Petersson, H. Nakatsuji, X. Li, M. Caricato, A. Marenich, J. Bloino, B. G. Janesko, R. Gomperts, B. Mennucci, H. P. Hratchian, J. V. Ortiz, A. F. Izmaylov, J. L. Sonnenberg, D. Williams-Young, F. Ding, F. Lipparini, F. Egidi, J. Goings, B. Peng, A. Petrone, T. Henderson, D. Ranasinghe, et al., Gaussian 09, Revision A.02, Gaussian Inc. , Wallingford CT **2016**.
[45] S. J. Clark, M. D. Segall, C. J. Pickard, P. J. Hasnip, M. I. J. Probert, K. Refson, M. C. Payne, *Z. Kristallogr.* **2005**, *220*, 567.
[46] G. Kresse, J. Furthmüller, *Phys. Rev. B* **1996**, *54*, 11169.
[47] P. Giannozzi, S. Baroni, N. Bonini, M. Calandra, R. Car, C. Cavazzoni, D. Ceresoli, G. L Chiarotti, M. Cococcioni, I. Dabo, A. D. Corso, S. d. Gironcoli, S. Fabris, G. Fratesi, R. Gebauer, U. Gerstmann, C. Gougoussis, A. Kokalj, M. Lazzeri, L. Martin-Samos, N. Marzari, F. Mauri, R. Mazzarello, S. Paolini, A. Pasquarello, L. Paulatto, C. Sbraccia, S. Scandolo, G. Sclauzero, A. P Seitsonen, et al., *J Phys Condens Matter* **2009**, *21*, 395502.
[48] T. D. Kühne, M. Iannuzzi, M. D. Ben, V. V. Rybkin, P. Seewald, F. Stein, T. Laino, R. Z. Khaliullin, O. Schütt, F. Schiffmann, D. Golze, J. Wilhelm, S. Chulkov, M. H. Bani-Hashemian, V. Weber, U. Borštnik, M. Taillefumier, A. S. Jakobovits, A. Lazzaro, H. Pabst, T. Müller, R. Schade, M. Guidon, S. Andermatt, N. Holmberg, G. K. Schenter, A. Hehn, A. Bussy, F. Belleflamme, G. Tabacchi, et al., *J. Chem. Phys.* **2020**, *152*, 194103.
[49] Q. Hu, E. Rezaee, W. Xu, R. Ramachandran, Q. Chen, H. Xu, T. EL-Assaad, D. V. McGrath, Z. Xu, *Small* **2021**, *17*, 2005216.
[50] G. D. Liberto, S. Tosoni, G. Pacchioni, *ChemCatChem* **2020**, *12*, 2097.
[51] H. Shu, J. Xia, H. Yang, J. Luo, Z. Wan, H. A. Malik, F. Han, X. Yao, C. Jia, *ACS Sust. Chem. Eng.* **2020**, *8*, 10859.
[52] T.-H. Han, J.-W. Lee, C. Choi, S. Tan, C. Lee, Y. Zhao, Z. Dai, N. D. Marco, S.-J. Lee, S.-H. Bae, Y. Yuan, H. M. Lee, Y. Huang, Y. Yang, *Nat. Commun.* **2019**, *10*, 520.
[53] X. Zhou, L. Zhang, J. Yu, D. Wang, C. Liu, S. Chen, Y. Li, Y. Li, M. Zhang, Y. Peng, Y. Tian, J. Huang, X. Wang, X. Guo, B. Xu, *Adv. Mater.* **2022**, *34*, 2205809.
[54] S. You, H. Wang, S. Bi, J. Zhou, L. Qin, X. Qiu, Z. Zhao, Y. Xu, Y. Zhang, X. Shi, H. Zhou, Z. Tang, *Adv. Mater.* **2018**, *30*, 1706924.
[55] S. Yang, S. Chen, E. Mosconi, Y. Fang, X. Xiao, C. Wang, Y. Zhou, Z. Yu, J. Zhao, Y. Gao, F. D. Angelis, J. Huang, *Science* **2019**, *365*, 473.
[56] A. D. Becke, K. E. A. Edgecombe, *J. Chem. Phys.* **1990**, *92*, 5397.
[57] L. De Santis, R. Resta, *Surf. Sci.* **2000**, *450*, 126.
[58] X. Gong, L. Guan, H. Pan, Q. Sun, X. Zhao, H. Li, H. Pan, Y. Shen, Y. Shao, L. Sun, Z. Cui, L. Ding, M. Wang, *Adv. Funct. Mater.* **2018**, *28*, 1804286.
[59] Y. Cao, Z. Deng, M. Wang, J. Bai, S. Wei, H. Feng, *J. Phys. Chem. C* **2018**, *122*, 17228.
[60] Q. Ou, Y. Zhang, Z. Wang, J. A. Yuwono, R. Wang, Z. Dai, W. Li, C. Zheng, Z. Xu, X. Qi, S. Duhm, N. V. Medhekar, H. Zhang, Q. Bao, *Adv. Mater.* **2018**, *30*, 1705792.
[61] K. Wang, X. Liu, R. Huang, C. Wu, D. Yang, X. Hu, X. Jiang, J. C. Duchamp, H. Dorn, S. Priya, *ACS Energy Lett.* **2019**, *4*, 1852.
[62] H. W. Qiao, S. Yang, Y. Wang, X. Chen, T. Y. Wen, L. J. Tang, Q. Cheng, Y. Hou, H. Zhao, H. G. Yang, *Adv. Mater.* **2018**, *31*, 1804217.
[63] A. Agresti, A. Pazniak, S. Pescetelli, A. Di Vito, D. Rossi, A. Pecchia, M. Auf der Maur, A. Liedl, R. Larciprete, D. V. Kuznetsov, D. Saranin , A. D. Carlo, *Nat. Mater.* **2019**, *18*, 1228.
[64] V. I. E. Queloz, M. E. F. Bouduban, I. García-Benito, A. Fedorovskiy, S. Orlandi, M. Cavazzini, G. Pozzi, H. Trivedi, D. C. Lupascu, D. Beljonne, J.-E Moser, M. K. Nazeeruddin, C. Quarti, G. Grancini, *Adv. Funct. Mater.* **2020**, *30*, 2000228.
[65] T. Wang, Y. Li, Q. Cao, J. Yang, B. Yang, X. Pu, Y. Zhang, J. Zhao, Y. Zhang, H. Chen, A. Hagfeldt, X. Li, *Energy Environ. Sci.* **2022**, *15*, 4414.
[66] D. Yang, X. Zhou, R. Yang, Z. Yang, W. Yu, X. Wang, C. Li, S. Liu, R. P. H. Chang, *Energy Environ. Sci.* **2016**, *9*, 3071.
[67] N. K. Noel, S. N. Habisreutinger, B. Wenger, Y.-H. Lin, F. Zhang, J. B. Patel, A. Kahn, M. B. Johnston, H. J. Snaith, *Adv. Energy Mater.* **2019**, *10*, 1903231.
[68] H. Zhang, S. Xu, T. Guo, D. Du, Y. Tao, L. Zhang, G. Liu, X. Chen, J. Ye, Z. Guo, H. Zheng, H. Zhang, S. Xu, T. Guo, *ACS Appl. Mater. Interfaces* **2022**, *14*, 28826.
[69] J. Xia, J. Luo, H. Yang, C. Sun, Z. Wan, H. A. Malik, H. Zhang, Y. Shi, C. Jia, *Nano Energy* **2019**, *66*, 104098.
[70] P. Caprioglio, D. S. Cruzc, S. Caicedo-Dávila, F. Zu, A. A. Sutanto, F. Peña-Camargo, L. Kegelmann, D. Meggiolarom, L. Gregorin, C. M. Wolff, Burkhard Stiller, L. Perdigón-Toro, H. Kobler, B. Li, E. Gutierrez-Partida, I. Lauermann, A. Abate, N. Koch, F. D. Angelis, B. Rech, G. Grancini, D. Abou-Ras, M. K. Nazeeruddin, M. Stolterfoht, S. Albrecht, M. Antonietti, D. Neher, *Energy Environ. Sci.* **2021**, *14*, 4508.
[71] D. Yang, R. Yang, X. Ren, X. Zhu, Z. Yang, C. Li, S. Liu, *Adv. Mater.* **2016**, *28*, 1600446.
[72] C. Duan, J. Cao, Z. Liang, Y. Ming, J. Li, L. Zhao, B. Dong, J. Li, C. Wu, S. Wang, *Sol. RRL* **2021**, *5*, 2100648.
[73] L. Yang, J. Feng, Z. Liu, Y. Duan, S. Zhan, S. Yang, K. He, Y. Li, Y. Zhou, N. Yuan, J. Ding, S. Liu, *Adv. Mater.* **2022**, *34*, 2201681.
[74] C. Zhang, S. Yuan, Y. Lou, Q. Liu, M. Li, H. Okada, Z. Wang, *Adv. Mater.* **2020**, *32*, 2001479.
[75] E. H. Jung, B. Chen, K. Bertens, M. Vafaie, S. Teale, A. Proppe, Y. Hou, T. Zhu, C. Zheng, E. H. Sargent, *ACS Energy Lett.* **2020**, *5*, 2796.
[76] J. Chen, X. Zhao, S. Kim, N. Park, *Adv. Mater.* **2019**, *31*, 1902902.
[77] L. Wang, J, Xia, Z. Yan, P. Song, C. Zhen, X. Jiang, G. Shao, Z. Qiu, Z. Wei, J. Qiu, M. K. Nazeeruddin, *Adv. Funct. Mater.* **2022**, *32*, 2204725.

[78] Z. Qin, Y. Chen, X. Wang, N. Wei, X. Liu, H. Chen, Y. Miao, Y. Zhao, *Adv. Mater.* **2022**, *34*, 2203143.
[79] S. Sonmezoglu, S. Akin, *Nano Energy* **2020**, *76*, 105127.
[80] Z. Li, B. Li, X. Wu, S. A. Sheppard, S. Zhang, D. Gao, N. J. Long, Z. Zhu, *Science* **2022**, *376*, 416.
[81] L. Wang, L. Fu, B. Li, H. Li, L. Pan, B. Chang, L. Yin, *Sol. RRL* **2021**, *5*, 2000720.
[82] Q. Lou, Y. Han, C. Liu, K. Zheng, J. Zhang, X. Chen, Q. Du, C. Chen, Z. Ge, *Adv. Energy Mater.* **2021**, *11*, 2101416.
[83] X. Zhao, L. Tao, H. Li, W. Huang, P. Sun, J. Liu, S. Liu, Q. Sun, Z. Cui, L. Sun, Y. Shen, Y. Yang, M. Wang, *Nano Lett.* **2018**, *18*, 2442.
[84] Z. Dai, S. K. Yadavalli, M. Chen, A. Abbaspourtamijani, Y. Qi, N. P. Padture, *Science* **2021**, *372*, 618.
[85] Y. Shi, H. Zhang, X. Tong, X. Hou, F. Li, Y. Du, S. Wang, Q. Zhang, P. Liu, X. Zhao, *Sol. RRL* **2021**, *5*, 2100128.
[86] M. Hou, H. Zhang, Z. Wang, Y. Xia, Y. Chen, W. Huang, *ACS Appl. Mater. Interfaces* **2018**, *10*, 30607.
[87] J. Wang, S. Fu, L. Huang, Y. Lu, X. Liu, J. Zhang, Z. Hu, Y. Zhu, *Adv. Energy Mater.* **2021**, *11*, 2102724.
[88] L. Huang, D. Zhang, S. Bu, R. Peng, Q. Wei, Z. Ge, *Adv. Sci.* **2020**, *7*, 1902656.
[89] T. Cao, Z. Wang, Y. Xia, B. Song, Y. Zhou, N. Chen, Y. Li, *ACS Appl. Mater. Interfaces* **2016**, *8*, 18284.
[90] R. D. Chavan, D. Prochowicz, B. Bończak, M. M. Tavakoli, P. Yadav, M. Fiałkowski, C. K. Hong, *Adv. Mater. Interf.* **2020**, *7*, 2001144.
[91] W. Zhou, J. Zhen, Q. Liu, Z. Fang, D. Li, P. Zhou, T. Chen, S. Yang, *J. Mater. Chem. A* **2017**, *5*, 1724.
[92] M. Zhang, Q. Chen, R. Xue, Y. Zhan, C. Wang, J. Lai, J. Yang, H. Lin, J. Yao, Y, Li, L. Chen, Y. Li, *Nat. Commun.* **2019**, *10*, 4593.
[93] K. Liu, S. Chen, J. Wu, H. Zhang, M. Qin, X. Lu, Y. Tu, Q. Meng, X. Zhan, *Energy Environ. Sci.* **2018**, *11*, 3463.
[94] J. Wang, K. l Datta, C. H. L. Weijtens, M. M. Wienk, R. A. J. Janssen, *Adv. Funct. Mater.* **2019**, *29*, 1905883.
[95] X. Zhou, W. Zhang, S. Wang, F. Wen, Q. Chen, X. Shen, X. Hu, C. Peng, Z. Ma, M. Zhang, Y. Huang, S. Yang, W. Zhang, *Sci. China Mater* **2022**, *65*, 2325.
[96] M. Li, Z. Wang, T. Kang, Y. Yang, X. Gao, C. Hsu, Y. Li, L. Liao, *Nano Energy* **2018**, *43*, 47.
[97] H. Wang, F. Li, P. Wang, R. Sun, W. Ma, M. Chen, W. Miao, D. Liu, T. Wang, *Adv. Energy Mater.* **2020**, *10*, 2000615.
[98] M. M. Tavakoli, P. Yadav, R. Tavakoli, J. Kong, *Adv. Energy Mater.* **2018**, *8*, 1800794.
[99] P. Wang, R. Li, B. Chen, F. Hou, J. Zhang, Y. Zhao, X. Zhang, *Adv. Mater.* **2020**, *32*, 1905766.
[100] Q. Cao, Z. Li, J. Han, S. Wang, J. Zhu, H. Tang, X. Li, X. Li, *Sol. RRL* **2019**, *3*, 1900333.
[101] R. D. Chavan, M. M. Tavakoli, D. Prochowicz, P. Yadav, S. S. Lote, S. P. Bhoite, A. Nimbalkar, C. K. Hong, *ACS Appl. Mater. Interfaces* **2020**, *12*, 8098.
[102] S. F. Shaikh, H.-C. Kwon, W. Yang, H. Hwang, H. Lee, E. Lee, S. Ma, J. Moon, *J. Mater. Chem. A* **2016**, *4*, 15478.
[103] P. Huang, Q. Chen, K. Zhang, L. Yuan, Y. Zhou, B. Song, Y. Li, *J. Mater. Chem. A* **2019**, *7*, 6213.
[104] Y. Zhang, P. Gao, E. Oveisi, Y. Lee, Q. Jeangros, G. Grancini, S. Paek, Y. Feng, M. K. Nazeeruddin, *J. Am. Chem. Soc.* **2016**, *138*, 14380.
[105] F. Han, J. Luo, B. Zhao, Z. Wan, R. Wang, C. Jia, *Electrochim. Acta* **2017**, *236*, 122.
[106] J. Zhuang, P. Mao, Y. Luan, N. Chen, X. Cao, G. Niu, F. Jia, F. Wang, S. Cao, J. Wang, *Adv. Funct. Mater.* **2021**, *31*, 2010385.
[107] D. Wang, C. Wu, X. Qi, W. Luo, Y. Zhang, Z. Zhang, X. Guo, B. Qu, L. Xiao, Z. Chen, *ACS Appl. Energy Mater.* **2019**, *2*, 5883.
[108] H. Min, D. Y. Lee, J. Kim, G. Kim, K. S. Lee, J. Kim, M. J. Paik, Y. K. Kim, K. S. Kim, M. G. Kim, T. J. Shin, S. Il Seok, *Nature* **2021**, *598*, 444.
[109] Z. Gao, Y. Wang, H. Liu, J. Sun, J. Kim, Y. Li, B. Xu, W. C. H. Choy, *Adv. Funct. Mater.* **2021**, *31*, 2101438.
[110] M. Kim, I. Choi, S. J. Choi, J. W. Song, S. Mo, J. An, Y. Jo, S. Ahn, S. K. Ahn, G. Kim, D. S. Kim, *Joule* **2021**, *5*, 659.
[111] N. Tsvetkov, Q. Lu, Y. Chen, B. Yildiz, *ACS Nano* **2021**, *15*, 1805.
[112] C. Liu, K. Wu, Y. Lu, L. Hsiao, K. Lai, C. Chu, K. Ho, *ACS Appl. Mater. Interf.* **2021**, *13*, 60125.
[113] Q. Jiang, Y. Zhao, X. Li, Z. Yin, X. Zhang, J. You, *Nat. Photon.* **2019**, *13*, 460.
[114] S. Palei, H. Kim, J. H. Seo, D. Singh, K. Seo, *Adv. Mater. Interfaces* **2022**, *9*, 2200464.
[115] S. Jeong, S. Seo, H. Yang, H. Park, S. Shin, H. Ahn, D. Lee, J. H. Park, N. Park, H. Shin, *Adv. Energy Mater.* **2021**, *11*, 2102236.
[116] Yukta, N. Parikh, R. D. Chavan, P. Yadav, M. K. Nazeeruddin, S. Satapathi, *ACS Appl. Mater. Interf.* **2022**, *14*, 29744.
[117] B. Liu, J. Hu, D. He, L. Bai, Q. Zhou, W. Wang, C. Xu, Q. Song, D. Lee, P. Zhao, F. Hao, X. Niu, Z. Zang, J. Chen, *ACS Appl. Mater. Interf.* **2022**, *14*, 21079.
[118] S. J. Sung, J. Im, G. Kim, C. S. Moon, J. J. Yoo, S. S. Shin, N. J. Jeon, B. S. Ma, D. J. Kim, T.-S. Kim, J. Seo, *Adv. Energy Mater.* **2022**, *12*, 2200758.
[119] Y.-W. Jang, S. Lee, K. M. Yeom, K. Jeong, K. Choi, M. Choi, J. H. Noh, *Nat. Energy* **2021**, *6*, 63.
[120] S. Sidhik, Y. Wang, M. D. Siena, R. Asadpour, A. J. Torma, T. Terlier, K. Ho, W. Li, B. Puthirath, X. Shuai, A. Agrawal, B. Traore, M. Jones, R. Giridharagopal, P. M. Ajayan, J. Strzalka, D. S. Ginger, C2. Katan, M. A. Alam, J. Even, M. G. Kanatzidis, A. D. Mohite, *Science* **2022**, *377*, 1425.
[121] J. Xue, R. Wang, X. Chen, C. Yao, X. Jin, K. Wang, W. Huang, T. Huang, Y. Zhao, Y. Zhai, D. Meng, S. Tan, R. Liu, Z. Wang, C. Zhu, K. Zhu, M. C. Beard, Y. Yan, Y. Yang, *Science* **2021**, *371*, 636.
[122] J. Wu, Y. Li, Y. Zhang, Y. Li, Y. Huang, Z. Jiang, Q. Ai, Y. Liu, L. Zhang, Y. Peng, X. Wang, B. Xu, C. Cheng, *Small* **2022**, *18*, 2200130.
[123] Q. Chen, K. Deng, Y. Shen, L. Li, *InfoMat* **2022**, *4*, e12303.
[124] J. Chen, Y. Yang, H. Dong, J. Li =, X. Zhu, J. Xu, F. Pan, F. Yuan, J. Dai, B. Jiao, X. Hou, A. K.-Y. Jen, Z. Wu, *Sci. Adv.* **2022**, *8*, eabk2722.
[125] D. Luo, W. Yang, Z. Wang, A. Sadhanala, Q. Hu, R. Su, R. Shivanna, G. F. Trindade, J. F. Watts, Z. Xu, T. Liu, K. Chen, F. Ye, P. Wu, L. Zhao, J. Wu, Y. Tu, Y. Zhang, X. Yang, W. Zhang, R. H. Friend, Q. Gong, H. J. Snaith, R. Zhu, *Science* **2018**, *360*, 1442.
[126] Y. Tu, X. Yang, R. Su, D. Luo, Y. Cao, L. Zhao, T. Liu, W. Yang, Y. Zhang, Z. Xu, Q. Liu, J. Wu, Q. Gong, F. Mo, R. Zhu, *Adv. Mater.* **2018**, *30*, 1805085.
[127] J. Chen, S.-G. Kim, N.-G. Park, *Adv. Mater.* **2018**, *30*, 1801948.
[128] T. Webb, X. Liu, R. J. E. Westbrook, S. Kern, M. T. Sajjad, S. Jenatsch, K. D. G. I. Jayawardena, W. H. K. Perera, I. P. Marko, S. Sathasivam, B. Li, M. Yavari, D. J. Scurr, M. R. Alexander, T. J. Macdonald, S. A. Haque, S. J. Sweeney, W. Zhang, *Adv. Energy Mater.* **2022**, *12*, 2200666.
[129] M. Abdi-Jalebi, M. I. Dar, S. P. Senanayak, A. Sadhanala, Z. Andaji-Garmaroudi, L. M. Pazos-Outón, J. M. Richter, A. J. Pearson, H. Sirringhaus, M. Grätzel, R. H. Friend, *Sci. Adv.* **2019**, *5*, eaav2012.
[130] A. A. Sutanto, C. Igci, H. Kim, H. Kanda, N. Shibayama, M. Mensi, V. I. E. Queloz, C. Momblona, H. J. Yun, H. J. Bolink, A. J. Huckaba, M. K. Nazeeruddin, *ACS Appl. Energy Mater.* **2021**, *4*, 1259.
[131] T. Su, F. T. Eickemeyer, M. A. Hope, F. Jahanbakhshi, M. Mladenović, J. Li, Z. Zhou, A. Mishra, J. Yum, D. Ren, A. Krishna, O. Ouellette, T. Wei, H. Zhou, H. Huang, M. D. Mensi, K. Sivula, S. M. Zakeeruddin, J. V. Milić, A. Hagfeldt, U. Rothlisberger, L. Emsley, H. Zhang, M. Grätzel, *J. Am. Chem. Soc.* **2020**, *142*, 19980.
[132] C. Yang, H. Wang, Y. Miao, C. Chen, M. Zhai, Q. Bao, X. Ding, X. Yang, M. Cheng, *ACS Energy Lett.* **2021**, *6*, 2690.
[133] Y. Tian, H. Cheng, Y. Zhao, Z. Wang, *J. Mater. Chem. A* **2022**, *10*, 7173.

[134] B. Zhao, X. Yan, T. Zhang, X. Ma, C. Liu, H. Liu, K. Yan, Y. Chen, X. Li, *ACS Appl. Mater. Interf.* **2020**, *12*, 9300.
[135] M. Lyu, S. Park, H. Lee, B. S. Ma, S. H. Park, K.-H. Hong, H. Kim, T.-S. Kim, J. H. Noh, H. J. Son, N.-G. Park, *ACS Appl. Mater. Interf.* **2021**, *13*, 35595.
[136] F. Tan, H. Tan, M. I. Saidaminov, M. Wei, M. Liu, A. Mei, P. Li, B. Zhang, C.-S. Tan, X. Gong, Y. Zhao, A. R. Kirmani, Z. Huang, J. Z. Fan, R. Quintero-Bermudez, J. Kim, Y. Zhao, O. Voznyy, Y. Gao, F. Zhang, L. J. Richter, Z.-H. Lu, W. Zhang, E. H. Sargent, *Adv. Mater.* **2019**, *31*, 1807435.
[137] Y. Li, E. L. Lim, H. Xie, J. Song, T. Kong, Y. Zhang, M. Yang, B. Wu, C. Duan, D. Bi, *ACS Photon.* **2021**, *8*, 3185.
[138] P.-L. Qin, G. Yang, Z.-w. Ren, S. H. Cheung, S. K. So, L. Chen, J. Hao, J. Hou, G. Li, *Adv. Mater.* **2018**, *30*, 1706126.
[139] L. Meng, C. Sun, R. Wang, W. Huang, Z. Zhao, P. Sun, T. Huang, J. Xue, J.-W. Lee, C. Zhu, Y. Huang, Y. Li, Y. Yang, *J. Am. Chem. Soc.* **2018**, *140*, 17255.
[140] X. Zheng, J. Troughton, N. Gasparini, Y. Lin, M. Wei, Y. Hou, J. Liu, K. Song, Z. Chen, C. Yang, B. Turedi, A. Y. Alsalloum, J. Pan, J. Chen, A. A. Zhumekenov, T. D. Anthopoulos, Y. Han, D. Baran, O. F. Mohammed, E. H. Sargent, O. M. Bakr, *Joule* **2019**, *3*, 1963.
[141] R. Ma, Z. Ren, C. Li, Y. Wang, Z. Huang, Y. Zhao, T. Yang, Y. Liang, X. Sun, W. C. H. Choy, *Small* **2020**, *16*, 2002628.
[142] S. Akina, Y. Altintas, E. Mutlugund, S. Sonmezoglu, *Nano Energy* **2019**, *60*, 557.
[143] Y. Zhang, H. Yang, M. Chen, N. P. Padture, O. Chen, Y. Zhou, *Adv. Energy Mater.* **2019**, *9*, 1900243.
[144] Y. Wang, T. Wu, J. Barbaud, W. Kong, D. Cui, H. Chen, X. Yang, L. Han, *Science* **2019**, *365*, 687.
[145] X. Li, T. Tong, Q. Wu, S. Guo, Q. Song, J. Han, Z. Huang, *Adv. Funct. Mater.* **2018**, *28*, 1800475.
[146] Y. Wang, W. Li, Y. Yin, M. Wang, W. Cai, Y. Shi, J. Guo, W. Shang, C. Zhang, Q. Dong, H. Ma, J. Liu, W. Tian, S. Jin, J. Bian, Y. Shi, *Adv. Funct. Mater.* **2022**, *32*, 2204831.
[147] J. Ma, G. Yang, M. Qin, X. Zheng, H. Lei, C. Chen, Z. Chen, Y. Guo, H. Han, X. Zhao, G. Fang, *Adv. Sci.* **2017**, *4*, 1700031.
[148] W. Lee, J. Choi, J. W. Jung, *Org. Electron.* **2017**, *51*, 404.
[149] X. Li, S. Fu, W. Zhang, S. Ke, W. Song, J. Fang, *Sci. Adv.* **2020**, *6*, eabd1580.
[150] J. Xie, X. Yu, J. Huang, X. Sun, Y. Zhang, Z. Yang, M. Lei, L. Xu, Z. Tang, C. Cui, P. Wang, D. Yang, *Adv. Sci.* **2017**, *4*, 1700018.
[151] J. Lee, J. Kim, C.-L. Lee, G. Kim, T. K. Kim, H. Back, S. Jung, K. Yu, S. Hong, S. Lee, S. Kim, S. Jeong, H. Kang, K. Lee, *Adv. Energy Mater.* **2017**, *7*, 1700226.
[152] E. M. Sanehira, B. J. T. de Villers, P. Schulz, M. O. Reese, S. Ferrere, K. Zhu, L. Y. Lin, J. J. Berry, J. M. Luther, *ACS Energy Lett.* **2016**, *1*, 38.
[153] Y. Hou, X. Du, S. Scheiner, D. P. McMeekin, Z. Wang, N. Li, M. S. Killian, H. Chen, M. Richter, I. Levchuk, N. Schrenker, E. Spiecker, T. Stubhan, N. A. Luechinger, A. Hirsch, P. Schmuki, H.-P. Steinrück, R. H. Fink, M. Halik, H. J. Snaith, C. J. Brabec, *Science* **2017**, *355*, 722.
[154] Y. Zhao, T. Heumueller, J. Zhang, J. Luo, O. Kasian, S. Langner, C. Kupfer, B. Liu, Y. Zhong, J. Elia, A. Osvet, J. Wu, C. Liu, Z. Wan, C. Jia, N. Li, J. Hauch, C. J. Brabec, *Nat. Energy* **2022**, *7*, 144.
[155] H. Si, Q. Liao, Z. Zhang, Y. Li, X. Yang, G. Zhang, Z. Kang, Y. Zhang, *Nano Energy* **2016**, *22*, 223.
[156] G. Mathiazhagan, L. Wagner, S. Bogati, K. Y. Ünal, D. Bogachuk, Th. Kroyer, S. Mastroianni, A. Hinsch, *ACS Appl. Nano Mater.* **2020**, *3*, 2463.
[157] Q. Wang, Q. Dong, T. Li, A. Gruverman, J. Huang, *Adv. Mater.* **2016**, *28*, 6734.
[158] Y. Zheng, W. Shi, J. Kong, D. Huang, H. E. Katz, J. Yu, A. D. Taylor, *Small Methods* **2017**, *1*, 1700244.
[159] G. Li, S. Deng, M. Zhang, R. Chen, P. Xu, M. Wong, H.-S. Kwok, *Sol. RRL* **2018**, *2*, 1800151.
[160] E. Ochoa-Martinez, M. Ochoa, R. D. Ortuso, P. Ferdowsi, R. Carron, A. N. Tiwari, U. Steiner, M. Saliba, *ACS Energy Lett.* **2021**, *6*, 2626.
[161] J. Peng, Y. Wu, W. Ye, D. A. Jacobs, H. Shen, X. Fu, Y. Wan, T. Duong, N. Wu, C. Barugkin, H. T. Nguyen, D. Zhong, J. Li, T. Lu, Y. Liu, M. N. Lockrey, K. J. Weber, K. R. Catchpolea, T. P. White, *Energy Environ. Sci.* **2017**, *10*, 1792.
[162] J. Peng, J. I. Khan, W. Liu, E. Ugur, T. Duong, Y. Wu, H. Shen, K. Wang, H. Dang, E. Aydin, X. Yang, Y. Wan, K. J. Weber, K. R. Catchpole, F. Laquai, S. De Wolf, T. P. White, *Adv. Energy Mater.* **2018**, *8*, 1801208.
[163] M. Kim, S. G. Motti, R. Sorrentino, A. Petrozza, *Energy Environ. Sci.* **2018**, *11*, 2609.
[164] D. Yang, R. Yang, S. Priya, S. Liu, *Angew. Chem., Int. Ed.* **2019**, *58*, 4466.
[165] B. Zhang, J. Su, X. Guo, L. Zhou, Z. Lin, L. Feng, J. Zhang, J. Chang, Y. Hao, *Adv. Sci.* **2020**, *7*, 1903044.
[166] N. Ren, B. Chen, R. Li, P. Wang, S. Mazumdar, B. Shi, C. Zhu, Y. Zhao, X. Zhang, *Sol. RRL* **2021**, *5*, 2000795.
[167] B. J. Kim, M. Kim, D. G. Lee, G. Lee, G. J. Bang, J. B. Jeon, M. Choi, H. S. Jung, *Adv. Mater. Interfaces* **2018**, *5*, 1800993.
[168] M. Zhong, Y. Liang, J. Zhang, Z. Wei, Q. Li, D. Xu, *J. Mater. Chem.* **2019**, *7*, 6659.
[169] J. Xiong, N. Liu, X. Hu, Y. Qi, W. Liu, J. Dai, Y. Zhang, Z. Dai, X. Zhang, Y. Huang, Z. Zhang, Q. Dai, J. Zhang, *Adv. Energy Mater.* **2022**, *12*, 2201787.
[170] Y. Meng, J. Zhang, C. Liu, K. Zheng, L. Xie, S. Bu, B. Han, R. Cao, X. Yin, C. Liu, Z. Ge, *Adv. Funct. Mater.* **2022**, *32*, 2210600.
[171] X. Zhu, H. Dong, J. Chen, J. Xu, Z. Li, F. Yuan, J. Dai, B. Jiao, X. Hou, J. Xi, Z. Wu, *Adv. Funct. Mater.* **2022**, *32*, 2202408.
[172] Q. Dong, C. Zhu, M. Chen, C. Jiang, J. Guo, Y. Feng, Z. Dai, S. K. Yadavalli, M. Hu, X. Cao, Y. Li, Y. Huang, Z. Liu, Y. Shi, L. Wang, N. P. Padture, Y. Zhou, *Nat. Commun.* **2021**, *12*, 973.
[173] D. Gao, B. Li, Z. Li, X. Wu, S. Zhang, D. Zhao, X. Jiang, C. Zhang, Y. Wang, Z. Li, N. Li, S. Xiao, W. C. H. Choy, A. K.-Y. Jen, S. Yang, Z. Zhu, *Adv. Mater.* **2022**, *34*, 2206387.
[174] C. Long, K. Huang, J. Chang, C. Zuo, Y. Gao, X. Luo, B. Liu, H. Xie, Z. Chen, J. He, H. Huang, Y. Gao, L. Ding, J. Yang, *Small* **2021**, *17*, 2102368.
[175] Z. Dai, S. Li, X. Liu, M. Chen, C. E. Athanasiou, B. W. Sheldon, H. Gao, P. Guo, N. P. Padture, *Adv. Mater.* **2022**, *34*, 2205301.
[176] X. Meng, Z. Cai, Y. Zhang, X. Hu, Z. Xing, Z. Huang, Z. Huang, Y. Cui, T. Hu, M. Su, X. Liao, L. Zhang, F. Wang, Y. Song, Y. Chen, *Nat. Commun.* **2020**, *11*, 3016.
[177] B. Fan, J. Xiong, Y. Zhang, C. Gong, F. Li, X. Meng, X. Hu, Z. Yuan, F. Wang, Y. Chen, *Adv. Mater.* **2022**, *34*, 2201840.
[178] H. B. Lee, N. Kumar, B. Tyagi, K.-J. Ko, J.-W. Kang, *Sol. RRL* **2021**, *5*, 2000589.
[179] G. Grancini, C. Roldán-Carmona, I. Zimmermann, E. Mosconi, X. Lee, D. Martineau, S. Narbey, F. Oswald, F. De Angelis, M. Graetzel, M. K. Nazeeruddin, *Nat. Commun.* **2017**, *8*, 15684.
[180] J. Dagar, M. Fenske, A. Al-Ashouri, C. Schultz, B. Li, H. Köbler, R. Munir, G. Parmasivam, J. Li, I. Levine, A. Merdasa, L. Kegelmann, H. Näsström, J. A. Marquez, T. Unold, D. M. Többens, R. Schlatmann, B. Stegemann, A. Abate, S. Albrecht, E. Unger, *ACS Appl. Mater. Interfaces* **2021**, *13*, 13022.
[181] C. Liu, Y. Yang, K. Rakstys, A. Mahata, M. Franckevicius, E. Mosconi, R. Skackauskaite, B. Ding, K. G. Brooks, O. J. Usiobo, J.-N. Audinot, H. Kanda, S. Driukas, G. Kavaliauskaite, V. Gulbinas, M. Dessimoz, V. Getautis, F. De Angelis, Y. Ding, S. Dai, P. J. Dyson, M. K. Nazeeruddin, *Nat. Commun.* **2021**, *12*, 6394.
[182] Z. Liu, L. Qiu, K. Ono, S. He, Z. Hu, M. Jiang, G. Tong, Z. Wu, Y. Jiang, D.-Y. Son, Y. Dang, S. Kazaoui, Y. Qi, *Nat. Energy* **2020**, *5*, 596.
[183] Y. Sha, E. Bi, Y. Zhang, P. Ru, W. Kong, P. Zhang, X. Yang, H. Chen, L. Han, *Adv. Energy Mater.* **2021**, *11*, 2003301.

[184] M. Du, S. Zhao, L. Duan, Y. Cao, H. Wang, Y. Sun, L. Wang, X. Zhu, J. Feng, L. Liu, X. Jiang, Q. Dong, Y. Shi, K. Wang, S. Liu, *Joule* **2022**, *6*, 1931.
[185] S. Pisoni, F. Fu, R. Widmer, R. Carron, T. Moser, O. Groening, A. N. Tiwari, S. Buecheler, *Nano Energy* **2018**, *49*, 300.
[186] T. Bu, J. Li, F. Zheng, W. Chen, X. Wen, Z. Ku, Y. Peng, J. Zhong, Y. Cheng, F. Huang, *Nat. Commun.* **2018**, *9*, 4609.
[187] S. Pescetelli, A. Agresti, G. Viskadouros, S. Razza, K. Rogdakis, I. Kalogerakis, E. Spiliarotis, E. Leonardi, P. Mariani, L. Sorbello, M. Pierro, C. Cornaro, S. Bellani, L. Najafi, B. Martín-García, A. E. D. R. Castillo, R. Oropesa-Nuñez, M. Prato, S. Maranghi, M. L. Parisi, A. Sinicropi, R. Basosi, F. Bonaccorso, E. Kymakis, A. D. Carlo, *Nat. Energy* **2022**, *7*, 597.
[188] E. Mosconi, J. M. Azpiroz, F. De Angelis, *Chem. Mater.* **2015**, *27*, 4885.
[189] W. Chen, J. Zhang, G. Xu, R. Xue, Y. Li, Y. Zhou, J. Hou, Y. Li, *Adv. Mater.* **2018**, *30*, 1800855.
[190] T. Leijtens, K. Bush, R. Cheacharoen, R. Beal, A. Bowring, M. D. McGehe, *J. Mater. Chem. A* **2017**, *5*, 11483.
[191] Y. Liang, P. Song, H. Tian, C. Tian, W. Tian, Z. Nan, Y. Cai, Pa. Yang, C. Sun, J. Chen, L. Xie, Q. Zhang, Z. Wei, *Adv. Funct. Mater.* **2022**, *32*, 2110139.
[192] Z. Li, X. Wu, B. Li, S. Zhang, D. Gao, Y. Liu, X. Li, N. Zhang, X. Hu, C. Zhi, A. K.-Y. Jen, Z. Zhu, *Adv. Energy Mater.* **2022**, *12*, 2103236.
[193] H. Zhang, K. Li, M. Sun, F. Wang, H. Wang, A. K.-Y. Jen, *Adv. Energy Mater.* **2021**, *11*, 2102281.
[194] H. Bi, G. Han, M. Guo, C. Ding, H. Zou, Q. Shen, S. Hayase, W. Hou, *ACS Appl. Mater. Interf.* **2022**, *14*, 35513.
[195] Z. He, Y. Hu, G. Sun, W. Song, X. Wang, S. Zhang, J. Wang, M. Wang, T. Sun, Y. Tang, *Sol. RRL* **2022**, *6*, 2200567.
[196] G. Xiao, L. Wang, X. Mu, X. Zou, Y. Wu, J. Cao, *CCS Chem.* **2021**, *3*, 25.
[197] J. Lee, G. Kim, M. Kim, S. A. Park, T. Park, *Adv. Energy Mater.* **2020**, *10*, 1902662.
[198] S. Chen, Y. Deng, H. Gu, S. Xu, S. Wang, Z. Yu, V. Blum, J. Huang, *Nat. Energy* **2020**, *5*, 1003.
[199] S. Chen, Y. Deng, X. Xiao, S. Xu, P. N. Rudd, J. Huang, *Nat. Sustain.* **2021**, *4*, 636.
[200] S. Wu, Z. Li, M. Li, Y. Diao, F. Lin, T. Liu, J. Zhang, P. Tieu, W. Gao, F. Qi, X. Pan, Z. Xu, Z. Zhu, A. K.-Y. Jen, *Nat. Nanotechnol.* **2020**, *15*, 934.
[201] R. Nie, W. Chu, Z. Li, H. Li, S. Chen, Y. Chen, Z. Zhang, X. Liu, W. Guo, S. Il Seok, *Adv. Energy Mater.* **2022**, *12*, 2200480.

**Jianxing Xia** obtained his Ph.D. at the University of Electronic Science and Technology of China (UESTC) under the supervision of Prof. Chunyang Jia in 2022. During his Ph.D., He took two years as a visiting Ph.D. student in Group for Molecular Engineering of Functional Material (GMF), Institute of Chemical Sciences and Engineering, at Ecole Polytechnique Fédérale de Lausanne (EPFL) under the guidance of Prof. Mohammad K. Nazeeruddin. He is currently a postdoctoral researcher under Prof. Mohammad K. Nazeeruddin. His interests concentrate on novel hole-transporting materials and their novel p-dopant development, device engineering, and theory analysis for perovskite solar cells.

**Muhammad Sohail** has obtained a Ph.D. in chemistry from The Open University, Milton Keynes, UK, and is a research scientist at Texas A&M University in Qatar. His current research focuses on developing functional materials and optimizing their optoelectronic properties for solar cells and photo electrocatalysis. He has a demonstrable record of conceiving and successfully leading research projects, establishing international collaborations, and securing externally funded grants. Ha has leadership experience in capacity and program-building with proven capability to work on multiple R&D projects and bring them to completion.

**Mohammad Khaja Nazeeruddin** received his Ph.D. in Inorganic Chemistry from Osmania University Hyderabad, India. Currently, he is a professor of Chemistry at Ecole Polytechnique Fédérale de Lausanne (EPFL), Lausanne, and his research focuses on Perovskite and Dye-Sensitized Solar Cells and Light-emitting diodes. His group is involved in developing stable perovskite solar cells by compositional and interface engineering and developing novel hole-transporting material. He was appointed as World Class University (WCU) professor at Korea University, and Adjunct Professor at King Abdulaziz University, Jeddah.